Cross-Flow Turbine Fluid Mechanics: Experimental Optimization and Analysis

Benjamin W. Strom

A dissertation
submitted in partial fulfillment of the
requirements for the degree of

Doctor of Philosophy

University of Washington

2019

Reading Committee:

Brian Polagye, Chair

Steven Brunton, Chair

Benjamin Maurer

Program Authorized to Offer Degree:
Mechanical Engineering

University of Washington

Abstract

Cross-Flow Turbine Fluid Mechanics:
Experimental Optimization and Analysis

Benjamin W. Strom

Co-Chairs of the Supervisory Committee:
Associate Professor Brian Polagye
Department of Mechanical Engineering

Assistant Professor Steven Brunton
Department of Mechanical Engineering

Cross-flow turbines are devices for converting the kinetic energy of wind or water currents to rotational mechanical energy. The dual objectives of this work are to increase our understanding of cross-flow turbine flow physics and to improve the energy conversion performance of individual rotors and arrays. Experiments are conducted using scale models in flumes or tow-tanks. The first group of studies examines cross-flow turbine rotor geometry. To make the parameter space tractable, this work is restricted to straight-bladed turbines with NACA0018 blade profiles. The shape and location of structures used to mount the blades to the center shaft are found to have substantial impact on turbine power output. Likewise, performance is found to be sensitive to the blade mounting angle. Finally, results are presented from a large multi-parameter study on how optimal mounting angle, number of blades, and chord length change with the scale of the turbine. Optimal geometry parameters are found to be strongly co-dependent. The most efficient turbine geometry for small and large-scale rotors is found to differ significantly due to blade boundary layer effects. In the following chapter, measurements of the wake of a cross-flow turbine using particle image velocimetry are presented. A new fluid analysis approach for extracting oscillatory flows is introduced and used to describe the wake features. The form and trajectory of Lagrangian coherent structures in the wake are described. Strong span-wise (axial) flow is observed in the core of shed vortices for the first time in a cross-flow turbine wake. The last chapter focuses on advanced control of cross-flow turbine rotors. A rotor control scheme that optimizes the local flow conditions on the blade by varying the rotor angular velocity is presented, and shown to increase turbine performance by 59% over standard control methods. Control and geometric optimization of an array of two turbine rotors is performed. This includes the introduction of a new array controller that seeks to optimize interactions with the coherent structures observed in the wake analysis. Beneficial interactions between rotors are shown to increase the array performance by 1.3 times that of isolated turbines.

TABLE OF CONTENTS

Page

LIST OF FIGURES

Figure Number Page

LIST OF TABLES

NOMECLATURE

Acronyms:

CFT: Cross-flow turbine

AFT: Axial-flow turbine

TSR: Tip-speed ratio (see λ below)

DAQ: Data Acquisition (system)

ADV: Acoustic Doppler velocimeter

PIV: Particle image velocimetry

POD: Proper orthogonal decomposition

DMD: Dynamic mode decomposition

Constants and Variables:

U_∞: Freestream velocity

ρ: Freestream fluid density

ν: Fluid kinematic viscosity

H: Rotor height

D: Rotor diameter

R: Rotor radius

c: Rotor blade chord length

N: Rotor blade count

α_p: Preset pitch (blade mounting) angle

I: Mass moment of inertia of the rotor, shaft, and generator rotor

τ: Rotor mechanical torque. Torque on rotor due only to fluid interactions and angular acceleration

τ_f: Fluid torque. Torque imparted to the rotor due to fluid forcing

τ_c: Control Torque. Torque imparted to the rotor by all external (non-fluid) forces (e.g. generator, bearing torques, etc.).

ω: Rotor rotational velocity

F_x: Streamwise fluid force on the rotor (thrust)

F_y: Cross-stream (lateral) fluid force on the rotor (perpendicular to stream wise direction and rotor axis)

σ: Rotor solidity, $\frac{Nc}{\pi D}$

A_r: Rotor aspect ratio, $\frac{H}{D}$

λ: Tip-speed ratio, $\frac{\omega R}{U_\infty}$

C_P: Power coefficient, or the fluid kinetic to mechanical energy conversion efficiency, $\frac{\omega \tau_f}{\frac{1}{2}\rho U_\infty^3 HD}$

C_Q: Torque coefficient, $\frac{\tau}{\frac{1}{2}\rho U_\infty^2 HDR}$

C_t: Thrust coefficient, $\frac{F_x}{\frac{1}{2}\rho U_\infty^2 HD}$

C_ℓ: Lateral (cross-stream) force coefficient, $\frac{F_y}{\frac{1}{2}\rho U_\infty^2 HD}$

B_r: Blockage ratio, ratio of turbine frontal area to test section cross section $\frac{HD}{A_{\text{test section}}}$

Re_D: Diameter-based Reynolds number, $\frac{DU_\infty}{\nu}$

ACKNOWLEDGMENTS

This body of work would not have been possible without the generosity, support, and creative input of many people. First and foremost, thank you to my advisors Dr. Brian Polagye and Dr. Steven Brunton for guiding me in my growth as a scientist, engineer, and person. Many thanks to all members of the Steve Brunton and Marine Renewable Energy Laboratory groups, particularly the cross-flow turbine experimental team Dr. Rob Cavagnaro, Hannah Ross, Dr. Craig Hill, Dr. Dom Forbush, and Isabel Scherl. Additionally Noah Johnson played a critical role in the end-plate experiments and fabricated many key experimental components.

Thank you to the Bamfield Marine Science Centre for hosting yearly experimental campaigns, particularly to Dr. Eric Clelland, who was vital to the success of these experiments. Dr. Martin Wosnik and the team at the University of New Hampshire Jere A. Chase Ocean Engineering Laboratory made the tow-tank testing of large-scale turbines possible, and conversations Dr. Wosnik on CFT physics proved invaluable.

Thank you to reading committee member Dr. Benjamin Maurer and committee members Dr. Andrew Stewart and Dr. Tom Daniels.

The Alice C. Tyler trust provided funding for a complete re-build and upgrade to our in-house turbine testing flume. Thank you to all who contributed labor and expertise to the flume upgrade project, particularly Corey Luker and Thomas Alvarado.

Funding for this work was provided by Naval Facilities Engineering Command and the Department of Energy

Finally, thank you Dr. Kenneth Breuer, for setting me on this path, and to my family, who made this all possible.

DEDICATION

In memory of William Anthony Strom.

Chapter 1

INTRODUCTION

Addressing climate change is one of the defining challenges of our generation. In the face of political volatility, a permanent and more rapid transition away from fossil fuel-based energy sources can only be guaranteed through economic viability. Economies of scale promise to drive the cost of renewable energy generation down, as evidenced by the reduction in costs associated with photovoltaics in recent years. However, technological advances may be the most effective means of increasing the share of renewable energy in total power generation. A new or improved technology may decrease cost of generation in traditional markets, but more importantly will result in the an increase in the quantity of economically available renewable energy.

The global wind energy resource is over twenty times the total global energy consumption [94] but provides only 6% of global [61] and 5.5% of U.S. electrical power [2]. The U.S. Department of Energy has stated a goal of 20% of domestic electricity generation from wind by 2030 and 35% by 2050. Continued reductions in the cost of energy from terrestrial wind farms using conventional technology may be limited. The rate of cost reduction has slowed or reversed in the past decade [203], and it is estimated that there will only be further a 1% drop in the cost of terrestrial wind power over the next seven years [166]. A new wind energy technology has the potential to side-step this slow rate of cost reduction.

A promising, yet currently untapped source of renewable energy is in flowing water of rivers and tidal or convective ocean currents. Termed hydrokinetic energy, this differs from traditional hydropower in that it seeks to extract kinetic energy from moving water, rather than potential energy from a height difference. Still in its infancy, this industry is in the technological development and pilot project stage, with several competing turbine technologies.

Due to the complexities of deployment, operations, and maintenance in a water environment, cost reductions through technical advancement are critical to harnessing hydrokinetic energy economically.

This body of work focuses on technical improvement and deepening our understanding of the physics of an old but little-used technology for converting flow kinetic energy to rotational mechanical energy: the cross-flow turbine (CFT). Conventional axial-flow turbines (AFTs), also known as horizontal-axis turbines, have blades that rotate about an axis parallel to the incoming flow. A CFT's rotation axis is perpendicular to the flow direction. Termed vertical-axis turbines in the wind energy industry, we refer to this class of devices as CFTs, because, neglecting variations in the inflow velocity or mounting considerations, their operational principles remain unchanged with regard to their orientation to the horizon. Challenging fluid dynamics and comparatively little development effort indicate that this promising technology is ripe for improvement. Given its unique properties, this turbine type has the potential to revolutionize the wind and hydrokinetic energy industries.

1.1 Cross-Flow Turbines

Two major subcategories of CFTs exist: One class derives rotational torque, and thus power from drag and the other from lift. In a drag-based CFT, the blades or vanes travel at a velocity less than the local flow velocity such that passing fluid may impart a drag force. One example of a drag-based CFT design is the Savonius rotor [4]. In a lift-based CFT, for at least part of the rotational cycle, the blades travel faster than the local flow velocity. This allows a lift force to be generated by foil-shaped blades, imparting a rotational torque to the turbine. Drag-based CFTs operate a lower rotational speeds, have a lower energy conversion efficiency, and are able to begin rotating in lower flow velocities. This work focuses on the more efficient, lift-based CFTs. This turbine type is sometimes referred to as a Darius turbine, Gyromill, or H-rotor, depending on rotor geometry specifics.

The maximum efficiency of CFTs is generally lower than that of AFTs. One of the most efficient large-scale CFTs constructed was the Sandia 34 m vertical-axis wind turbine testbed.

The industry average efficiency for AFTs is about 15% higher than the peak performance of this turbine [191, 8]. This performance difference, combined with more analytically tractable aerodynamics facilitating design optimization, has resulted in AFTs as the dominant technology in the wind energy industry. Additionally, challenging and hard-to-predict oscillatory loading lead to the failure of several early large-scale VAWT prototypes [132]. Though one of the motivations of this body of work is to close the performance gap between CFTs and AFTs, a number of CFT characteristics may make CFTs an appropriate choice for some applications at current efficiency levels. First, the maximum blade speed of CFTs is generally lower than equivalently-sized AFTs [99], reducing collision risk with aerial or aquatic species. In hydrokinetic applications, blade cavitation is limited. Noise and vibration generation may also be decreased. Second, a vertically oriented CFT operates omi-directionally, removing the need for active yaw control. Mechanical complexity is reduced, and performance in turbulent flows, such as urban environments, may be increased compared to AFTs [17]. Third, a driveshaft extending the length of the rotor presents a number of potential benefits. In a vertical orientation, heavy and maintenance-intensive components such as the gearbox and generator can be located at the base of the rotor. For terrestrial wind, this can reduce tower and installation expenses. For floating platform offshore wind, stability is increased [188]. In arrays of horizontally-oriented CFTs, multiple rotors can drive a common generator, reducing total array cost. Fourth, the rectangular or otherwise elongated projected area of CFTs make them more suited to harness energy in shallow water flows, and may better facilitate the construction of high blockage-ratio arrays, resulting in elevated array power output [160]. Fifth, CFT blades can be constructed with constant cross-section, enabling inexpensive, continuous, mass-manufacturing methods, unlike AFT blade which require molds. Finally, when compared on an energy-out per unit land area basis, arrays of CFTs can outperform arrays of AFTs due to beneficial turbine interactions [202, 48, 101], faster wake recovery [29], and more efficient array boundary layer mixing [102].

1.2 Operational Principles

1.2.1 Blade Flow Conditions

In their simplest and most common configuration, CFTs have just a single degree of freedom: rotation about a central axis perpendicular to the flow. Despite this outward simplicity, the fluid dynamics responsible for CFT operation are complex, especially when compared to AFTs. The first source of complexity stems from the variable flow conditions experienced by a CFT blade during a single rotational cycle. From the perspective of the blade, the local flow is determined by three factors: the freestream flow velocity, the apparent velocity due to rotation, and any flow velocities induced by interaction of the rotor and the fluid, or in vector form,

$$\boldsymbol{U}(\theta) = \boldsymbol{U_\infty}(\theta) + \boldsymbol{U_\omega}(\theta) + \boldsymbol{U}_{\text{induced}}(\theta), \tag{1.1}$$

where θ is the azimuthal angular position of the blade quarter-chord (time dependence is not indicated for compactness). Zero angular position ($\theta = 0$) is defined as the point where the blade rotational velocity vector point directly upstream. Throughout this manuscript, bold mathematical symbols indicate a vector quantity. Both the contribution of the freestream velocity, $\boldsymbol{U_\infty}$, and the contribution of the turbine rotation, $\boldsymbol{U_\omega}$ can be derived from geometric relations, as illustrated in Fig. 1.1. If the induced velocity is neglected, an approximation for the local flow conditions can be made, here referred to as the nominal velocity and given by

$$\boldsymbol{U_n}(\theta) = \boldsymbol{U_\infty}(\theta) + \boldsymbol{U_\omega}(\theta). \tag{1.2}$$

A natural coordinate system to use when examining the local flow conditions on a blade is the local velocity magnitude and the aerodynamic angle of attack, α, since foil force generation is presented as functions of these variables. Again neglecting the induced flow, the nominal angle of attack is given by,

$$\alpha_n(\theta) = -\tan^{-1}\left[\sin(\theta), \lambda(\theta) + \cos(\theta)\right] + \alpha_p(\theta), \tag{1.3}$$

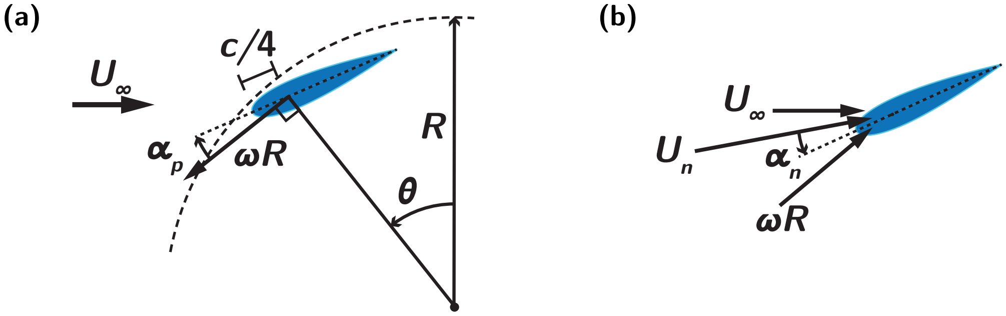

Figure 1.1: **(a)** Rotational and freestream velocity vectors and geometric parameters contributing to **(b)** the total local flow velocity and angle of attack (neglecting flow induced by the rotor).

while the nominal velocity magnitude is

$$|\boldsymbol{U_n}(\theta)| = U_\infty \sqrt{\lambda(\theta)^2 + 2\lambda(\theta)\cos(\theta) + 1}. \tag{1.4}$$

Here $\tan^{-1}$ indicates the four-quadrant arctangent and α_p is the blade mounting angle, where a positive angle indicates the blade leading edge is rotated radially outward about the quarter-chord. The tip-speed ratio (TSR), λ is the ratio of the velocity due to rotation to the freestream velocity, or

$$\lambda(\theta) = \frac{\omega(\theta)R}{U_\infty}, \tag{1.5}$$

where $\omega = \frac{d\theta}{dt}$ is the turbine rotation rate and R is the blade mounting radius. For non-constant radius turbine geometries, such as those with troposkein blades, the TSR may also vary along the turbine height. To facilitate cross-comparison, the nominal velocity magnitude is presented normalized by the freestream velocity as

$$U_n(\theta)^* = \frac{|\boldsymbol{U_n}(\theta)|}{U_\infty} = \sqrt{\lambda(\theta)^2 + 2\lambda(\theta)\cos(\theta) + 1}. \tag{1.6}$$

Even if the mounting angle and the rotation rate are held constant, α_n and U_n^* vary over the course of one rotation. This variation is shown for one turbine geometry at various TSRs in Fig. 1.2.

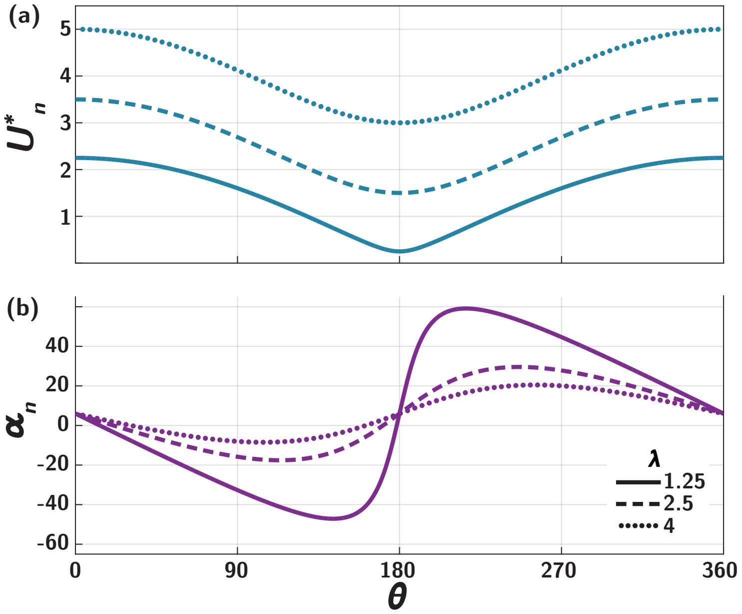

Figure 1.2: Variation in local flow velocity incident on the blade, normalized by the freestream velocity **(a)** and the local angle of attack **(b)** as functions of blade position. Both figures neglect flow induced by the rotor.

1.2.2 Power Generation

CFT blades are designed to maximize lift (a force perpendicular to the local flow velocity) while minimizing drag (a force aligned with the local flow velocity) over a certain range of local angles of attack. In a lift-based CFT, fluid energy is converted to rotational energy by the projection of the lift force vector onto the rotational velocity vector. Alternatively but equivalently, the cross-product of the blade radius vector with the lift vector results in a torque in the direction of rotation. Due to the varying flow conditions, this forcing varies throughout a rotation. Figure 1.3 shows a projection of lift and drag forces responsible for positive torque. The instantaneous torque produced by all blades, less the drag torque produced by other rotating turbine components interacting with the fluid multiplied by rotation rate of the turbine equals the fluid mechanical power generated by the rotor.

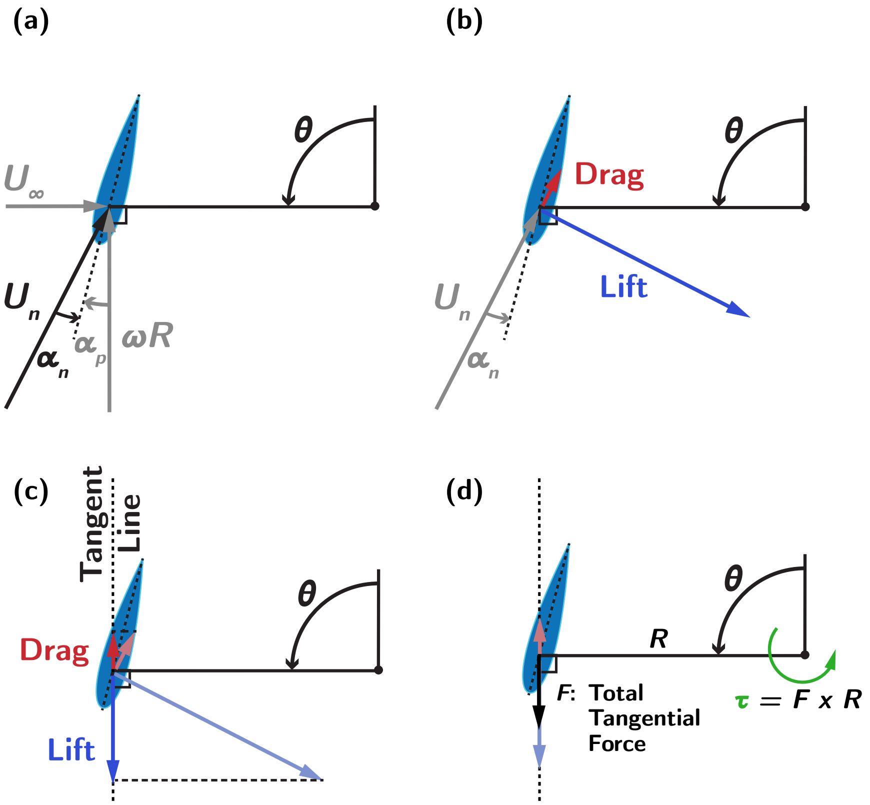

Figure 1.3: An illustration of how CFTs generate torque through lift and drag. Freestream flow is from left to right. **(a)** Local flow velocity vector at $\theta = 90°$ resulting from the sum of the freestream and rotational velocity vectors. The TSR is about 2. **(b)** The resulting lift and drag force vectors generated due to these local flow conditions. **(c)** Decomposition of these force vectors onto the direction of foil motion. **(d)** The resulting total tangential force and generated torque. Power output is a positive torque times a positive angular velocity.

1.2.3 Fluid Forcing Complications

The above description may lead to the false impression that estimation of the fluid forces on CFT blades is trivial. However, a number of factors make estimation of CFT power output analytically challenging and difficult even for high-resolution computational fluid dynamics (CFD) models. The first of these complications stems from the inherent variability of the blade local flow conditions. Given the local angle of attack and velocity, look up tables, or foil polars can provide accurate estimates of fluid forcing for a foil with a constant inflow. Combined with conservation of mass and momentum, foil polars are the basis for blade element momentum theory, a successful semi-analytic AFT model. No universal model exists to predict foil forcing under unsteady flow conditions. Forcing depends on the instantaneous values and time history of both the inflow velocity vector and its derivatives. To make things worse, the local angle of attack in CFTs can extend beyond the static stall angle, or the angle at which flow no longer passes smoothly over the blade. This process of separation during a dynamic pitching maneuver is termed dynamic stall. Prediction of dynamic stall forcing is an active area of research[36], with current models still unable to predict foil forcing over a variety of conditions[87]. Additionally, models often have parameters that must be tuned to a specific case, and thus fall short as a design tool. An excellent review of dynamic stall phenomena and models can be found in J. Leishman's book, *Principles of Helicopter Aerodynamics*, Chapters 8 and 9 [110].

A second complication arises from our previous omission of the induced velocity, $\boldsymbol{U}_{\text{induced}}$. Since any force imparted on the rotor blades must impart an equal and opposite force on the fluid, the performance of the blade and the activity of surrounding flow field are inextricably coupled. Attempts to model this effect have been made, such as the double-multiple stream-tube model[145] and vortex particle methods[138]. The former, depending on the implementation, may require non-physical assumptions, such as neglecting conservation of mass or flow induced in the cross-stream direction. To converge on a solution, both of these and related methods require the use of inaccurate dynamic stall models. Finally, the double-

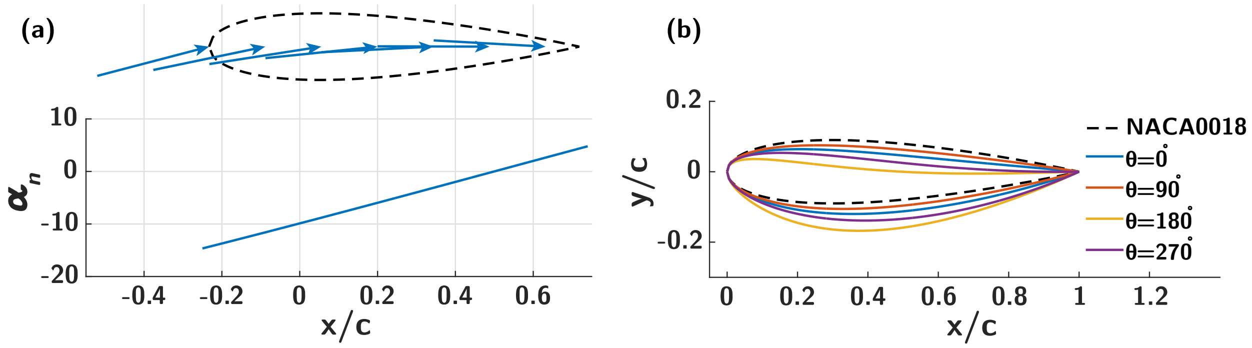

Figure 1.4: **(a)** Illustration of the variation in angle attack along the chord line for a high chord-to-radius turbine. **(b)** The "induced camber" effect of operating in a curvilinear flow field, as a function of blade position.

multiple stream-tube model has no mechanism for including the effect of vortical structures generated by the blades during dynamic stall.

An additional flow complexity arises from the circular path traced by the blades. For turbines with large blades compared to the radius, the local angle of attack can change significantly along the chord length of the blade, as shown in Fig. 1.4 **(a)**. An alternative view is that the foil is operating in a curvilinear flow field. Migliore, Wolfe, and Fanucci showed that the geometry of foil in a curvilinear flow field can be conformally mapped to a new geometry in a linear flow field, such that the forcing between cases is identical[127]. This effect results in a symmetric foil in curvilinear flow demonstrating the forcing properties of a cambered foil, and thus is termed virtual camber. To further add to the complexity, the amount and shape of the virtual camber changes over the course of one rotation, as shown in Fig. 1.4 **(b)**.

A final complication arises from the behavior of the boundary layer on a CFT foil. Lift and drag forcing, as well as the timing and nature of flow separation and reattachment at high angles of attack depends on if the boundary layer is primarily turbulent, laminar, or a combination of the two (laminar transitioning to turbulent). The nature of the boundary layer is dependent on the local inflow velocity and velocity history, the turbine blade size, and the fluid kinematic viscosity (in other words, the flow history and local Reynolds number). Intractable for analytical models, this presents a challenge to even the most advanced CFD simulations, since the boundary layer must be completely resolved to capture this behavior correctly. Unsteady Reynolds-averaged Navier-Stokes models have been shown to consistently miscalculate blade forcing and performance[119, 67]. Large-eddy and detached-eddy simulations have been shown to be more successful[67], though these are currently likely to be prohibitively expensive for large parameter sweeps. The boundary layer physics responsible for these difficulties are discussed more thoroughly in section 3.4.

The preceding fluid dynamic complexities make CFTs a rich topic of study and motivate the use of laboratory experiments as the method of investigation.

1.2.4 Equation of Motion and Performance Evaluation

Because this body of work is concerned with the fluid dynamic performance of CFT rotors, the performance metric used in this work is the amount of kinetic energy in the fluid that is converted to rotational mechanical energy by the rotor. The performance of bearings, generators, gearboxes, and electrical conversion systems are crucial to the overall power output of a CFT system, but the design of these components is outside the scope of this work. Therefore, the equation of motion for a CFT rotor takes on the fluid-centric form of

$$\dot{\omega}(t)I = \tau_{\mathrm{f}}(t) + \tau_{\mathrm{c}}(t). \tag{1.7}$$

Here $\dot{\omega}$ is the turbine angular acceleration and I is the mass moment of inertia of all rotating components. τ_{f} encompasses all fluid forcing on the turbine rotor, including torque in the direction of rotation due to foil lift, drag on foils and other turbine components, added mass, damping, and any other fluid-rotor interaction. τ_{c} is the torque imparted on turbine rotor by anything other than the fluid. This includes the power take-off or electro-mechanical control system, as well as bearing and other non-fluid sources of frictional losses. The fluid power generated by the turbine rotor is then

$$P(t) = \tau_f(t)\omega(t). \tag{1.8}$$

For time averaged data where the angular velocity of the turbine is periodic or constant and the average is taken over an integer number of rotations, $-\tau_{\mathrm{c}}(t)$ can replace $\tau_f(t)$ in the above equation. Details and proof are given in section 2.2.2, $-\tau_{\mathrm{c}}(t)$. The energy conversion efficiency, or power coefficient, is the turbine power normalized by the total fluid power incident on the turbine, or

$$C_P(t) = \frac{P(t)}{\frac{1}{2}\rho U_\infty^3(t) A}, \tag{1.9}$$

where ρ is the fluid density, and A is the area normal to the freestream direction swept by the turbine rotor. For a constant radius CFT, $A = HD$, where D is the rotor diameter, and H is the rotor height or span. A CFT performance curve consists of a series of C_P measurements made for a sequence of TSRs, Eq. (1.5). The TSR is usually incremented by changing the turbine rotation rate. The rotation rate is incremented by either direct closed-loop control of the turbine rotation rate (velocity control) or indirectly by varying τ_{c} (torque control). The peak of the C_P-TSR curve indicates the peak performance of the specific rotor geometry under the tested inflow conditions and control scheme. Because the free stream velocity, U_∞, is generally measured at a location upstream of the turbine rotor, care must be take in computing time average C_P due to the advection time of free stream turbulence. Details are given in 2.3.5.

1.3 History of CFT Research

The following chapters each describe existing literature pertinent to the specific aspects of CFTs under consideration. However, it may be useful to the reader map out historical CFT research in broad strokes. The inventor of lift-based CFTs was french engineer Georges Jean Marie Darrieus, who patented the concept in 1931[52]. The first published experiments, consisting of wind-tunnel testing of a vertical-wind turbine with troposkein blades, were performed in Canada in the early 1970s[180, 179]. Shortly thereafter, Sandia National Labs began a multi-decade campaign of experimental vertical-axis wind turbine research [26, 201] with some additional contribution from the National Aeronautics and Space Administration [137]. This early research focused mainly on two- and three-bladed CFTs with troposkein blades, a shape designed to minimize internal stresses. The culmination of this research was the construction of the 34 m Sandia National Labs vertical-axis wind turbine[8]. These technological developments were transferred to the FloWind Corporation, who built and installed over 500 vertical-axis turbines in California in the mid 1980s. These turbines struggled from premature structural failure due to fatigue of the blade-tower connection joints[188]. Academic research on CFTs continued through the 1980s, with perhaps the first experiments using water as the working fluid performed by P. Fraunie et. al[70]. Few publications date from the 1990s and early 2000s, with the exceptions of[174, 71, 196, 175, 120]. Notably, A. Gorlov introduced the concept of helically swept blades, reducing oscillatory loading and improving self starting characteristics[76]. Starting in the late 2000s, a resurgence of academic interest in CFTs for small wind and hydrokinetic applications occurred, with more than a dozen articles published between 2007 and 2009. The well-publicized work of J. Dabiri[202, 48], suggesting that arrays of CFTs could outperform arrays of AFTs, elevated academic interest in CFTs even further. This heightened interest has continued through the present day. An excellent review of large vertical axis-wind turbine prototypes has recently been published[132], and the vertical-axis wind turbine page of P. Gipes *Wind Energy for the Rest of Us* website provides a thorough though perhaps overly pessimistic overview of attempts to commercialize small vertical-axis wind turbines[73]. Several companies are attempting to bring CFTs to market through harnessing hydrokinetic energy, including Ocean Renewable Power Company, based in Maine, USA, and Instream Energy Systems of Vancouver, British Columbia, Canada. Additional recent CFT investigations have been inspired by their potential for offshore wind applications [81, 28], due the added stability of a down-tower generator , with several companies working toward commercialization in this arena, such as Sweden-based SeaTwirl.

1.4 Scope of Work

The body of work documented in this manuscript aims to improve the performance of and increase our understanding of CFTs through experimental investigation and optimization. Chapter One covers the methods used commonly across all experiments. Chapter Two covers experiments pertaining to the geometric optimization of CFT rotors. Chapter Three investigates the a CFT wake and presents a new technique for uncovering wake physics. Chapter Four introduces two new CFT control methods, one for individual turbines and one turbine arrays.

Chapter 2

METHODS OF INVESTIGATION

Perhaps the only reassuring aspect of experimental investigation is that there is no question whether the physics of the system are accurate. The difficulty is in whether the physical system measured is a useful one, and in the accuracy and precision of these measurements. Compared to computational work, the time-consuming portion of investigation is shifted from the run-time to design and verification of the measurement setup. However, once fine-tuned, large parameter spaces can be explored rapidly. For example using the system detailed below, a performance curve of a single turbine can be collected in a half hour, including installation and removal of the rotor. In contrast, a thirty-second run corresponding to one point on a performance curve might cost a week of computation time on a modern workstation using a CFD model appropriated for this type of flow.

The work presented here has been in part limited by the types of parameters that are easiest to iterate experimentally. For example, control parameters can be changed on-the-fly, allowing for fast parameter sweeps or real-time optimization. In contrast, parameters like blade helix angle and blade cross-section profile require fabrication of a new rotor for each data point. Parameters such as these are most likely to benefit from CFD analysis, since fabrication time and cost may approach that of simulation.

2.1 Flumes

The majority of experiments presented here were performed in flumes. Flumes are artificial channels that usually use pumps to recirculate water, creating flow through a testing section. Performing experiments in flumes rather than in wind tunnels has a number of advantages. First, a higher Reynolds number can be achieved with a smaller, easier to manufacture turbine rotor and at a lower flow velocity. For example, a 0.2 m diameter turbine in 1.0 m/s of water flow has approximately the same diameter Reynolds number, Re_D, as a 0.5 m diameter wind turbine in 8 m/s wind. Second, forces and torques are higher than in air flow for turbines with equivalent Reynolds numbers, making high signal-to-noise ratio measurements easier. For the identical Reynolds number cases described here, forces are 2.1 times higher in water than in air. Third, all flow and turbine activity is slower. Measurements can be lower frequency, control loops can be slower, and forces and vibrations due to centripetal forces are reduced.

Challenges specific to flume testing include the difficulty of placing electronics underwater, corrosion, free surface effects, and the temperature dependence of water viscosity. When the flow velocity is large compared to the square root of channel depth times the gravitational acceleration, free surface waves develop. The resulting wave orbitals may influence the flow incident on the turbine, impacting performance or degrading estimation of the true freestream velocity. Closed-loop temperature control is necessary to hold the viscosity, and thus Reynolds number constant across experiments.

Experimentalists testing turbines in wind tunnels or flumes face a conundrum. On one hand, the size of the model should be maximized, such that the Reynolds number is as close as possible to that of commercial-scale turbines. However, when a large fraction of the test section area is occupied by the turbine rotor, the upstream pressure is increased and more flow is forced through the rotor. The fraction of the area swept by the turbine over the test section cross-sectional area is called the blockage ratio, given by

$$B_r = \frac{HD}{A_{\text{test section}}} \tag{2.1}$$

for a CFT turbine rotor. The elevated flow through the rotor at large B_r boosts performance above that of unconfined flow conditions. Generally speaking, blockage should be kept below 5% to reflect unconfined performance [125, 161]. Most of the experiments performed here have blockage ratios greater than 5%. For this reason, results are presented in a comparative manner, such that performance gains and decreases are compared at the same blockage value. One method avoiding this issue is to increase the Reynolds number through increasing the fluid density, such as in a high-pressure wind-tunnel[129]. However, such facilities are uncommon.

2.1.1 University of Washington Tyler Flume

The UW Tyler flume has a test section measuring 0.76 m wide and 4.88 m long. The standard operating depth for these experiments was 0.475 m with the water flowing. This flume has an unusually large contraction ratio of 4.0. Combined with a flow straightener and resistive meshes, this results in a turbulence intensity, TI, between 1.5% and 3%, given by

$$TI = \frac{\sqrt{\frac{1}{3}\left(\langle u'^2\rangle + \langle v'^2\rangle + \langle w'^2\rangle\right)}}{\left\langle\sqrt{U^2 + V^2 + W^2}\right\rangle} \tag{2.2}$$

where $[U, V, W]$ are the total velocity vector components and $[u^{'}, v^{'}, w^{'}]$ are the fluctuating velocity components. In this manuscript, $\langle f\rangle$ denotes the temporal mean of the quantity f. Variable frequency drives on the flume pumps enable computer controlled flow velocity up to approximately 1.1 m/s. This flume has both heating and cooling capabilities allowing temperature control to within ±0.1° C. Using the standard turbine rotor of this work (see section 2.4), the blockage ratio is 11%.

2.1.2 Bamfield Marine Science Center Flume

The Bamfield Marine Science Center Flume consists of a 10 m long test section with no stilling basin (contraction ratio of 1). The flume width is 2.0 m, and the standard dynamic depth used was 0.73 m, resulting in a blockage ratio of 2.8%. The turbulence intensity was between 2.0% and 3.5%. The maximum possible flow rate was 0.6 m/s. A refrigeration system provided temperature control to within ±0.5° C.

2.2 Turbine Test Setup

The primary system used for turbine performance measurement and control is shown in Fig. 2.1. A Yaskawa SGMCS-02B or SGMCS-05B direct mount servomotor was used to

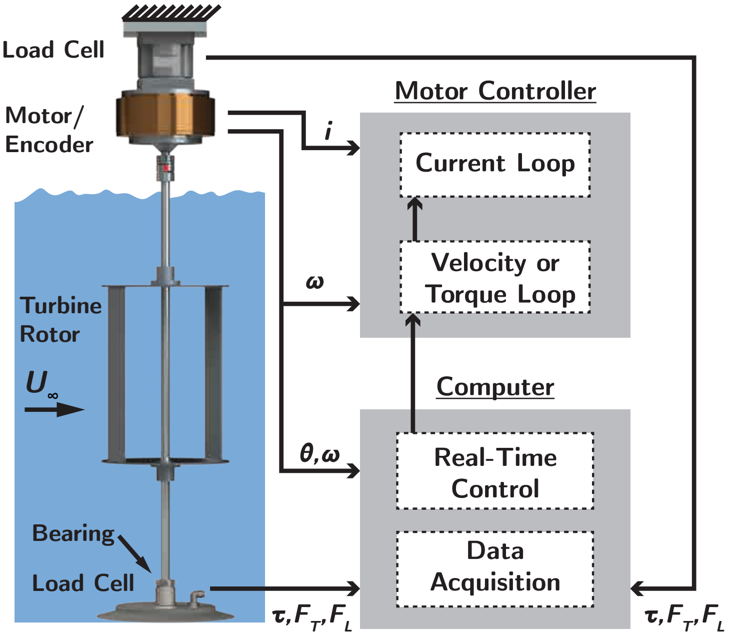

Figure 2.1: Turbine experimental control and measurement system diagram. i indicates current flow from the servomotor to the controller, where it is dissipated in a resistor. Not pictured, an acoustic doppler velocimeter is located $5D$ upstream centered on the rotor, providing freestream velocity data.

control the turbine rotation. Coupled with a Yaskawa SGDV-05B3C41 controller, this allows for angular velocity or torque control, and allows electrical energy to flow from the servomotor to the drive (generation mode) or from the drive to the motor (motoring mode). The motor also has an internal encoder with over one million counts per revolution. The turbine was mounted directly to the face of this motor via a flexible shaft coupling. The motor is mounted to the flume superstructure via ATI Mini45 six-axis load cell. This cell measures all reaction forces and torques on the servomotor. The turbine drive shaft is 12.7 mm in diameter and terminates at a bearing near the bottom of the flume. This bearing is supported by an ATI Nano25 six-axis load cell, which measures the reaction forces on the lower bearing. The Nano25 load cell is mounted to the flume bottom via a vacuum plate.

The turbine control architecture is also illustrated in Fig. 2.1. Control and measurement is handled using a MATLAB Simulink model running on the MATLAB Realtime Desktop kernel on a PC. The control and acquisition I/O is through National Instruments PCIe-6351 and/or PCIe-6353 data acquisition (DAQ) boards. The turbine velocity or torque command is sent to the motor controller via an analog voltage. On-board counters on the DAQ keep track of the turbine angular position from the motor encoder signal. All electrical interfaces between the DAQ system and the motor drives are isolated to reduced electrical noise. The DAQ cards are also used to measure the amplified load cell voltages. The control loop and data collection frequency was 1kHz. The Simulink Realtime Desktop model allows for either open loop, or closed loop control of the turbine based on incoming measurements.

The freestream velocity was measured using a Nortek Vector acoustic Doppler velocimeter (ADV) at a sample rate of 64Hz. The sampling volume was positioned five diameters upstream from the turbine rotation axis, and centered on the turbine swept area in the vertical and cross-stream directions.

2.2.1 Torque and Power Measurement

Because it can be a topic of some confusion, it is worth detailing how the above experimental setup is used to derive the fluid-only torque and power. The torques acting on the turbine rotor in this setup may be separated into three components, as illustrated in Fig. 2.2. First is the torque applied by the servomotor to the turbine rotor, τ_{c}. During power generation, this torque is applied opposite to the direction of the turbine rotation. Second is the torque applied on the turbine rotor by the fluid, τ_{f}. This torque includes forces that are beneficial, pushing the turbine in the direction of rotation, as well as forces that are detrimental, such as drag losses that act to slow the turbine down. Finally, the lower bearing imparts a small parasitic loss on the turbine, τ_{b}. Therefore the equation of motion becomes

$$\tau_{\mathrm{c}} + \tau_{\mathrm{f}} + \tau_{\mathrm{b}} = I\dot{\omega}. \tag{2.3}$$

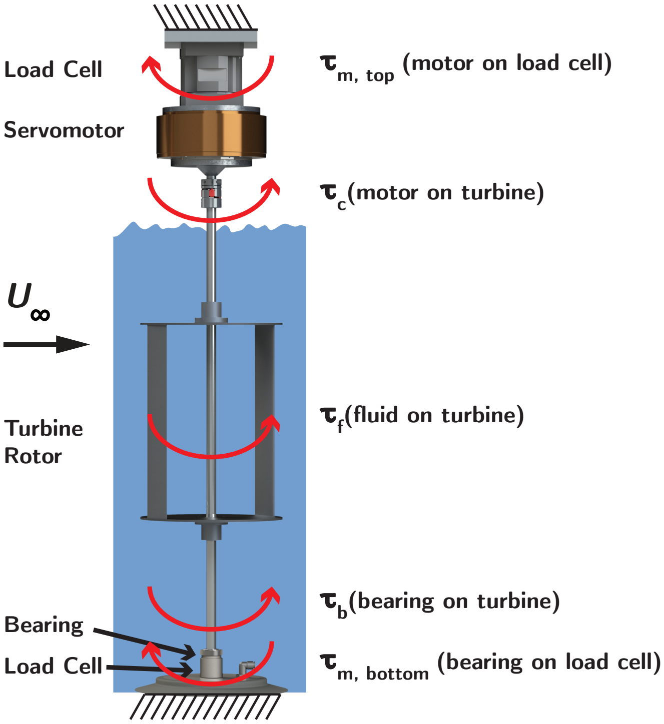

Figure 2.2: Free-body diagram illustrating the torques and reactions torques present in the experimental setup.

A brief aside on the control torque: This analysis does not consider the individual torques present in the servomotor, such as the torque due to the magnetic field applied to the rotor and the parasitic torques due to the motor bearings. These torques are all lumped into the single term, τ_c, which describes the total torque applied to the rotor by the servo motor. The motivation for this choice is to study the mechanical efficiency of the turbine rotor without including the efficiency of the servomotor. Therefore, the efficiencies presented in this study do not include losses in the servomotor system.

To consider how we are able to measure the aggregate control torque, we must consider the free body diagram of the servomotor stator, which does not rotate. The stator experiences two external torques. First is the torque equal and opposite to that applied to the servomotor rotor, and subsequently to the rigidly-connected turbine rotor. This torque is the electromagnetic force, minus bearing losses. This is equal and opposite to τ_{c}, the torque applied to the turbine by the servomotor. The second torque on the servomotor stator is the reaction torque between the servomotor and the upper load cell (in the above figure, this is $\tau_{\text{m, top}}$). Since the stator of the servomotor is stationary and does not accelerate, we then have

$$-\tau_{\mathrm{c}} + \tau_{\text{m, top}} = 0. \tag{2.4}$$

This means that the torque measured by the top load cell is equal to the aggregate control torque. Consequently, if the turbine was spun at constant velocity in a vacuum (such that $\tau_{\mathrm{f}} = 0$) and the lower bearing was frictionless ($\tau_{\mathrm{b}} = 0$), the upper load cell would measure zero torque. In this scenario, under constant velocity control mode, any losses internal to the servomotor are compensated by an input of external current by the servomotor controller, resulting in net zero force applied to the turbine and motor rotor, and no reaction torque is measured by the load cell.

Now let us return to the equation of motion for the turbine rotor (2.3). We have just shown that $\tau_{\mathrm{c}} = \tau_{\text{m, top}}$. Similarly, the reaction torque of the lower bearing on the lower load cell is equal to the parasitic torque the bearing applies to the turbine rotor, giving $\tau_{\mathrm{b}} = \tau_{\text{m, bottom}}$. This gives

$$\tau_{\text{m, top}} + \tau_{\mathrm{f}} + \tau_{\text{m, bottom}} = I\dot{\omega}. \tag{2.5}$$

To consider the torque on the turbine rotor due to fluid forcing and acceleration alone, we isolate these terms:

$$\tau_{\text{m, top}} + \tau_{\text{m, bottom}} = I\dot{\omega} - \tau_{\mathrm{f}}. \tag{2.6}$$

The rotor mechanical torque (fluid and acceleration torques only) in terms of torques measured in this experiment is then

$$\tau \equiv \tau_{\mathrm{f}} - I\dot{\omega} = -\tau_{\text{m, top}} - \tau_{\text{m, bottom}}. \tag{2.7}$$

The mechanical fluid power generated by the turbine, with non-fluid losses eliminated, is then

$$P = \tau\omega = \left(\tau_{\mathrm{f}} - I\dot{\omega}\right)\omega = -\left(\tau_{\text{m, top}} + \tau_{\text{m, bottom}}\right)\omega. \tag{2.8}$$

2.2.2 Acceleration and deceleration power

The energy generated by the turbine rotor over one revolution is given as the time integral of equation (2.8) as

$$E_{\text{per cycle}} = \int\limits_{\text{cycle}} \tau(t)\omega(t)\; dt \tag{2.9}$$

or, using Eq. 2.7,

$$E_{\text{per cycle}} = \int\limits_{t_0}^{t_0+T} \tau_{\text{f}}(t)\omega(t) dt - \int\limits_{t_0}^{t_0+T} I\omega(t)\dot{\omega}(t) dt \tag{2.10}$$

where T is the rotation period. In the second integral term, $\dot{\omega} = \frac{d\omega}{dt}$ is substituted, and the limits modified appropriately:

$$E_{\text{per cycle}} = \int\limits_{t_0}^{t_0+T} \tau_{\text{f}}(t)\omega(t) dt - \int\limits_{\omega(t_0)}^{\omega(t_0+T)} I\omega(t) d\omega \tag{2.11}$$

As long as the angular velocity is periodic, such that $\omega(t_0) = \omega(t_0 + T)$, the second integral is always zero. Additionally, this integral goes to zero for any angular velocity profile, periodic or not, that takes on the same value as at t_0 some point in the future. This means that any controller which results in a periodic acceleration and deceleration of the turbine only contributes to the mechanical energy harvested per cycle by modifying τ_{f}. If under velocity control, the fluid torque goes negative, the servomotor may be required to inject energy into the turbine (act as a motor rather than a generator) during some parts of the cycle. This energy is recovered by decelerating the turbine during other portions of the rotation. As will be detailed in the next section, this function can also be performed by increasing the mass moment of inertia of the rotor, and using the rotor as a kinetic energy storage device. Under torque control, τ_c can be regulated to always resist the rotor rotation, eliminating the possibility injecting energy into the turbine.

2.2.3 $\dot{\lambda}$ Scaling: An Argument for Velocity Control

[1] The two main control methods for laboratory turbines are to spin the rotor at a constant angular velocity, by varying the control torque in a closed-loop control system, or to hold the control torque constant and allow the angular velocity to vary. Under torque contrlo, where the turbine angular velocity is not prescribed, the blade kinematics, and thus fluid forcing, depend on the ratio of the turbine mass-moment of inertia and the sum of the fluid and control torques on the rotor. This can be shown by rearranging the turbine equation of motion Eq. (1.7), as

$$\dot{\omega} = \frac{\tau_h - \tau_c}{I} = \frac{\Delta\tau}{I} \tag{2.12}$$

where here we consider τ_c to include all external (non-fluid, non-accleration) torques on the rotor. This calls into question the validity of extending results of laboratory experiments performed with a control scheme that allows the rotation rate to vary ($\dot{\omega} \neq 0$), such as resistive torque control, to larger turbine scales, such as those suitable for commercialization. It is then useful to explore how the variation in rotation rate is expected to change as turbine size is increased.

Consider the non-dimensional form of eq (2.12),

$$\frac{I\dot{\omega}}{\frac{1}{2}\rho U_0^2 AR} = \frac{\Delta\tau}{\frac{1}{2}\rho U_0^2 AR} = \Delta C_Q. \tag{2.13}$$

Solving for the angular acceleration yields

$$\dot{\omega} = \frac{1}{2J}\rho U_0^2 AR\Delta C_Q. \tag{2.14}$$

For a constant freestream velocity, the angular acceleration may be expressed in terms of the derivative of the tip-speed ratio as

$$\dot{\lambda} = \frac{\dot{\omega}R}{U_0}, \text{ or } \dot{\omega} = \frac{\dot{\lambda}U_0}{R}. \tag{2.15}$$

---

[1] A similar argument to the following appears in the forthcoming publication *Comparison of Cross-Flow Turbine Performance under Torque-Regulated and Speed-Regulated Control* by B. Polagye, B. Strom, D. Forbush, H. Ross, and R. Cavagnaro

Substitution into the previous equation, and solving for the rate of change of the tip-speed ratio yields

$$\dot{\lambda} = \frac{\frac{1}{2}\rho U_0 A R^2 \Delta C_Q}{I}. \tag{2.16}$$

The turbine frontal area is

$$A = 2RH \tag{2.17}$$

and the turbine height and radius are related through the aspect ratio (A_r) by

$$H = 2RA_r \tag{2.18}$$

Equation. (2.16) then becomes

$$\dot{\lambda} = \frac{2\rho U_0 R^4 A_r \Delta C_Q}{I}. \tag{2.19}$$

The mass moment of inertia, I, may be approximated as the sum of point masses (the blades) with total mass m, placed at a radius R from the rotation axis, or

$$I \approx \frac{1}{2}R^2 m, \tag{2.20}$$

where the blade mass can be expressed using the blade cross-sectional area A_b, the blade material density ρ_b, and the number of blades N as

$$m = NA_b H\rho_b, \tag{2.21}$$

yeilding

$$I \approx \frac{1}{2}R^2 NA_b H\rho_b. \tag{2.22}$$

The blade cross-section area can be expressed as

$$A_b = c^2 t^*, \tag{2.23}$$

where t^* is the non-dimensional mean blade thickness, as a fraction of the chord length, c. The mass-moment of inertia is then approximated by

$$I \approx \frac{1}{2}R^2 Nc^2 tH\rho_b. \tag{2.24}$$

Using the aspect ratio relation, eq. (2.18), and the non-dimension chord-to radius ratio (c_r) relation

$$c = c_r R \tag{2.25}$$

to eliminate H and c yields

$$I \approx A_r c_r^2 t^* N \rho_b R^5. \tag{2.26}$$

The time derivative of the tip-speed ratio (eq. (2.19)) then becomes

$$\dot{\lambda} \approx \frac{2\rho U_0 \Delta C_Q}{c_r^2 t^* N \rho_b R}. \tag{2.27}$$

It will be assumed that the non-dimensional turbine geometric parameters chord-to-radius ratio (c_r), foil thickness ratio (t^*), and number of blades (N) will remain constant between the laboratory and commercial-scale turbines. Additionally, the non-dimensional torque coefficient (ΔC_Q), the working fluid density (ρ) and the blade material density (ρ_b) are assumed to remain constant across scales. This results in the proportionality

$$\dot{\lambda} \propto \frac{U_0}{R}. \tag{2.28}$$

When scaling from the laboratory to full-scale turbines, the ratio of laboratory measured tip-speed ratio variation to that experienced by a full-scale, commercial turbine is then

$$\frac{\dot{\lambda}_{\text{lab}}}{\dot{\lambda}_{\text{full}}} \propto \frac{U_{0,\text{lab}}}{U_{0,\text{full}}} \frac{1}{S}, \tag{2.29}$$

where S is the geometric scaling factor of the laboratory turbine, or

$$S = \frac{R_{\text{lab}}}{R_{\text{full}}}. \tag{2.30}$$

Thus, we expect variations in tip-speed ratio to be proportional to changes in the freestream velocity and inversely proportional to the turbine scale. Results utilizing constant resistive torque control of a small radius, laboratory-scale turbine may then experience significantly larger swings in tip-speed ratio, resulting in different blade kinematics than large, commercial turbines. Several strategies may be taken to alleviate this issue. First, very low values of

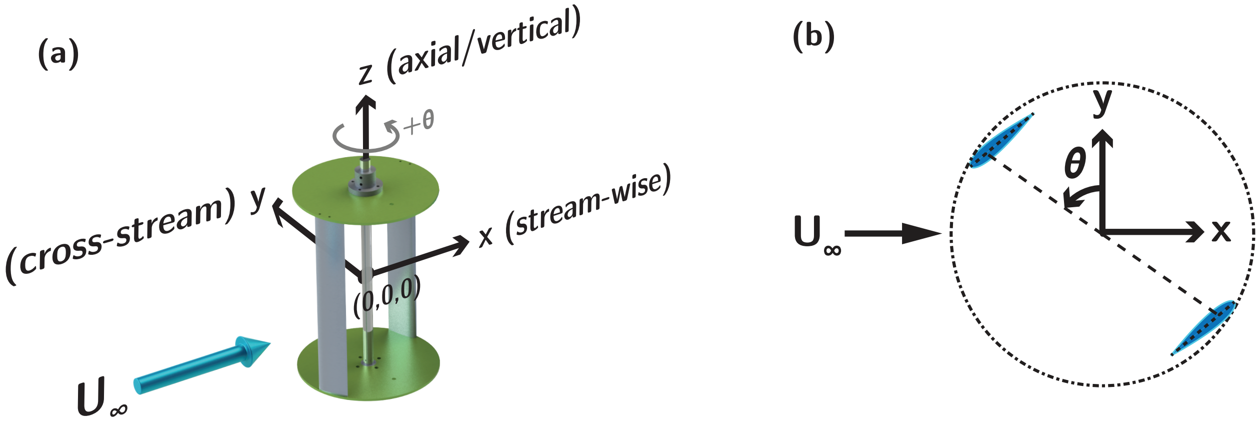

Figure 2.3: **(a)** Isometric and **(b)** cross-section views of the turbine coordinate system used in this work.

freestream velocities may be used. However, this poses difficulty in achieving representative Reynolds numbers and in measuring very small values of hydrodynamic torque. Second, the mass-moment of inertia of the turbine may be artificially increased, either through addition of mass to the rotor, or through applying a torque opposite the direction of angular acceleration via a real-time measurement and control system. Care must be taken that additional rotor mass does not interact with the working fluid. Finally, rotors may be operated under constant angular velocity control ($\dot{\lambda} = 0$) rather than torque control. This will approximate the kinematic behavior of the rotor as the turbine size becomes very large ($\frac{1}{R} \rightarrow 0$).

2.3 Data Post-Processing

2.3.1 Turbine Coordinate System

The standard coordinate system in which all following results are presented is illustrated in Fig. 2.3. The origin is on the axis of rotation, centered relative to the turbine height. Positive $\widehat{z}$ direction points towards the flume water surface. The $+\widehat{x}$ direction points downstream, and so is nominally parallel to the freestream vector. The $\widehat{y}$ direction follows, using a right-hand coordinate system. Positive rotation and torque direction is defined by the $+\widehat{z}$ axis, so is counter-clockwise when viewed from above. In this work, the $+\widehat{x}$ direction is referred to as 'streamwise' while the $+\widehat{y}$ direction is referred to as 'cross-stream'. Note that in many publications, the $+\widehat{y}$ direction is referred to as 'spanwise' (for example [5]), but because in the case of CFTs the blade span extends in the $+\widehat{z}$ direction, this nomenclature is felt to be confusing.

2.3.2 Load Cells

Load cell measurements were converted from amplified strain-gauge voltages to forces and torques in the default coordinate system of each load cell using factory provided calibration matricies. Because there was no means of registering rotational orientation of the load cells about the $\widehat{z}$ axis during setup, a rotational correction was applied to the F_x and F_y forces. This correction was derived by applying a force in a known direction (usually $+\widehat{x}$), then calculating the rotation matrix necessary to transform the measured x and y forces onto the applied force vector. The sum of the transformed forces measured by the top and bottom load cells gives the fluid force applied to the turbine rotor. The fluid torque was calculated as given in section 2.2.1.

2.3.3 Encoder Data

The encoder counts were converted to radians. Because there was no mechanism for maintaining alignment of the turbine rotor and the motor between rotor change-outs, the $\theta = 0$ turbine position was calibrated using an alignment pin mounted to a removable arm. The alignment pin registered in a hole in the turbine blade mounting structure.

Differentiation of encoder data to derive turbine velocity and acceleration poses a challenge. The measurement is discretized twice over. Once due to the spatial discretization of the encoder counts between $\theta = 0 \rightarrow 2\pi$. Second, though the counter chip onboard the DAQ registers changes in the encoder count nearly instantaneously, the Simulink data acquisition system only samples this value every 1 ms. This adds a layer of temporal discretization to the measurement. Low order finite-difference differentiation of the resulting measurement yields noisy derivatives that do not reflect the actual activity of the system. The solution used here is to differentiate an analytical polynomial fit to a window of position measurements. The standard used for this experiment is a second-order polynomial fit to a window of 20 time points. Since a new polynomial is fit for every datapoint, this can be a computationally intensive process. A fast vectorized method of performing this computation has been developed, and because it may be useful to other users of encoders, is given in A.1.

2.3.4 ADV Data

ADV measurements are prone to sparse noise, usually referred to as spikes. Goring and Nikora [75] presented an algorithm for identifying ADV data spikes, which was later improved by [199] and [134]. This method employs a 3D phase space comprised of the velocity measurement and its first two derivatives. A 3D ellipsoid is drawn in this space, which extends along each axis a distance of

$$r_i = \hat{\sigma}(x_i)\sqrt{2 \ln N}, \tag{2.31}$$

where $\hat{\sigma}$ is the standard deviation, x_i is the measurement of interest (velocity, or its first or second derivative), and N is the number of measurements in the time series. This corresponds to the maximum expected value for a normal, random variable. Data points that fall outside this ellipsoid are identified data spikes. The algorithm is then run on the remaining data recursively until no more spikes are identified.

In this work it was found that the algorithm did not identify data spikes as efficiently when the freestream velocity had slow variations of any significant amplitude. This is likely because the ellipsoid is incorrectly expanded along the velocity direction. A solution, implemented here, is to perform the above algorithm on velocity data that has first been subjected to a high-pass filter, removing slow changes. Identified spike locations are then replaced in the original time-series using linear interpolation.

Spike identification was always performed on the raw beam velocities (before converting to real-world coordinates). Conversion to spatial coordinates spreads a spike occurring in a single beam across multiple channels, reducing the spike amplitude and making spike identification less effective.

2.3.5 Computation of Normalized Quantities

Force and performance data is presented normalized by the freestream velocity data. Ideally, the instantaneous values of these coefficients are calculated, then a time average can be taken. However, a number of challenges make this impractical for the data collected in this work. First, velocity fluctuations measured upstream do not interact with the turbine rotor until some time later, when this flow has advected downstream. Since the flow slows by an unknown amount as it approaches the rotor (streamwise induction), calculation of this advection time is difficult. Additionally, the structure of these fluctuations may have evolved during the advection time. Finally and most importantly, the Nortek Vector did not have an onboard clock that could be set accurately. Thus, freestream measurement time uncertainty was ± 1.0 second at best. For this reason, normalized coefficients were calculated by taking the mean of the numerator and denominator separately. For example, the mean power coefficient becomes

$$\langle C_P \rangle = \frac{\langle \omega(t)\tau(t) \rangle}{\frac{1}{2}\rho \left\langle U_\infty(t)^3 \right\rangle HD}. \tag{2.32}$$

Care is taken to average over an integer number of rotations in order to remove the influence of inter-cycle variations around the mean value.

Other normalized parameters of interest are the torque coefficient,

$$\langle C_Q \rangle = \frac{\langle \tau(t) \rangle}{\frac{1}{2}\rho \left\langle U_\infty(t)^2 \right\rangle HDR}, \tag{2.33}$$

and the stream wise and cross-stream wise force coefficients, referred to here as the thrust and lateral force coefficients, given by

$$\langle C_t \rangle = \frac{\langle F_x(t) \rangle}{\frac{1}{2}\rho \left\langle U_\infty(t)^2 \right\rangle HD}, \tag{2.34}$$

and

$$\langle C_\ell \rangle = \frac{\langle F_y(t) \rangle}{\frac{1}{2}\rho \left\langle U_\infty(t)^2 \right\rangle HD} \tag{2.35}$$

respectively.

2.3.6 Error and Variability

The quantity most often referred to in the following work is the turbine power coefficient, thus a brief error analysis of a sample measurement is presented. Uncertainty in the estimation of C_P is due primarily to the upper load cell torque and the freestream velocity measurements. The high resolution of the angular encoder and the relatively small values of lower bearing torque mean these measurements do not contribute significant uncertainty. The upper load cell had an accuracy of ± 1/1504 Nm, while the Nortek Vector had an accuracy of ± 0.5% and a resolution of ± 0.001 m/s. At a freestream velocity of 0.7 m/s, and operating at the peak C_P of 0.2 (both typical), the measured C_P has a maximum combined error of 1.3×10^{-4}. The standard acquisition time for one performance point was 30 seconds. For typical tip-speed ratios and flow speeds ranging from 0.4 m/s to 0.7 m/s, the number of full turbine revolutions in this time period range from 25 to 101. The cycle-to-cycle variance in C_P is typically 0.2% to 0.5%.

This analysis suggests a high level of precision of the turbine measurements over the course of a single test run. However, over the course of days to weeks as turbine rotors are removed and reinstalled, the performance of the rotors at identical flow and control conditions show C_P variation of approximately ±0.005, mainly at higher TSRs. The source of this variation is a topic of continued investigation. Possible options include slight variations in turbine rotor or mounting geometry, changes in the flow conditions, such as turbulence or viscosity, drift in load cell measurements due to thermal effects, or the use of a point free-stream velocity measurement to represent the velocity incident on the entire rotor area.

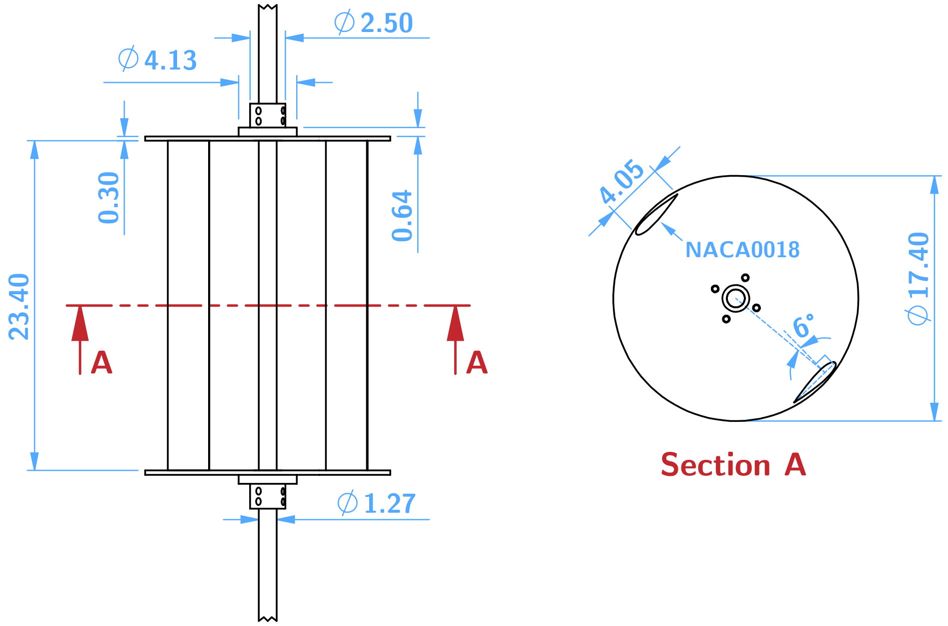

Figure 2.4: Dimensioned drawing of the standard experimental turbine. Dimension units are centimeters.

2.4 Turbine Geometry

The standard turbine geometry for these experiments, unless stated otherwise, is illustrated in Fig. 2.4. The rotor consists of two straight NACA0018 profile blades with chord lengths of 0.0406 m. The ends of the blades are mounted to the 0.012 m diameter center shaft via circular end plates. The blades are mounted at a preset pitch angle of six degrees (rotated six degrees about the quarter chord, leading edge outward). The turbine diameter is 0.172 m while the height (span) is 0.234 m. Non-dimensional geometric parameters, defined in section 3.1, are as follows: Solidity, $\sigma = 0.15$; chord-to-radius ratio, $c/R = 0.47$; and aspect ratio, $A_r = 1.36$.

Chapter 3

GEOMETRIC OPTIMIZATION

3.1 CFT Geometric Parameters

The parameters defining the major aspects of CFT rotor geometry are given in Table 3.1. For the purpose of comparing the relative geometry of rotors of different sizes, it is useful to define non-dimensional geometric parameters. These are given in Table 3.2. It should be noted that solidity, or the fraction of the turbine circumference occupied by blade, given by

$$\sigma = \frac{Nc}{2\pi R} \tag{3.1}$$

is not included in this list. Because two rotors can have different geometries but identical solidities (by varying N inversely with c), this parameter is of limited use when the objective is optimizing geometry. Additionally, as will be seen in section 3.4, making sense of CFT performance requires the consideration of N and c/R separately. For some CFT variants, the parameters given in Table 3.2 are not held constant. For example in designs with troposkein or canted blades, the radius varies as a function of position along the rotor height. In others, the blades may be tapered toward the tips, such that the chord length changes along the blades. Simultaneous optimization of all geometric parameters, including letting parameters vary in a single rotor, is a rather intractable task. This is especially true from an experimental standpoint where each rotor must be fabricated. In this work we seek to understand the phenomena by which design changes impact turbine performance. For this reason, only a subset of parameters is studied in this work. First, we restrict ourselves to the study of straight-bladed turbines ($\beta = 0$). Helical or canted blades have the potential to improve the self-starting capabilities of CFTs as well as smoothing loads and power output. However, because the blades in these designs occupy a range of azimuthal positions at the

R	Turbine radius
H	Blade span (rotor height)
c	Blade chord
N	Blade count
α_p	Preset blade pitch angle
-	Blade profile
β	Blade helix or cant angle
-	Blade end condition

Table 3.1: Dimensional turbine geometry parameters.

$\boldsymbol{c/R}$	**Chord-to-radius ratio**
A_r	Aspect ratio, $\frac{H}{2R}$
$\boldsymbol{N}$	**Blade count**
$\boldsymbol{\alpha_p}$	**Preset blade pitch angle**
-	Blade profile
β	Blade helix or cant angle
-	**Blade end condition**

Table 3.2: Non-dimensional turbine geometric parameters. Bolded quantities are those studied in this chapter.

same time, various different types of fluid-blade interactions can be occur simultaneously along a blade. This limits the usefulness of blade force measurements as an investigative tool. Additionally, unlike helical or canted blades, varying the preset pitch angle on a straight blade is trivial. Finally, it is likely that helical and canted blades induce significant axial flow in the rotor, further complicating already rich fluid mechanics. Blade profile shape is also not studied in this work. An optimization procedure based on fabricating and testing new profiles would be very time-intensive, though this may be soon possible with recent advances in additive manufacturing. The problem of optimizing the blade profile is better suited to CFD studies, and numerous investigations taking this approach to the topic have been published[51, 121, 22, 95, 109, 65, 18, 131, 40, 42, 50]. Notably, the optimized foil found by many of these studies does not differ substantially from a standard symmetric NACA0018 used in this work, for example see fig. 5 in [51]. The last geometric parameter left unstudied in this work is rotor aspect ratio. It is expected that performance per unit length of rotors will asymptote to that of an infinite-length rotor rather quickly. This is because the changes in performance are dependent on the blade aspect ratio (H/c). Above values of H/c of about

7-10, foil performance per unit length ceases to change[97]. For a rotor with even a large c/R of 0.5, this foil aspect ratio is achievable with a turbine aspect ratio of only $A_r = 1.75$ to 2.5. Therefore, it is felt that in the majority of applications, turbine aspect ratio will be inconsequential to the optimization of other rotor geometric parameters. The remaining parameters, bolded in Table 3.2, are those considered in the following studies. In the first section (3.2), the blade end condition is studied through the effect of mounting structures on performance. In the next section (3.3), the effect of preset pitch angle, α_p, is studied in isolation. In the last section (3.4) the effect of Reynolds number on optimal values of c/R, N, and α_p are studied, as well as some of the interdependence between these parameters.

3.2 Blade mounting structures

The following contains content from [185][1].

Little has been published concerning the implications of how CFT blades are affixed to the central shaft. While this concern may seem secondary to the rotor blade geometry, the blade support structure has the potential to heavily influence rotor performance. First, since the support member(s) must rotate with the rotor, they will necessarily produce some drag opposing the direction of rotation. Second, the support members may influence lift generation of the rotor blades. For example, on stationary foils, end-plates have been shown to be functionally similar to an increase in blade span by reducing tip effects[153]. Blade support structures placed near the tips of the blades may act as end-plates, reducing lift losses due to flow from the pressure surface to the suction surface around the end of the blade. Third, on aircraft wings, winglets are employed to reduce induced drag (drag due to lift[105]). Blade support structures have the potential to provide this function. Finally, differing blade support geometries may restrict span-wise flow in the turbine rotor to varying degrees, which may impact turbine performance by altering vortex formation during dynamic

---

[1] The work in this section has been published in AIP *Journal of Renewable and Sustainable Energy* (DOI:10.1063/1.5025322) and was co-authored with Brian Polagye and Noah Johnson[185]. The author lead all experiments and wrote the published manuscript. AIP allows the inclusion of copyrighted work in a thesis document.

stall.

Previous studies have individually demonstrated several strategies for mounting the blades to the central shaft. These include disks[76, 99], streamlined struts at the blade ends[174, 13], and streamlined struts at the mid-span or other intermediate positions[12, 85]. However, to date, few studies have made a systematic comparison of the implication of these choices. Goude, Lundin, and Leijon[78] considered the influence of differing numbers of struts using a double-multiple stream tube model based on tabulated values of the strut drag coefficient. Gosselin, Dumas, and Boureau[77] used an unsteady Reynolds-averaged Naiver-Stokes model to explore the effect of the adding end-plates to the blade tips of a CFT. Small end-plate resulted in turbine performance gains, since reduction in tip-losses outweighed end-plate drag losses. Rawlings et al.[151] experimentally found a slight increase in performance by applying disk and foil end-plates to the ends of a three-bladed CFT. Li and Calisal[112] experimentally compared a turbine with NACA 0012 struts positioned at the center-span and ends of the blades to a more blunt profile, positioned at 1/4 span from the ends. The increase in performance of the NACA 0012 struts was attributed to lower profile drag and a reduction in tip losses and induced drag. Additionally, disk and foil end-plates were tested resulting in a small increase in performance. Bachant et al.[15] experimentally compared NACA 0021 and cylindrical struts mounted at the mid-span of a three bladed CFT. The large drag on the cylindrical struts resulted in a negative turbine efficiency at all operating conditions. Strut drag was measured independently from turbine performance by rotating the turbines without blades.

By evaluating changes in turbine performance and drag on mounting structures, as well as analytical models, we provide a guide for selecting blade mounting geometry for CFT designs. These considerations are specific to lift-based CFTs since drag-based CFTs, such as a Savonius rotor, are configured to maximize drag.

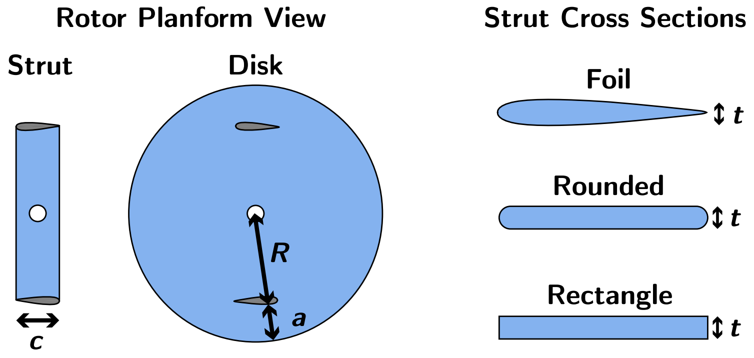

Figure 3.1: Blade mounting geometries. Strut versus disk configurations are at the left pane. The three strut cross-sections are shown at the right. Struts and disks are attached to the blade tips, with the exception of the mid-span strut (or "H") configuration, where the blades are mounted via a single foil at the mid-span. Table 3.3 lists the mounting geometries tested.

3.2.1 Methods

With the exception of the blade mounting structures, the turbine geometry, measurement methods, and analysis described in the methods chapter reflect those used in this work. All tests were performed in the UW Tyler Flume.

The ten blade connection geometries tested are illustrated in Fig. 3.1 and listed in Table 3.3. Six types of struts with a chord length equal to the blade chord were tested. These had either a symmetric 4-digit NACA foil, rounded, or rectangular cross-section. For each of these, two thicknesses were tested, $t = 0.16c$ and $0.08c$, where c is the chord length (equal for the blades and the struts). Additionally, three sets of $0.08c$ thick disks were tested. The first had a radius equal to that of the turbine. The second and third had radii that were expanded by $a = 0.5$ and 1.0 chord lengths. All mounting structures were attached at the ends of the turbine blades, with the exception of a final "mid-span strut" configuration, in which the blades were mounted to the center shaft at the mid-span using a 0.16c thick foil.

By incrementing the tip-speed ratio, a complete performance curve was generated for each mounting structure at four freestream velocities. These corresponded to blade chord

Planform	**Cross Section**	**Thickness**
Strut	Foil (NACA0008)	$0.08c$
Strut	Foil (NACA0016)	$0.16c$
Strut	Rounded	$0.08c$
Strut	Rounded	$0.16c$
Strut	Retangle	$0.08c$
Strut	Retangle	$0.16c$
Mid-span strut	Foil (NACA0016)	$0.16c$
Disk, $R^* = R$		$0.08c$
Disk, $R^* = R + 0.5c$		$0.08c$
Disk, $R^* = R + c$		$0.08c$

Table 3.3: List of mounting geometries tested. All geometries except the mid-span strut consist of two mounting structures, one at each end of the rotor. The Mid-span strut is a single mounting structure located at the mid-pane of the rotor. R^* indicates disk mounting structure radius.

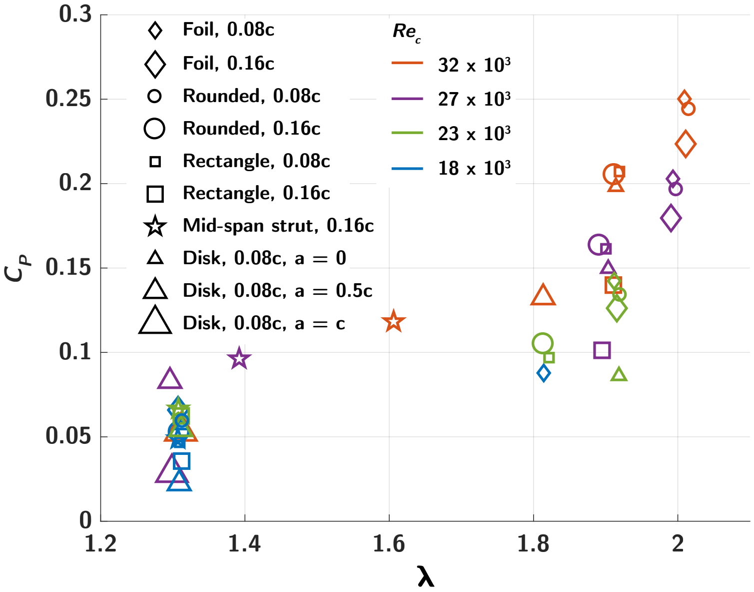

Figure 3.2: Peak turbine efficiency as a function of corresponding tip-speed ratio. Color indicates Reynolds number, Eq. (3.2). Legend indicates strut shape and thickness.

Reynolds numbers,

$$Re_c = \frac{cU_\infty}{\nu}, \tag{3.2}$$

of 18, 23, 27 and 32 $\times$ 10^3, where ν is the kinematic viscosity. Losses due to drag on the mounting structures were estimated by performing the same tip-speed ratio sweeps with the mounting structures alone, after the method of Bachant et al.[15].

3.2.2 Results

Figure 3.2 summarizes the peak performance of each blade mounting geometry as a function of Reynolds number and tip-speed ratio. Without exception, increasing Reynolds number increased turbine performance, as expected for transitional Reynolds numbers[15]. As shown in Fig. 3.3 (top), for poor-performing turbines, a secondary performance peak at $\lambda = 1.3$ dominates over the peak near $\lambda = 1.8$-2. Previous work has demonstrated that this low tip-speed ratio peak is due to a strong vortex-foil interaction[182],3.3. Increasing turbine performance generally corresponds to an increase in the tip-speed ratio at which peak efficiency occurs. At the highest Reynolds number, strut geometries with the greatest peak efficiencies were the 0.08c thick struts with foil and rounded cross sections ($C_P = 0.250$ and 0.244, respectively) followed by the 0.16c thick strut with a foil cross section ($C_P = 0.224$). These geometries performed best at all Reynolds numbers. The smallest disk ($a = 0$), thin rectangular strut, and thick rounded strut had the next best efficiency with similar relative performance at each Reynolds number. The expanded disks ($a = 0.5c, c$) and the mid-span strut configurations had the poorest performance at each Reynolds number.

3.2.3 Discussion

Taking a perturbation theory-like approach to the problem similar to Li and Calisal[112], the total efficiency of the turbine may be expressed as follows

$$C_P = C_{P,\,\mathrm{b}} + C_{P,\,\mathrm{m}} + C_{P,\,\mathrm{m\to b}} + C_{P,\,\mathrm{b\to m}} + C_{P,\ \mathrm{h.o.t.}} \tag{3.3}$$

Here $C_{P,\,\mathrm{b}}$ represents the ideal power that could be produced by the blades, regardless of the mounting structure or blade end condition (e.g., in the absence of tip losses). $C_{P,\,\mathrm{m}}$ represents the efficiency losses due to rotational drag on the mounting structures in a flow undisturbed by the turbine blades. The next two terms represent secondary effects. $C_{P,\,\mathrm{m\to b}}$ represents the influence of the mounting structures on blade performance. This includes a reduction in tip-losses and induced drag and influence on span-wise flow. $C_{P,\,\mathrm{b\to m}}$ encapsulates the effect of the blades on the drag experienced by the mounting structures, primarily due to changes in the local flow field induced by the blades. Further, higher-order terms ($C_{P,\,\mathrm{h.o.t.}}$) likely exist, but are not considered in this analysis.

If secondary and higher-order effects are small enough to be neglected, we can write

$$C_{P,\,\mathrm{b}} = C_P - C_{P,\,\mathrm{m}} - \cancelto{0}{C_{P,\,\mathrm{secondary}}}. \tag{3.4}$$

As in Bachant et al.[15], measurements of $C_{P,\,\mathrm{m}}$ have been taken directly by spinning the turbine in the flume without blades. Figure 3.4 shows this efficiency loss for the highest

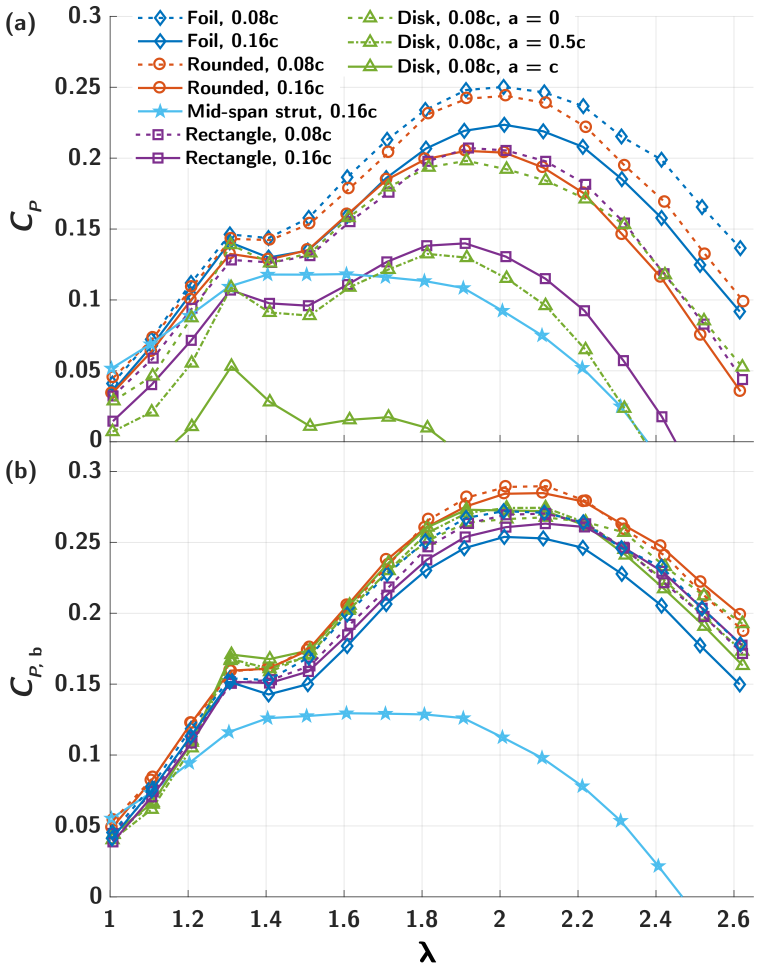

Figure 3.3: **(a)** Full turbine performance curves. **(b)** Performance curves with mounting structure rotational drag losses added back in as an estimate of blade-only performance. Both show performance for $Re_c = 32 \times 10^3$.

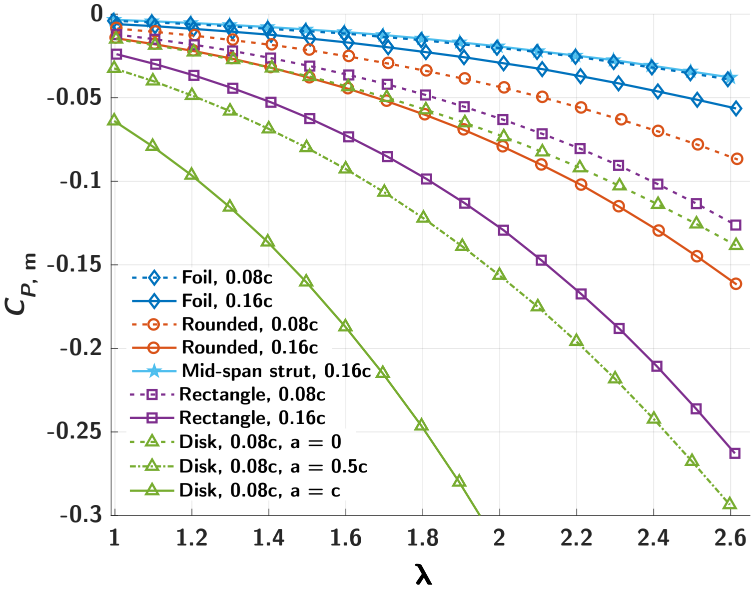

Figure 3.4: Efficiency loss due to mounting structure drag versus tip-speed ratio at $Re_c = 32 \times 10^3$.

Reynolds number tested. If the approximation that $C_{P,\,\mathrm{secondary}} \approx 0$ holds, $C_{P,\,\mathrm{b}}$ should be the same for all turbine configurations. Figure 3.3 **(b)** shows the performance curves resulting from this analysis. With the exception of the mid-span strut turbine, the blade performance curves are generally collapsed, though secondary effects are still responsible for some performance variation. Excluding the mid-span strut turbine, there is a 13% difference in the lowest and highest performing geometries at the peak of the curves, with discrepancy increasing with tip-speed ratio. The largest variation is between turbines with identical plan-form geometries (Foil, 0.16*c* versus Rounded 0.08*c*). These geometries likely have a similar end-plate and winglet effect on the blades, suggesting that $C_{P,\,\mathrm{m}\to\mathrm{b}}$ should be similar. Therefore, it is hypothesized that the most influential secondary effect for all geometries except the mid-span strut geometry is $C_{P,\,\mathrm{b}\to\mathrm{m}}$, that is, the changes in mounting structure drag due to the flow induced by the blades. Extending the disks beyond the radius of the turbine foils did not appear to increase blade performance. This suggests that shielding only

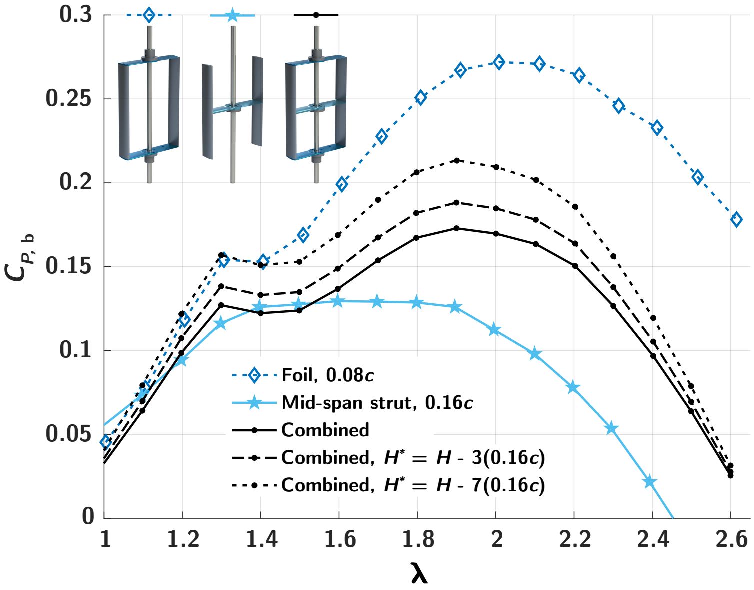

Figure 3.5: Blade performance (Eq. (3.4)) curves for the $0.08c$ thick foil struts, $0.16c$ thick mid-span strut, and a turbine with both. Black dashed lines show the performance of the turbine with both mounting structure types using a reduced value of the turbine height in the efficiency equation to account for loss of operable blade span due to the presence of the mid-span strut. Failure of these curves to approach the $0.08c$ foil curve indicates additional sources of power loss due to the presence of the mid-span strut.

the inside edge of the blade (suction side) is adequate to reduce tip losses.

Mid-Span Mounting Discussion

The mid-span strut turbine exhibits a much reduced total performance, remarkable considering mounting structure losses ($C_{P,\,\mathrm{m}}$) are equal to the best performing turbine (Foil, $0.08c$, Fig. 3.4) and that this is a common geometry for small vertical-axis wind turbines (i.e. “H-Darrieus”). When the mounting structure losses are accounted for, the $C_{P,\,\mathrm{b}}$ curve has a much broader peak, far below the other turbine geometries (Fig. 3.3, **(b)**). Since this turbine is the only geometry with free foil tips, it is likely that $C_{P,\,\mathrm{m}\rightarrow\mathrm{b}}$ dominates. Tip-losses are expected to be large as flow is no longer blocked between the suction and pressure sides of the blades. In addition, the free blade tips may introduce additional drag. To examine whether tip-effects are solely responsible for the decrease in performance of the mid-span strut turbine, an additional turbine geometry was tested, where the mounting structure included both the $0.08c$ thick foil struts at the ends of the blades and the $0.16c$ thick foil mid-span strut. A comparison of the foil $0.08c$, mid-span strut, and the combined turbine are given in Fig. 3.5. Here, the efficiency loss due to rotational drag, $C_{P\,\mathrm{m}}$, has been subtracted, leaving only the blade performance and secondary effects. Shielding the foil tips by using both types of mounting structures increases in blade performance over using the mid-span strut alone. However, the failure of the blade performance to match that achieved using the $0.08c$ foil struts alone suggests tip losses are only partially responsible for losses due to the presence of the mid-span mount. Since the mid-span strut attaches to the blades on the suction side of the blades, a central segment of the blades is unavailable for lift production. To explore this possibility, the area used in the denominator of the rotor efficiency equation (1.9) is reduced from $A = DH$ to $A = DH^*$, where $H^* = H - nt$, where t is the mid-span strut thickness, and n is the number of strut thicknesses unavailable for lift production at the mid-span of the blades. As apparent from Fig. 3.5, rescaling the blade efficiency in this manner does not account for all of the difference in blade performance between the $0.08c$ foil turbine and the combined turbine, even if three strut widths on either side of the mid-span strut are assumed to be unavailable for lift production (black, fine dashed line).

Given the preceding analysis, it seems that another mechanism, besides losses related to the free blade tips and an interruption of the lifting surface, must be partially responsible for the low performance of the mid-span strut turbine design. One hypothesis stems from the fact that the strut interrupts span-wise flow along the lifting surface. To see how this might be detrimental, first consider that the nominal (local) angle of attack on the foil varies as a function of azimuthal blade position, θ, as described in Eq. 1.3. In Fig. 1.2, for $\lambda = 2$, the nominal angle of attack for the upstream portion of the cycle (where the majority of power is generated) varies from less than zero to over 24 degrees. This virtual pitch-up maneuver to an angle well above the static stall angle can result in the roll up of a leading edge vortex (LEV), a phenomena known as dynamic stall[123]. The low pressure region in the LEV results in a temporary increase in lift above that possible with a foil at constant angle of attack. As reviewed in Wu, Vakili, and Wu[204], span-wise flow in the vortex core helps to stabilize the LEV, resulting in greater lift for longer duration before the vortex is shed. This suggests the introduction of a strut into the mid-span of the turbine blades could interrupt span-wise flow, causing premature shedding of the LEV and a reduction in lift.

Modeling Mounting Structure Drag

Analytical models for the drag on various mounting structure geometries may be a useful design tool for providing informed design decisions with limited prototype iteration. Here, models are compared to data collected by rotating the mounting structures without blades. Losses due to rotational drag of the central shaft are not included in the models. Losses due to the central shaft are measured separately by rotating the central shaft in the flow without blades or mounting structures at the appropriate freestream velocity and rotation rate. These small losses are then removed from mounting structure losses.

First the rectangular-planform struts (non-disk mounting structures) are considered. The relative velocity perpendicular to a strut section at a distance r from the rotation axis may be written as

$$U_{\text{rel}}(r,\theta) = \omega r + U_\infty \cos(\theta) + U_{\text{induced}}, \tag{3.5}$$

where θ is the blade position and is zero when the blade is traveling directly upstream. U_{induced} consists of any flow velocities induced by the blades and mounting structures. This term will be neglected for simplicity in subsequent analysis, with the assumption that the flow induced by the mounting structures is small. The resulting velocity vector incident on a strut is shown in Fig. 3.6. Taking a blade-element approach to calculating strut losses, the torque due to drag on a strut element of radial width dr is

$$\tau_d(r,\theta) = \frac{1}{2}\rho U_{\text{rel}}(r,\theta)^2 \operatorname{sgn}(U_{\text{rel}}) C_D(U_{\text{rel}}) L r dr. \tag{3.6}$$

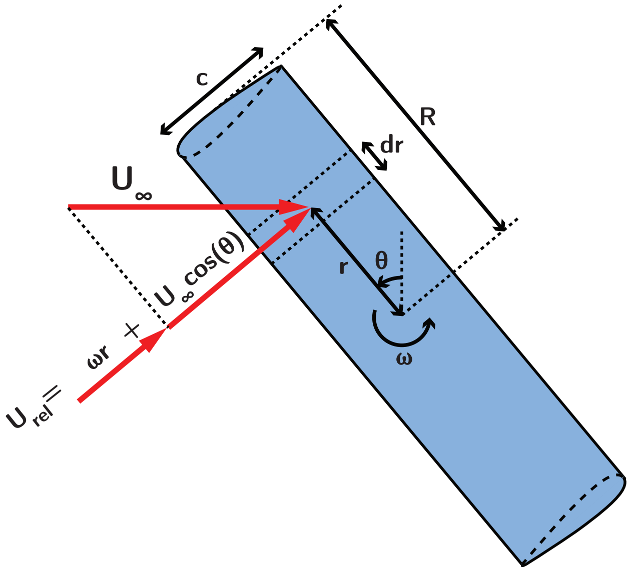

Figure 3.6: Strut drag model diagram. The freestream flow is from left to right. Red arrows indicate the components of the local flow velocity due to rotation and the freestream incident on a strut section of width dr.

Here L is the characteristic length used in the pertinent drag coefficient (C_D) definition (e.g., the chord length for a foil). The $\mathrm{sgn}(U_\mathrm{rel})$ term ensures the torque is applied in the direction of the relative velocity in case reverse flow is encountered.

At a specific azimuthal angle, θ, the total torque due to drag on one half strut is given by

$$\tau(\theta) = \frac{1}{2}\rho L \int_0^R U_\mathrm{rel}(r,\theta)^2 \, \mathrm{sgn}(U_\mathrm{rel}) C_D(U_\mathrm{rel}) r dr \tag{3.7}$$

The power loss is the mean of this value over all angles multiplied by the rotation rate, ω, and the number of half struts (twice the number of blades), or

$$P_\mathrm{strut} = \frac{\omega N \rho L}{2\pi} \int_0^{2\pi} \int_0^R U_\mathrm{rel}(r,\theta)^2 \, \mathrm{sgn}(U_\mathrm{rel}) C_D \left(U_\mathrm{rel}\right) r dr d\theta. \tag{3.8}$$

Rectangular Cross-Section Struts

Here the length scale used in the drag coefficient is $L = t$ where t is the strut thickness. Because the variation in drag coefficient with Reynolds number has been shown to be small[165], a constant value is used. A good approximation is to neglect the effect of reverse flow, since it occurs for only a small portion of the rotation, and if the tip-speed ratio is greater than 1, only near the center of the turbine where U_{rel} is small. Then the power loss integral can be solved exactly as

$$P_{\text{rect.}} = \frac{1}{4}\omega N \rho C_D t R^2 \left(\omega^2 R^2 + U_\infty^2\right). \tag{3.9}$$

Rectangular sections with a thickness over streamwise depth ratio of 5 have a drag coefficient of about $C_D = 1$ and drag coefficient trends lower as as this ratio increases[177]. The rectangular struts in this study had width over depth ratios of 6.4 for the $t = 0.16c$ strut and 12.8 for the $t = 0.08c$ strut. Drag coefficients of 0.95 and 0.92 respectively were found to best fit the data, consistent with expectations for an increasing thickness-over-depth ratio. Figure 3.7 shows the success of this model in predicting the power loss of the $0.08c$ rectangular strut, normalized by the fluid power incident on the turbine, as in the standard power coefficient definition. In addition, the assumption of a Reynolds number independent drag coefficient is supported by the independence of power loss from the Reynolds number.

Foil Struts

Equation (3.8) is applied to model the foil strut power loss. Here the length scale used in the drag coefficient definition is, by convention, the chord length ($L = c$) and the drag coefficient is allowed to vary based on the instantaneous Reynolds number of each radial element at each angular position, giving

$$P_{\text{foil}} = \frac{\omega N \rho c}{2\pi} \int_0^{2\pi} \int_0^R U_{\text{rel}}(r,\theta)^2 \, \text{sgn}(U_{\text{rel}}) C_D(r,\theta) r dr d\theta. \tag{3.10}$$

Tabulated values of the drag coefficient variation with Reynolds number were generated using the panel-method code XFOIL[55] with the turbulence intensity set to 1.5%, the same value

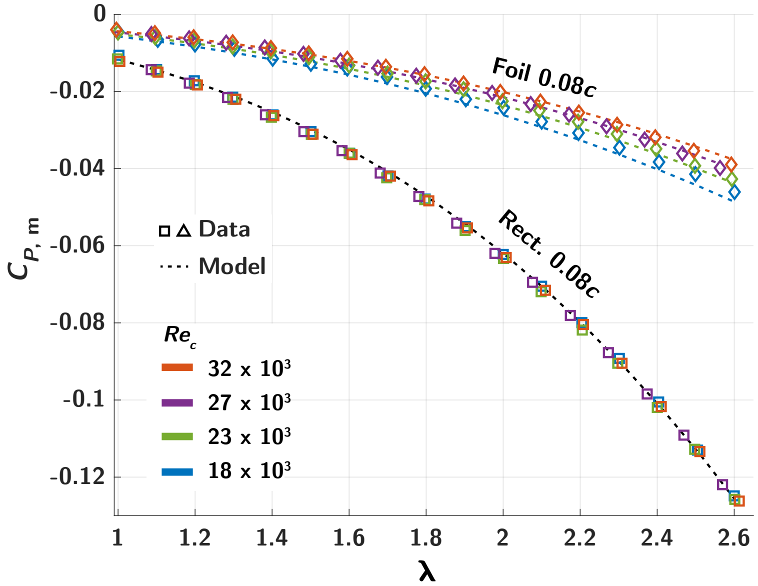

Figure 3.7: Efficiency losses due to drag on the 0.08c struts (symbols) for four different Reynolds numbers as measured by rotating the struts without turbine blades. Losses from the center shaft were measured separately and have been accounted for. The 0.08c rectangle line shows predicted losses according to Eq. (3.9), while the 0.08c foil lines show predicted losses according to Eq. (3.10), with a modification to account for increased drag of the blade mounting pad.

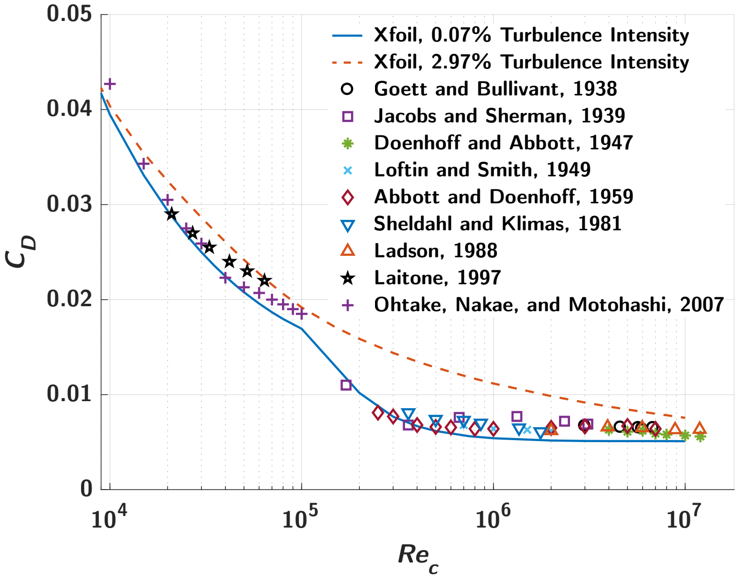

Figure 3.8: Drag coefficient versus Reynolds number for a NACA 0012 foil at zero angle of attack. Experimental data, from [74, 93, 198, 115, 1, 173, 107, 108, 143] is compared to the XFOIL code[55] at two different levels of inflow turbulence intensity. XFOIL is used to generate the drag coefficients in Eq. (3.10). Low Reynolds number drag is shown to be the worst-case scenario, while high Reynolds number drag coefficients asymptote to a constant value.

as the experiments. These values were interpolated based on the local Reynolds number

$$Re_{\text{local}}(r,\theta) = \frac{cU_{\text{rel}}(r,\theta)}{\nu} \tag{3.11}$$

for each blade element and angular position. XFOIL is able to predict drag coefficients for a NACA0012 foil at zero angle of attack within reasonable accuracy, as shown in Fig. 3.8.

Because the flat blade mounting area (see Fig. 3.9) is not a foil in cross section and is exposed while measuring $C_{P,\,\text{m}}$, the drag coefficient for this section of the strut ($r/R > 0.91$) was increased by a constant multiple over the foil drag coefficient such that $C_D(r,\theta) = c_3 C_{D,\,\text{foil}}(r,\theta)$. A constant of $c_3 = 1.68$ was found to best fit the 0.08c foil data. Equation (3.10) was numerically integrated to arrive at the total power loss. Figure 3.7 compares

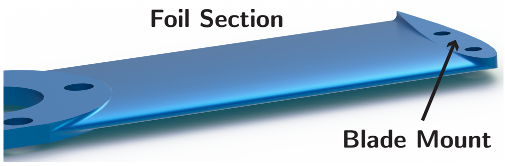

Figure 3.9: A close-up of the $0.08c$ foil strut. The flat blade mount pad adds additional drag when the strut is rotated without blades.

this model to data, where losses due to the center shaft have been removed. The Reynolds number dependence of the foil losses are reflected in the analytical model.

Disks

Von Kármán solved the Navier Stokes Equations exactly for the flow over a rotating disk with a laminar boundary layer[98], with refinements later made by Sparrow and Gregg[181]. A drag torque coefficient for a disk exposed to the fluid on both sides, defined as

$$C_\tau = \frac{2\tau}{\frac{1}{2}\rho\omega^2 R^{*5}} \tag{3.12}$$

was found to be

$$C_\tau = 3.87\ Re_\omega^{-\frac{1}{2}}. \tag{3.13}$$

Here, Re_ω is the disk rotation Reynolds number, given by

$$Re_\omega = \frac{R^{*2}\omega}{\nu}, \tag{3.14}$$

where R^* is the disk radius. For the extended disk mounting structures ($a > 0$), $R^* > R$. Rott and Lewellen[157] extended the approach to include the translation of the disk, equivalent to introducing a parallel freestream velocity, as in the case considered in these experiments. In the limit of a small advance ratio, defined as

$$J = \frac{U_\infty}{\omega R^*}, \tag{3.15}$$

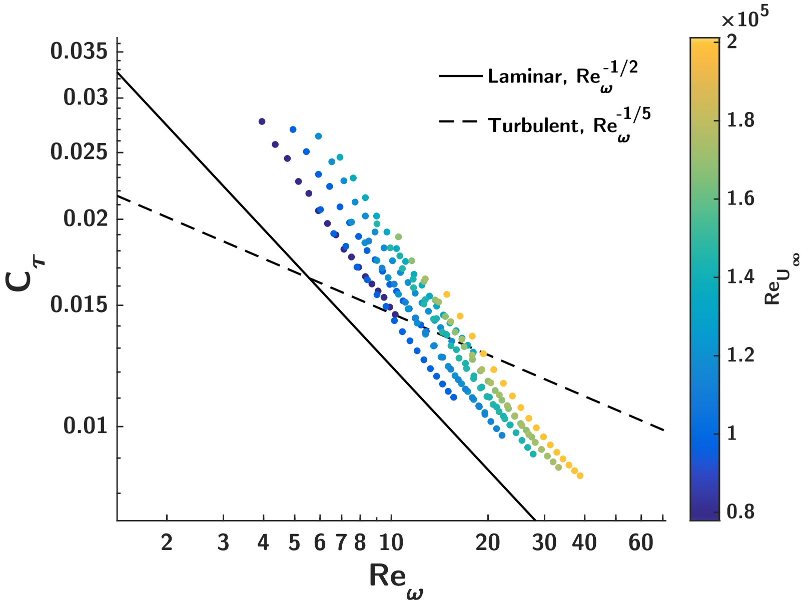

Figure 3.10: Disk rotational drag torque coefficient, Eq. (3.12), data compared to exact solutions for a disk in still fluid with laminar and turbulent boundary layers, Eq. (3.13) and Eq. (3.16)[98].

the solution is identical to Von Kàrmàn's, since the effects on the boundary layer of the freestream flow cancel on advancing and retreating sides of the disk. Von Kàrmàn also considered the case of a turbulent boundary layer on a rotating disk in still fluid, finding

$$C_\tau = 0.146\, Re_\omega^{-\frac{1}{5}}. \tag{3.16}$$

Equations (3.13) and (3.16) have shown good agreement with data for disks rotating in a fluid at rest[167]. To determine if the data collected in these experiments lies within the low advance ratio limit, such that these solutions may be used, disk drag torque coefficients measured in these experiments are compared to the exact laminar and turbulent solutions in Fig. 3.10.

The comparison demonstrates a clear dependence on the freestream velocity, here indicated by the freestream-based Reynolds number,

$$Re_{U_\infty} = \frac{R^* U_\infty}{\nu}, \tag{3.17}$$

suggesting that these measurements are above the low advance ratio limit, and cannot rely on the exact solutions alone. Besides that of Rott and Lewellin, the authors are not aware of any research or analysis on the rotational drag on a disk in parallel flow. Figure 3.10 shows that the drag torque coefficient still approximately follows the $Re_\omega^{-\frac{1}{2}}$ law, suggesting the boundary layer is likely in the laminar regime. The slight upward bend in the data with the highest Re_ω may indicate the onset of transition.

To account for the influence of the freestream velocity on the torque coefficient, a linear advance ratio term is added to the laminar solution, such that

$$C_\tau = 3.87 \; Re_\omega^{-\frac{1}{2}} + pJ, \tag{3.18}$$

where the constant p was found to be 0.0075 through best fit to the data. This empirical correction term was chosen as it results in the analytical solution for the case that the freestream velocity is zero (or as the advance ratio tends towards infinity). The model is compared to data in Fig. 3.11, where the predicted power loss has been normalized by the fluid power incident on the turbine rotor. Further measurements would be required to understand if this model is effective across a broader range of Reynolds numbers.

Dependence on Turbine Parameters

To explore dependence of mounting structure losses on turbine parameters (e.g., number of blades), the models for strut losses are reformulated in terms of non-dimensional turbine operational parameters. To aid comparison, some additional assumptions are made. The first of these is that mounting structures are located only at the ends of the blades. Power loss due to the mounting structures is first normalized by the power in the freestream flow incident on the turbine rotor area as

$$C_{P,\,\mathrm{m}} = \frac{P_{\mathrm{m}}}{\frac{1}{2}\rho U_\infty^3 2RH}. \tag{3.19}$$

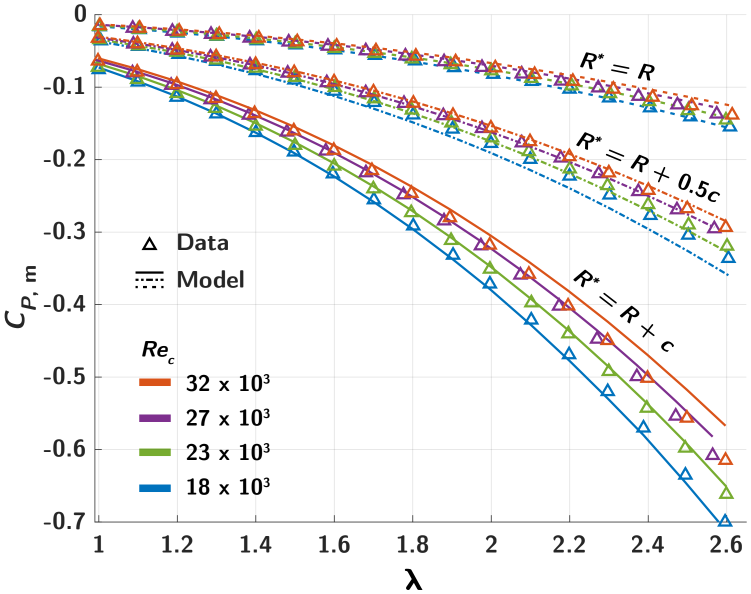

Figure 3.11: Efficiency losses due to drag on rotating disks (symbols) for four different Reynolds numbers as measured by rotating the disk without turbine blades. Losses due to the rotation of the center shaft have been removed. The lines show predicted losses according to the drag torque predicted by Eq. (3.18).

Turbine non-dimensional parameters are then substituted. For the rectangular strut model, assuming the strut width is equal the turbine blade chord, this gives

$$C_{P,\text{ rect.}} = -\frac{\pi t^* C_D \sigma}{4A_r}\lambda(\lambda^2+1) \tag{3.20}$$

Here

$$t^* = \frac{t}{c} \tag{3.21}$$

is the thickness ratio of the rectangular strut sections, and the other parameters are given in Table 3.2 and by Eq. 3.1. For foil struts, if it is assumed that the local Reynolds number is high enough that the drag coefficient is constant, the result is the same as the rectangular strut efficiency loss equation without the thickness ratio (due to the difference in drag coefficient definitions):

$$C_{P,\text{ foil}} = -\frac{\pi C_D \sigma}{4A_r}\lambda(\lambda^2+1). \tag{3.22}$$

Reynolds number independent operation is likely for commercial-scale turbines, so this simplification is appropriate. For the disk efficiency loss, it is assumed that the disk has the same radius as the turbine blades, $R^* = R$, thus the disk advance ratio is equal to inverse of the turbine tip-speed ratio, $J = \frac{1}{\lambda}$. The freestream velocity Reynolds number is a more natural expression for the scale of a turbine, thus the identity

$$Re_\omega = \lambda Re_{U_\infty} \tag{3.23}$$

is applied to Eq. (3.18). The turbine efficiency lost to disk drag torque then becomes

$$C_{P,\text{ disk}} = -\frac{\pi}{4A_r}\lambda^2\left(3.87\sqrt{\frac{\lambda}{Re_{U_\infty}}}+0.0075\right) \tag{3.24}$$

A comparison of Eq.s (3.20), (3.22), and (3.24) shows that for all geometries, increasing the aspect ratio will decrease relative losses, since there is more rotor area per blade mounting structure. A practical upper limit may exist if the blade requires intermediate support for structural stability. For the rectangular and foil struts, losses increase with turbine solidity, while for the disks they do not. However, there is likely a limit to the validity of this dependence on solidity, when the flow induced by a large number of struts has a significant impact on the individual strut drag. The effect of tip-speed ratio is similar across geometries, with the leading term of λ^3 for the foil and rectangular struts and $\lambda^{\frac{5}{2}}$ for the disks. Therefore the choice of mounting geometry (and associated losses) becomes increasingly important at higher tip-speed ratios.

Scaling and Reynolds Number Effects

A natural question whether the results of this study can generalize to larger geometries and, thus, higher Reynolds numbers, such as those of commercial-scale turbines. Though this topic warrants further exploration, some inferences may be made. First, for the foil and disk mounting geometries, the experimental data here represents a worst-case-scenario for normalized losses. As shown by Fig. 3.8, foil drag coefficients are expected to drop further as Reynolds number increases. Similarly, the disk losses show an inverse power law dependence on Reynolds number. In contrast, the drag coefficients of rectangular cross section struts show no change with Reynolds number, so those results would likely translate to larger turbines directly. This is because profile drag, relatively insensitive to Reynolds number for blunt objects, is responsible for the majority of the drag for this mounting geometry.

There is some evidence that these experiments are beginning to approach a regime of Reynolds number insensitivity. Figure 3.12 shows normalized losses, as compared to the highest Reynolds number measured, appear to be asymptotic to a constant value for the thin foil and smallest disk geometries.

Extrapolation of Models

The presented models include terms fit to our specific experimental data. This raises potential concerns over extensions to other turbines and flow conditions. Here, we discuss considerations for extrapolating each model for mounting structure power loss. The model for the rectangular-cross section struts is most likely to remain predictive when applied to

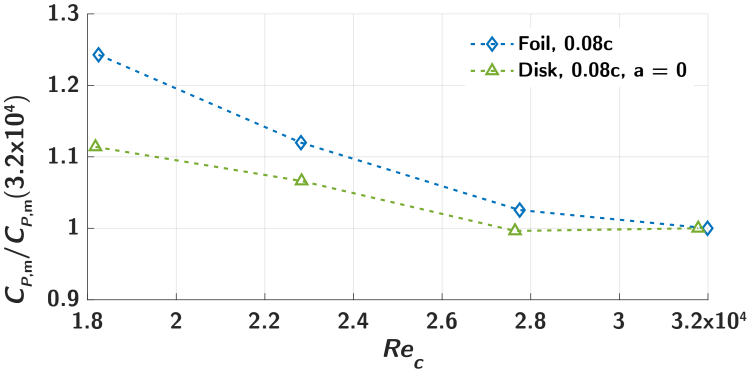

Figure 3.12: Efficiency loss as a function of Reynolds number, normalized by the efficiency loss at $Re_c = 3.2{\times}10^4$, is shown for the thin foil and smallest disk mounting geometries. Since the efficiency loss slope is less negative with increase in Reynolds number, these geometries may be approaching Reynolds number independence.

different scenarios since the fit value of the drag coefficient is close to that reported in previous work and is Reynolds number independent. The fit value in the foil strut model concerns the drag produced by the sharp geometry of the blade mounting pads. In a fully-assembled turbine, this geometry is merged with the blade, likely reducing the drag produced by the mounting pad. Good estimates of foil strut losses in a full turbine are likely possible using only the XFOIL estimated drag coefficients. Larger uncertainty remains for the accuracy of the disk model for higher freestream velocity Reynolds numbers and future work should include verification or modification of this model to ensure applicability across a wide range of turbine sizes and flow conditions.

3.2.4 Conclusions

Ten two-bladed CFT blade mounting geometries have been tested in a recirculating water flume at four Reynolds numbers. The best-performing mounting system consists of thin, foil-shaped struts attached at the ends of the turbine blades. With the exception of the mid-span strut geometry, blade performance is shown to collapse at peak performance when losses due to strut drag are accounted for. Tip-losses are shown to be only partially responsible for the poor performance of the mid-span strut turbine. It is hypothesized that interruption of span-wise flow may cause premature shedding of a beneficial leading edge vortex. Simple models for the drag on rectangular plan-form and disk mounting geometries are explored, and are shown to agree well with experimental data.

We believe these results will be useful to designers of CFTs. As such the main conclusions of this work are presented in terms of end-plate geometry design decisions. First, supports situated at the blade ends appear to improve performance relative to a mid-span support. For blades supported at the mid-span, the addition of winglets or end-plates to blade tips may reduce tip losses, but will increase drag without adding structural support. Additionally, it appears that mid-span supports have detrimental effects in addition to blade tip losses and rotational drag. For this reason, intermediate span supports should be minimized on turbines with a large axial dimension, H, as structural constraints allow, particularly when dynamic stall is an important contributor to turbine power output. Second, for a small number of blades, it appears that streamlined struts rather than disks are optimal. This seems likely to be true for turbines with at least three blades, as multiplying $t = 0.08c$ foil strut drag losses by 1.5 results in less drag than the smallest disk mounting structures tested. If possible, a foil cross-section is optimal, but using a simple-to-manufacture rounded rectangular strut performs nearly as well, as long as the thickness is minimized. For turbines with greater numbers of blades, it is likely that the disk mounting structures will be the optimal mounting geometry, as drag is independent of the number of blades. Since disk drag increases with R^{*4} and we observed no blade performance improvement by extending disks beyond the blades, the disks should not extend beyond the blades. Extension of the rectangular plan-form mounting structures (struts) beyond the blade radius is also likely to be detrimental. Since the suction side of the turbine blade is already shielded, the additional drag will overwhelm any small increase in blade performance due to further shielding of the blade tip.

Additional mounting structure geometries such as foil struts which incorporate small end-plates or winglets and a curved foil-strut interface are under consideration. If possible, strut geometries should be compared at larger scales, in the Reynolds number independent regime. Differences in performance when the inflow is not perpendicular to the axis of rotation should be considered, since the disk and strut geometries will likely respond differently to axial flow. Flow measurements inside the turbine rotor could be used to verify the additional sources of mid-span strut losses identified in this study.

3.3 Preset Pitch Angle

The following contains content from[182][2]

As evidence by Eq. 1.3, the preset pitch angle, or the angle at which the blade is mounted, has a direct influence on the blade-local flow conditions. This work was inspired by this fact, and the relative ease of iterating preset pitch angle experimentally, as well as the lack of a survey of a wide range of angles in prior work. The following section (3.4) details how optimal preset pitch angle can shift with changes in other turbine geometric parameters. This work considers the mechanisms by which preset pitch angle effects turbine performance for a single specific rotor geometry. These results and observations may be extensible only to rotors with similar c/R, N, and blade profile.

3.3.1 Prior Work

Klimas and Worstell (1981) tested preset pitch angles up to 7° experimentally on a vertical axis wind turbine, finding an optimal preset pitch of 2° [104]. Fieldler and Tullis (2009) tested three different preset pitch angles experimentally on a three bladed vertical axis wind turbine. They found a 29% increase in performance for a 7.8° preset pitch angle over the zero preset pitch angle case [68]. Two dimensional numerical simulations by McLaren, Tullis,

---

[2] Portions of this work were published in *The Proceedings of the 10th Annual European Wave and Tidal Energy Conference* and was co-authored with Steven Brunton and Brian Polagye. The author performed the experiments and analysis and wrote the manuscript. Discussion of results has been somewhat modified to reflect increased understanding since the publication of this work.

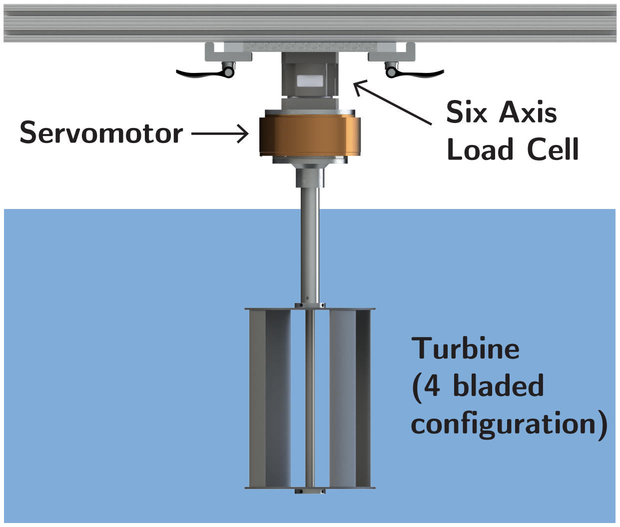

Figure 3.13: The experimental setup for the pitch experiments differed slightly from the standard setup in that the turbine was cantilevered from an AMTI MC3A load cell

and Ziada (2012) of a high solidity turbine illustrate the production of a single large leading edge vortex [124].

3.3.2 Methods

Turbine and Performance Measurement

The turbine rotor used in this work was identical to that given in the methods chapter with the exception of the preset pitch angle. Two sets of circular endplates were used for mounting the blades. Each had sets of mounting holes resulting in different preset pitch angles, ranging from $-4 \rightarrow 14^\circ$ in increments of 2°. Angles between 0° and 12° are presented.

As the first major set of CFT experiments performed by the author, this worked used a slightly less refined version of the experimental setup described in the methods chapter. Instead of being positioned between two load cells, the turbine was mounted at only one end to a face-mount servomotor via a 2.5 cm shaft. The servomotor was mounted in turn to

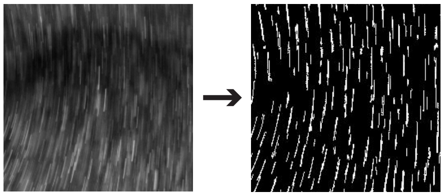

Figure 3.14: A small section of bubble streak-lines from a high-speed video still (left) and after post-processing via localized thresholding and minimum contiguity (right).

an AMTI MC3A six-axis load cell. The servomotor was operated in constant velocity mode isolating fluid forcing on the turbine by eliminating torque due to angular acceleration. The TSR was adjusted by altering turbine angular velocity. TSRs were considered from 0.8 to 2.8 in increments of 0.1. At each TSR, 60 seconds of force and position data was recorded.

Flow Visualization

Two-dimensional flow field visualization was performed for select test cases ($\alpha_p = 0°,\ 6°$, and $12°,\ \lambda = 1.3$ and 1.8). A transparent bottom endplate was used on the bottom of the turbine. Bubbles of approximately 25 μ m in diameter were selectively illuminated with halogen lamps. A high speed camera positioned below the test section captured the motion of the bubbles at 200 frames per second at the mid-plane of the turbine, perpendicular to the axis of rotation. In order to provide streak-lines for a qualitative assessment of velocity magnitude and trajectory, the exposure time was set to 7 ms. This resulted in approximate streak-line length of 4.9 mm for the freestream velocity of 0.7 m/s. The plane of inquiry was kept as thin as possible by increasing the aperture (deceasing the depth of focus) as much as allowable by the exposure time.

Post-processing of video frames was performed by localized thresholding in order to increase bubble visibility in blade shadows, followed by area opening via minimum connectivity (for de-speckling), the result of which is shown in Fig. 3.14.

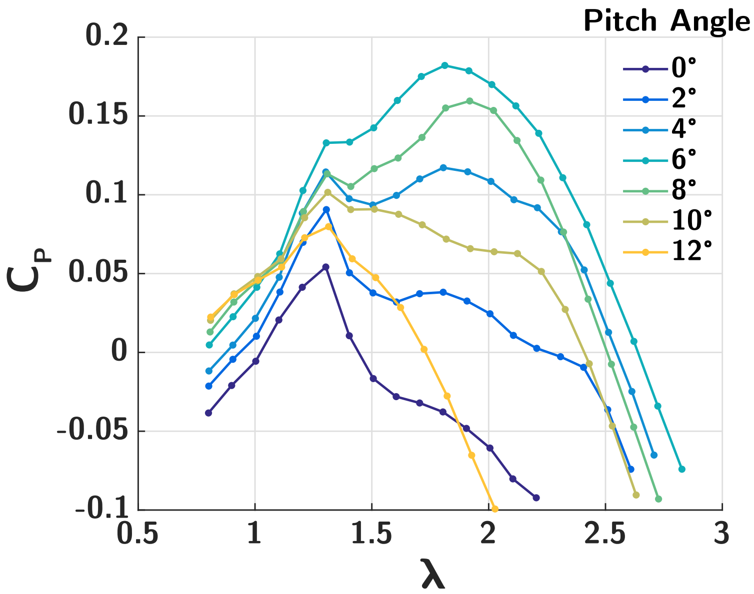

Figure 3.15: Turbine coefficient of performance (C_P, or efficiency) vs TSR for various preset pitch angles for an $N = 2$ bladed turbine.

3.3.3 Results and Discussion

Perfomance Curves

Figures 3.15 and 3.16 show the turbine efficiency versus with TSR for the two-bladed and four-bladed configurations respectively. We find turbine performance to be highly sensitive to preset pitch angle, with an optimum value of 6° for this rotor geometry.. The conversion efficiency increased from 5.4% with zero preset pitch angle to 18.2% at the optimum angle for the two-bladed case and from 8.8% to 14.0% for the four-bladed case.

A general explanation for the beneficial effect of increasing the preset pitch angle can be found by including the effect of the internal wake deficit in the calculation of the nominal angle of attack. The energy extracted from the flow by the blade during the upstream portion of the rotation results in a reduction in the freestream velocity encountered by the blades during the downstream portion of the cycle. This reduces the magnitude of the nominal

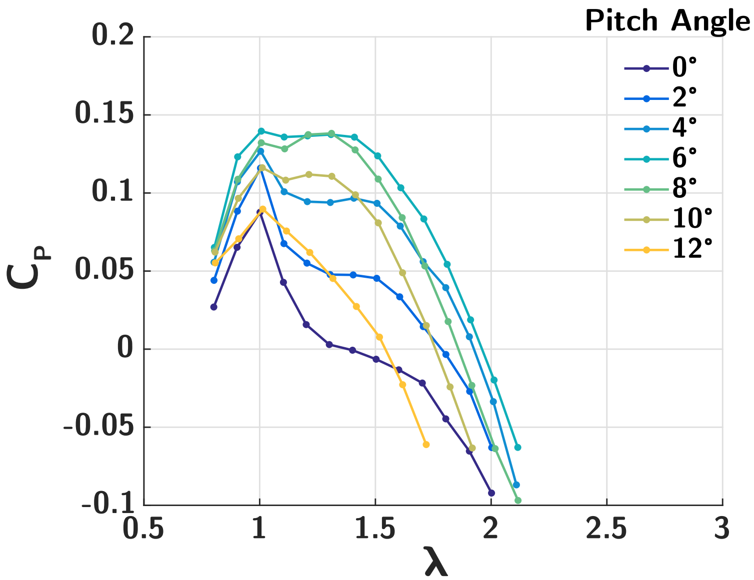

Figure 3.16: Turbine coefficient of performance (C_P, or efficiency) vs TSR for various preset pitch angles for an $N = 4$ bladed turbine.

angle of attack for the downstream portion of the stroke. Increasing the pitch angle has the opposite effect, thus normalizing the maximum nominal angle of attack for the upstream and downstream portions of the stroke (see Fig. 3.17). However, later work by the author (see section 5.1) indicates that little power is extracted on the downstream side of the rotor. This suggests that a larger benefit is due to optimization of the angle of attack on the upstream side, as discussed later on.

Though the maximum efficiency of the four-bladed turbine was significantly less that of the two-bladed turbine, performance was equivalent or better at TSRs less than or equal to one. Previous experiments indicate that a one-bladed turbine performs less well than a two-bladed turbine and with a higher optimal TSR. We hypothesize that the hydrodynamics responsible for an optimal number of blades is due to a balance of three factors. The addition of blades causes: Higher solidity and thus self blockage and flow diversion around the turbine, higher rotational drag per added bladed which reduces the optimal tip-speed ratio which in

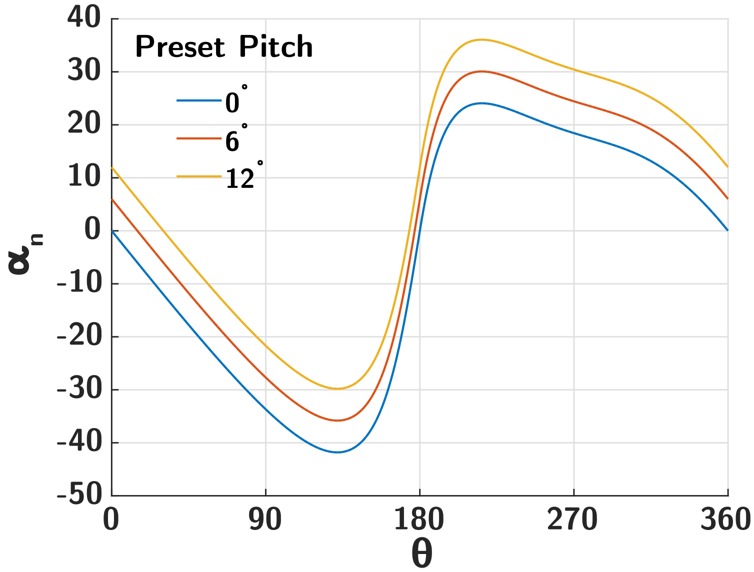

Figure 3.17: The effect of preset pitch angle on nominal angle of attack via Eq. 1.3. For the downstream side of the rotor, this assumes a negative cosine induced velocity in the streamwise direction with a minimum value of $0.5U_\infty$.

turn increases the maximum nominal angle of attack, and an increase in the frequency of fluid forcing and thus power output.

For the remainder of the discussion, we focus on the factors that influence the performance of the two-bladed turbine. We propose that the behavior shown in Fig. 3.15 can be partially explained via two hydrodynamic mechanisms: Lift and drag during the dynamic stall process for the upstream portion of the blade rotation, and the interaction of the foil with the resulting leading edge vortex.

Instantaneous Power Profiles

For a constant angular rotation speed and freestream flow velocity, the instantaneous conversion efficiency is solely a function of the torque due to the blade hydrodynamics ($I\dot{\omega}(t) = 0$ in Eq. 1.7). Figure 3.18 shows the phase-averaged power over half of a turbine rotation (the

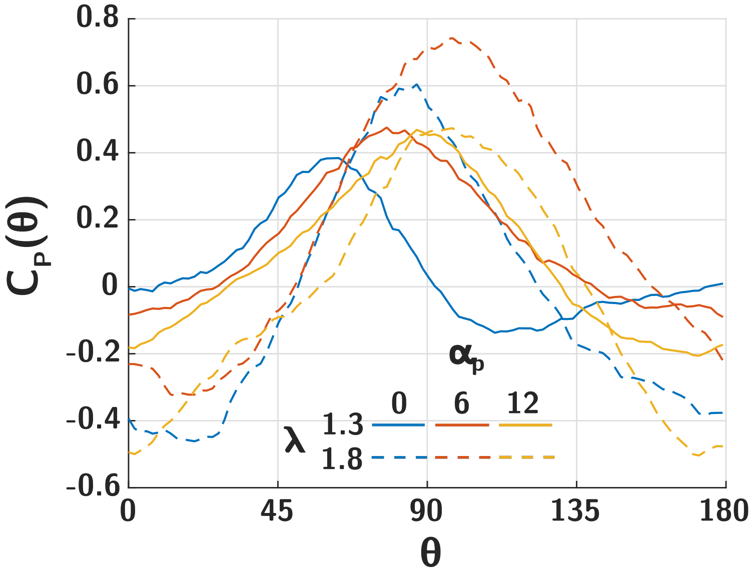

Figure 3.18: Phase-averaged instantaneous efficiency for a two-bladed turbine at various TSRs and preset pitch angles. Only a half rotation is shown as this is the forcing period.

forcing period for a two-bladed turbine) for several TSR and preset pitch angle configurations. With a 60 second sample period and 100 bins per half revolution, we have an average of 600 sample points per bin. Due to the downstream wake deficit, the remainder of this analysis assumes that the positive power output portion of the stroke is dominated by the upstream blade hydrodynamics.

Dynamic Stall

The large range of the nominal angle of attack experienced by the foil throughout the rotation suggests that the foil undergoes dynamic stall [47]. Dynamic stall is characterized by a transient increase in both the lift and drag forces during an increase in angle of attack well above their static values. The flow around the airfoil remains temporarily attached for higher angles than would normally be attached in the static case. The flow eventually separates, often leading to roll-up of the resulting shear layer into a vortex near the leading edge, which is referred to as the leading edge vortex (LEV) [123].

During the dynamic stall process, before and up to separation, the lifting force increases approximately linearly with increasing angle of attack [123]. The increase in the drag force over the static value is delayed and more abrupt than the lift force. As the lift force is beneficial to the power output of the turbine and the drag force is detrimental, at some critical angle of attack (α_{crit}), the benefit from the increase in lift force will be start to be overcome by the negative effect of the now rapidly increasing drag. If we assume that the majority of the power is due to the upstream blade, we can then hypothesize that the peak of the instantaneous power curve occurs at this critical nominal angle of attack. To test this, the peak of each instantaneous power curve is located with respect to the azimuthal blade position. Then Eq. 1.3 is used to calculate the nominal angle of attack at this location. The result is plotted in Fig. 3.19. The predicted critical angle of attack is quite consistent when the virtual pitching rate of the foil $\dot{\alpha}_n$ is rapid, and it is slightly less consistent during slower pitching rates. Surprisingly, no clear dependence on $\dot{\alpha}_n$ is observed, though it is central to many dynamic stall models [47].

Examination of the flow-field via bubble visualization shows that this critical nominal angle of attack corresponds to the onset of full separation. Figure 3.20 shows the flow field at the critical nominal angle of attack (**(a)** and **(c)**) and shortly afterwards (**(b)** and **(d)**) for two preset pitch angles. Though the azimuthal angle at which the critical nominal angle of attack occurs differs for each case (top vs. bottom), we see that for both cases the leading edge vortex occurs shortly after the critical nominal angle, suggesting that α_{crit} indicates the same stage of the dynamic stall process.

Dynamic stall is dictated by the nominal angle of attack trajectory, which in turn is governed by the TSR and preset pitch angle. As such, we observe that dynamic stall is likely responsible for the rightward shift of the instantaneous power curves with increasing preset pitch angle and increasing TSR (Fig. 3.18). This is because both parameters delay or reduce the nominal angle of attack, thus delaying the azimuthal angle at which α_{crit} is reached. The possible exception to these trends in Fig. 3.18 is the $\lambda = 1.8$ and $\alpha_p = 12°$

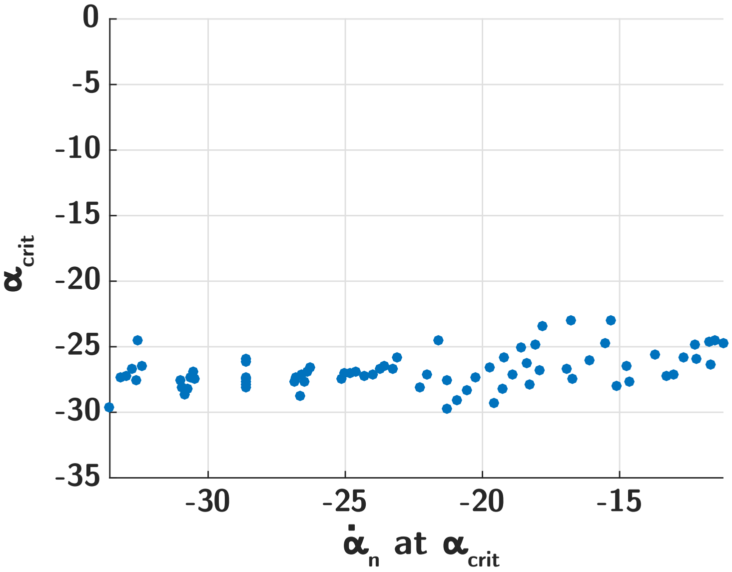

Figure 3.19: Critical angle of attack predictions using the peak of the instantaneous power curves and the nominal angle of attack (Eq. 1.3) for the test cases shown in Fig. 3.15. Cases where the nominal angle of attack never falls below $-25°$ are omitted as it is likely these cases never reach the critical angle.

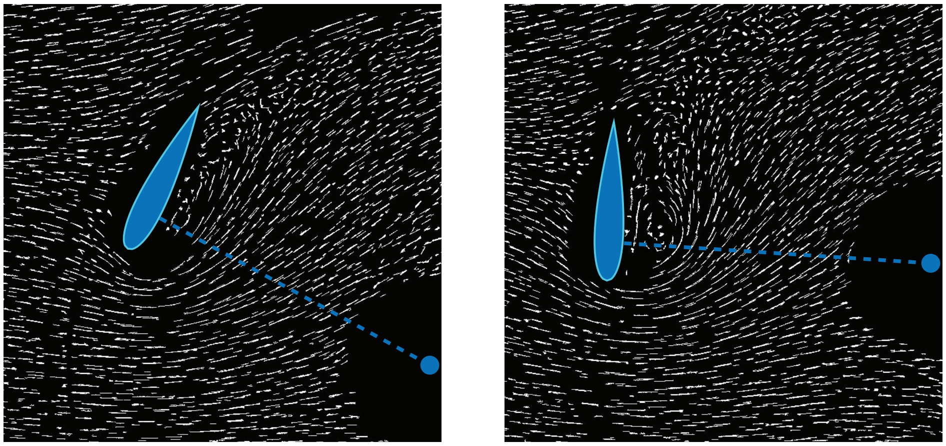

(a) $\lambda = 1.3, \alpha_p = 0°$. $\theta = \theta_{crit}$ $(\alpha_n = \alpha_{crit})$

(b) $\lambda = 1.3, \alpha_p = 0°$. $\theta = \theta_{crit} + \Delta\theta$

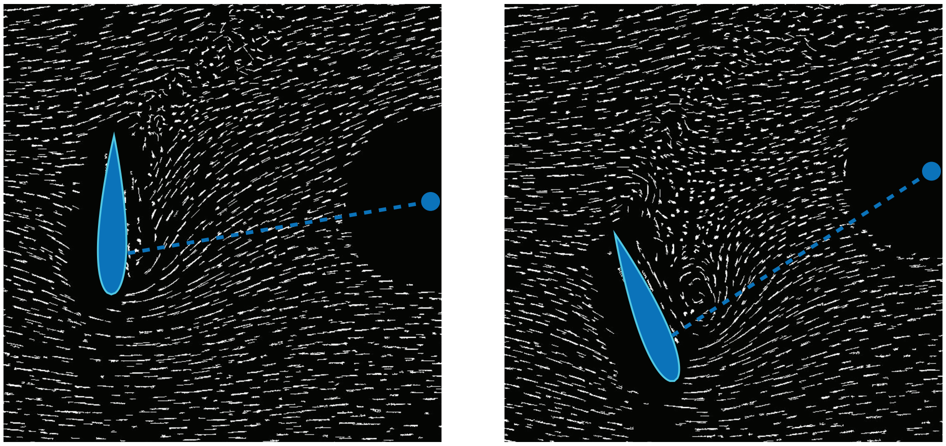

(c) $\lambda = 1.3, \alpha_p = 12°$. $\theta = \theta_{crit}$ $(\alpha_n = \alpha_{crit})$

(d) $\lambda = 1.3, \alpha_p = 12°$. $\theta = \theta_{crit} + \Delta\theta$

Figure 3.20: Flow visualization via high-speed video of entrained bubbles with the blade position superimposed. The freestream flows from left to right. The left images (**(a)** and **(c)**) show the flow-field for the azimuthal position at which the critical nominal angle of attack (α_{crit}) is predicted to occur. The right images (**(b)** and **(d)**) show the same flow-fields 15 ms later ($\approx 17°$ of rotation at this TSR). The top and bottom sets are for $0°$ and $12°$ preset pitch angles respectively. Note that though the azimuthal angle differs between the two cases, the stage of dynamic stall is the similar, supporting the concept of a critical nominal angle of attack.

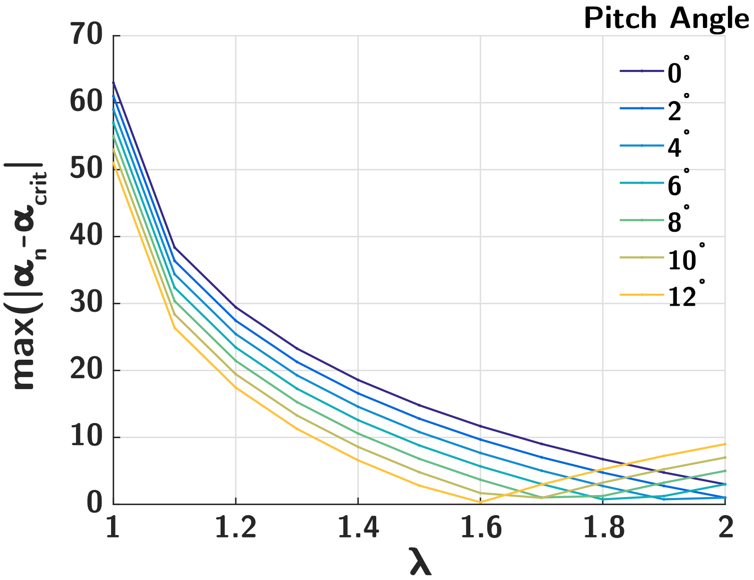

Figure 3.21: The difference between the maximum nominal effective angle of attack magnitude and the predicted critical angle vs TSR at each preset pitch angle tested. We hypothesize that minimizing this value maximizes power production by halting the dynamic stall process where the benefit due to the transient lift force is overcome by the detrimental spike in drag force. Thus the locations where these lines reach zero are reasonable predictors of the locations of peak performance, given in Fig. 3.15.

case. Equation 1.3 predicts that the nominal angle of attack never reaches the critical value for this set of conditions. This observation is reinforced by flow visualization as LEV roll-up is not observed for this case.

We suggest that combinations of TSR and preset pitch angle that result in optimal turbine performance will maximize the lift associated with dynamic stall while minimizing the drag penalty due to total separation. To do so, the nominal angle of attack should reach the critical angle and no further. Figure 3.21 shows the absolute difference of the maximum nominal angle of attack during the rotation and the critical angle. We see that our best performing case ($\lambda = 1.6, \alpha_p = 6°$) minimizes this value, as predicted by our

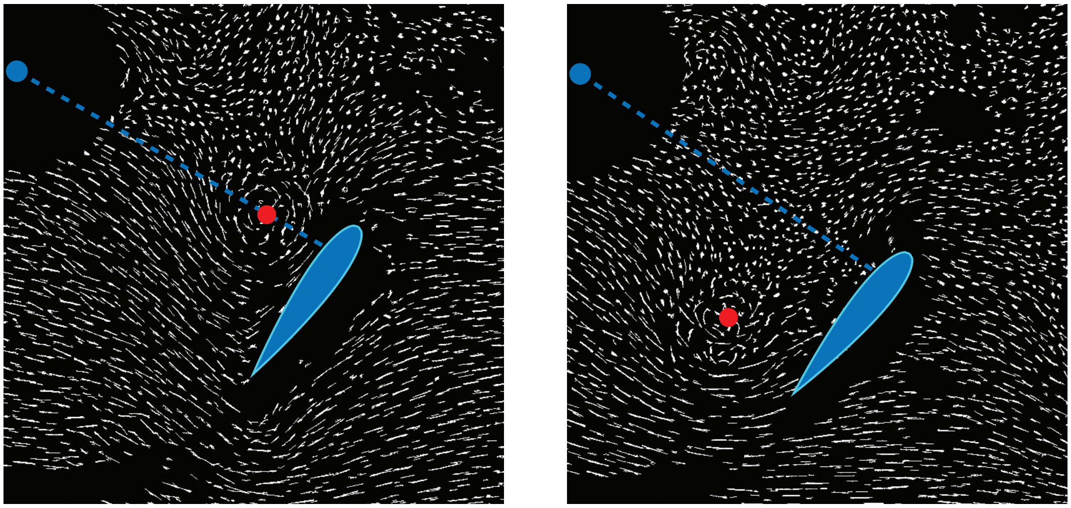

(a) $\lambda = 1.3, \alpha_p = 6°$

(b) $\lambda = 1.8, \alpha_p = 6°$

Figure 3.22: LEV location (highlighted by red dot) well after formation for two TSRs, all other parameters held constant.

hypothesis. In fact, the location of this minimum the predicts second peak (where $\lambda > 1.3$) in the performance curves for each preset pitch angle reasonably well. However, this method predicts good performance for some TSR-α_p combinations (such as $\lambda = 1.6, \alpha_p = 12°$) which perform poorly. In addition, dynamic stall does not explain the peak in the performance curves for all preset pitch angles at $\lambda = 1.3$. This suggests additional criteria help dictate turbine performance.

LEV-Foil Interaction

Flow-field visualizations show that the LEV vortex dynamics are dependent on the TSR. For TSRs of $\lambda > 1.3$, the downstream translation rate of the LEV is slower than the foil translation speed. As a result, the LEV translates towards the trailing edge of the foil, and is finally left behind completely. For TSRs of $\lambda \leq 1.3$, the LEV remains with the foil (at the leading edge). One example of this is shown in the flow visualizations in Fig. 3.22.

Previous studies show that the LEV is a low pressure region which exerts a suction force on the foil [47]. The effect of this is twofold: First, it causes the LEV to have a tendency to be "stuck" to the foil. This is why the LEV translates with the foil even if the foil is moving slightly faster or slower than the surrounding flow ($\lambda > 1$). This could be why the we see an associated critical TSR greater than one. Second, it imparts a hydrodynamic force on the foil, which in turn impacts turbine performance. At $\lambda > 1.3$, this means the eventual location of the LEV near the trailing edge of the foil will result in a detrimental drag force. The influence of the LEV can be seen in the instantaneous efficiency curves in Fig. 3.18. The $\lambda = 1.3$ cases show a higher instantaneous efficiency for the azimuthal angles where the LEV is present (after the peak associated with the power from dynamic stall). The lift benefit from the LEV for these cases is offset by the fact that the opposing blade on the other side of the turbine is translating directly upstream during this portion of the cycle. The $\lambda = 1.8$ cases show a sharp decrease in efficiency during the same region, associated with the drag force, which is at least due to the lack of the lifting force from the well positioned LEV, and possible due to added drag associated with the vortex being located near the trailing edge.

In the high TSR regime ($\lambda > 1.3$), decreasing the preset pitch angle increases the maximum nominal angle of attack, likely increasing the strength of the LEV. This results in a larger drag force once the LEV translates toward the trailing edge of the foil, deceasing overall performance. A large preset pitch angle, though potentially eliminating the LEV altogether due to the small maximum nominal angle of attack, may never reach α_{crit}, thus failing to take full advantage of the dynamic stall as discussed previously.

3.3.4 Other Hydrodynamic Factors

Though dynamic stall and the resulting LEV-foil interaction appear to describe much of turbine performance response with changing TSR and preset pitch angle, several other factors may influence performance significantly. These are outlined below.

As well as altering the nominal angle of attack, the TSR effects the magnitude of the nominal velocity vector experienced by the foil through the turbine rotation. This could explain the poor performance of some of the cases which otherwise undergo an optimal dynamic stall trajectory (those that are minimized in Fig. 3.21). If the TSR is not high enough, the low nominal velocity may result in lower forces or slower roll-up of an LEV, reducing power output. Additionally, the amount of energy extracted from the flow during the upstream portion of the stroke will change the behavior of the downstream interactions. Finally, the foil virtual camber (see Fig. 1.4) may increase lift at moderate levels, though extreme cambers are likely to be detrimental.

3.3.5 Conclusions

We find the energy conversion performance of this CFT to be highly sensitive to the preset blade pitch angle. For a two-bladed turbine, a 23.7% increase in performance was measured between the zero preset pitch angle case and the optimal preset pitch angle of six degrees. The corresponding increase for a four-bladed was 59%.

Two major factors influencing performance are identified: Fluid forcing during pre-separation Dynamic stall and subsequent LEV-foil interaction. A critical nominal angle of attack associated with fluid forcing during dynamic stall is identified using the peak phase-averaged instantaneous efficiency and an expression for the nominal angle of attack. This critical angle is found to be consistent across the parameter space. TSR and preset pitch angle combinations resulting in the highest turbine performance are those for which the maximum nominal angle of attack during the revolution matches the critical value. A secondary peak in the two-bladed turbine performance curve at TSR of $\lambda = 1.3$ is shown to correspond to the point at which LEV translation speed matches the foil translation rate. As a result, the LEV remains near the leading edge, enhancing instantaneous power as the foil translates downstream.

3.4 Reynolds Scaling of Optimal CFT Geometry

The objective of this work is to identify how optimal turbine geometry changes with the turbine scale. Specifically, given a scale of turbine what is the optimal solidity and chord-

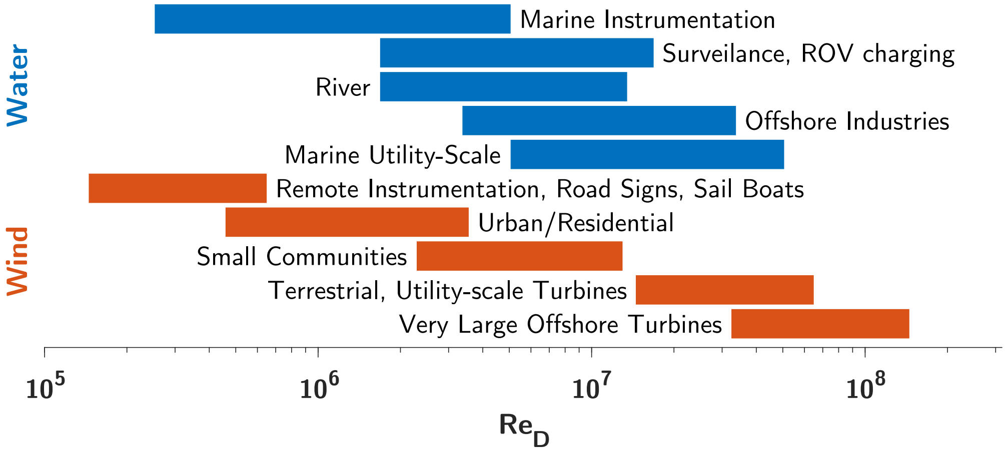

Figure 3.23: Ranges of expected diameter-based Reynolds numbers for cross-flow turbines by application.

to-radius ratio? Put another way, given a turbine radius and freestream velocity, how many blades with what chord-length will be optimal? Simultaneously, this work seeks to illustrate how optimal values of geometric parameters are codependent.

3.4.1 Introduction

It is useful to define the diameter-based Reynolds number, given by

$$Re_D = \frac{DU_\infty}{\nu}, \tag{3.25}$$

as a parameter used to indicate the scale of the turbine in a manner independent of the rotor geometry. Re_D indicates the ratio of the importance of flow inertia versus flow viscosity in the physics of turbine operation. It has been previously shown [14, 129] that CFT mechanical efficiency is highly sensitive to changes in Re_D at low values, while at high values, efficiency is asymtotic as a function of Re_D.

Since, in general, useful power output will be generated by turbines of significant size, it is natural to question the value of optimizing CFTs at low Reynolds numbers. Figure 3.23

demonstrates that if the scope of applications is expanded beyond large, grid-tied turbines, the range of useful values of Re_D spans several orders of magnitude.

From an experimental perspective, turbines that are small enough to test in flumes at low blockage ratios will necessarily have low Reynolds numbers, so it is useful to understand how testing at these scales effects turbine performance and optimal geometry.

Re_c Effects: Boundary Layers

Changes in turbine performance with Reynolds number are primarily driven by the behavior of the foil boundary layer and the resulting changes in lift and drag. The following foil boundary layer information is given in [114]. On the lifting (suction) surface of a foil there is a region of low pressure, generally positioned towards the leading edge. Flow is accelerated as it approaches this low pressure region from the leading edge. The flow is then decelerated as it travels towards the trailing edge, where it approaches the ambient pressure. This region is called the "adverse pressure gradient" area because the pressure gradient is opposite to the direction of flow. If the adverse pressure gradient is too strong, such as at high angles of attack, the flow is slowed to the point where it reverses, and the boundary layer separates from the foil. Instead of smooth flow over the lifting surface, there is now a large region of recirculating flow. This results in a precipitous drop in lift and an increases in drag.

At very low chord-based Reynolds numbers (below about Re_c = 30,000) a foil boundary layer is entirely laminar. Laminar boundary layers are more susceptible to separation than turbulent boundary layers and separate suddenly from near the leading edge. As Reynolds number is increased, a turbulent boundary layer can form after a separated region, termed the separation bubble. The adverse pressure gradient causes separation of the initially laminar boundary layer, but instead of separating completely, the separation bubble causes mixing, resulting in the onset of a turbulent boundary layer. The turbulent boundary layer is much more robust to adverse pressure gradients because momentum is injected into the lower regions of the boundary layer due to mixing. In addition, as angle of attack is increased, separation occurs more gradually on foils with a turbulent boundary, often starting at the trailing edge instead of the leading edge. Foil profile drag is reduced for a foil with a primarily turbulent boundary. In a laminar boundary layer the larger quantity of slow-moving fluid around the foil makes it behave as if it were a thicker body. Mixing between the freestream and a turbulent boundary reduces this effect. Drag due to skin friction is greater in a turbulent boundary layer due faster recovery of the flow velocity, resulting in greater shear at the foil surface.

The net effect is that as chord-based Reynolds number is increased to the transition point (about $Re_c = 70,000$) and above, the foil is able to provide lift at higher angles of attack without separation, and profile drag is reduced. Lift at high angles is important for CFTs due to the widely varying angle of attack experienced during one blade revolution (see Fig. 1.2). Using the separation bubble length as the length scale, the Reynolds number necessary for reattachment is about 50,000 [114]. Therefore foils with a chord-based Reynolds number less than this will likely not experience reattachment of a turbulent boundary layer. This seems at first to exclude our laboratory experiments from this phenomenon until the nominal flow velocity is considered. For our standard turbine geometry at a tip-speed ratio of $\lambda = 2$, the Reynolds number based on the nominal flow velocity, U_n, and the chord length ranges from about 90,000 to 50,000 during the power producing part of the cycle (around $\theta = 45 \to 135°$). Once the chord Reynolds number in CFTs becomes sufficiently high, further increases do not yield significant increase in turbine performance.

Solidity, c/R, and N

As blade chord is increased, turbine solidity (Eq. 3.1) works in opposition to the beneficial effects of increasing Reynolds number. With greater solidity, more flow is diverted around the turbine rotor than through it, resulting in less energy available for extraction and lower performance. Also, as the turbine rotational velocity is increased, the rotor appears more solid to the flow [5]. In addition to increased drag and decreased local angles of attack, this is one of the reasons why turbine efficiency drops at large tip-speed ratios. A turbine with high solidity will need to rotate more slowly to allow the same amount of flow through the rotor as a turbine with low solidity. For this reason, it may be useful to introduce the concept of *dynamic solidity* [5] which incorporates both tip-speed ratio and geometric solidity.

The number of turbine blades must also be considered. Increasing the number of blades without altering the chord length could increase the amount of torque generated by the rotor, except that it also increases the solidity. Adding blades and holding the solidity constant by decreasing the chord length could result in a loss of performance because the lift generated by the blade is proportional to the chord length and the chord-based Reynolds number is decreased.

Prior Work

Previous studies have investigated the effects of Reynolds number on a single geometry by increasing the freestream velocity [193, 155, 90, 27, 12], or in the case of [129] the freestream density. Additionally, several studies separately examined the effect of solidity [174, 152, 140, 122, 104, 68, 46]. Tanino et al. [190] examined optimal solidity and preset pitch angle as functions of turbine scale for three and five-bladed cross-flow wind turbines. Chord-based Reynolds numbers of $1.5 \to 4.6 \times 10^4$ were tested. Because the turbine efficiency for all but the largest Reynolds number was less than $C_P = 0.03$, it is likely that these turbine were operating in a drag-based mode, so these results will have limited utility for informing lift-based CFT design.

Scope of Work

As there is a gap in studies comparing the performance of a turbine within and well out of the transitional chord-based Reynolds number regime, a thorough optimization of the blade count, cord-to-radius ratio, and preset pitch angle has been performed. Optimization was performed at Re_D of 173,000, 255,000, and 805,000. It is intended that prior to publication of this work, data at Re_D of about $80,000$ can be included. The total parameter space explored is given in Table 3.4.

c/R	N	α_p	Re_D
0.236	2	2, 4, 6, 8	b, c, d (d only @ $\alpha_p = 2$)
0.236	4	2, 4, 6, 8	b, c, d (d only @ $\alpha_p = 8$)
0.354	2	4, 6, 8	b, c, d
0.354	4	4, 6, 8	b, c, d
0.472	2	4, 6, 8, 10	b, c, d (no d @ $\alpha_p = 10$)
0.472	4	4, 6, 8, 10	b, c, d (no d @ $\alpha_p = 10$)
0.590	2	6, 8, 10	b, c
0.590	4	8, 10, 12	b, c
0.708	2	8, 10, 12	b, c
0.708	4	8, 10, 12	b, c

Table 3.4: Turbine geometry and Reynolds number test matrix. The turbine blade profile was NACA0018. $Re_D(b) = 173{,}000$, $Re_D(c) = 255{,}000$, $Re_D(d) = 805{,}000$. Future work will include collection of data at $Re_D(a) = 80,000$, and the fill-in of the missing data-point at $c/R = 0.590$, $N = 4$, $\alpha_p = 10$ for $Re_D(b)$ and $Re_D(c)$.

3.4.2 Methods

Data at $Re_D(b) = 173{,}000$, $Re_D(c) = 255{,}000$ was collected in the UW Tyler flume using equipment and techniques as described in the methods chapter. Notably, the temperature of the flume was held at 34.7° C for the highest possible upper value of Reynolds number in this facility.

Data at $Re_D(d) = 805{,}000$ was collected at the University of New Hampshire Chase Ocean Engineering Laboratory in a tow tank. The test section of this tank measure 2.44 m wide, 3.66 m deep, 36.6 m long. A turbine rotor and blades, identical in non-dimensional parameters, blade mounting strategy, and blade profile to the model used in the UW Tyler flume was constructed. This larger turbine had an area of 1.0 m^2. The blockage ratios of the lab-scale turbine in the UW Tyler flume and of the 1 m-scale turbine in the UNH tow tank were both 11%. For this reason, blockage corrections are not performed as results analyses are comparative.

The UNH tow tank turbine test carriage and data aquisition system were constructed by Pete Bachant, and complete details of this system can be found in his thesis[11]. Importantly, this system allowed for operation of the turbine under constant velocity control and measurement of turbine performance and thrust.

As in section 3.2, end-plate losses are subtracted from total values, giving a proxy for the blade-only performance and thrust. The objective of this study is the effect of Reynolds number on blade performance. Subtracting the effects of the end plates disks removed any convolved Reynolds dependence of these structures from the results.

3.4.3 Results and Discussion

The vast quantity of data collected in this campaign is illustrated by Fig. 3.24. In all, 82 performance curves were collected. In the following analysis, only the peak performance for each $C_{P,b}$-TSR curve is examined. Due to the multi-dimensionality of the parameter space, it is useful to isolate the effects of single parameters as much as possible, and we start with

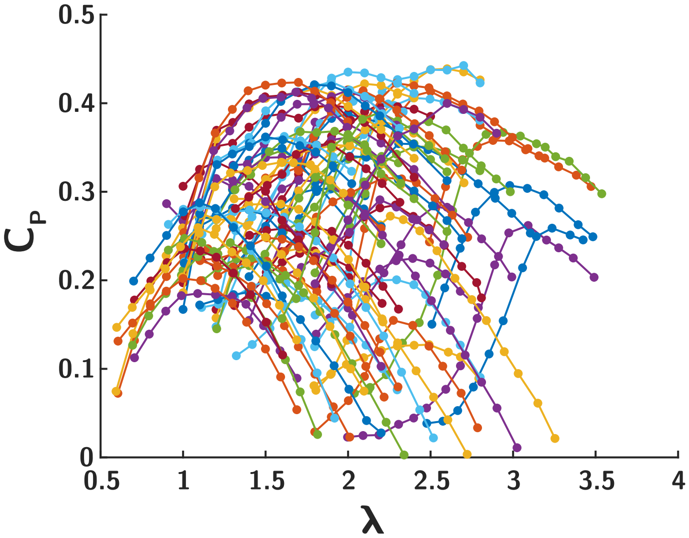

Figure 3.24: All performance curves collected for the purpose of the scaling investigation. This is not intended to illustrate trends, but rather the volume of data collected.

the preset pitch angle.

Optimal Preset Pitch Angle

First, we consider the optimal preset pitch angle (α_p) found for each combination of c/R, N, and Re_D. During data collection, as many curves as necessary were collected to ensure that the peak performance as a function of α_p was captured for each c/R and N. We find that optimal α_p increases fairly linearly with increases in c/R. Additionally it appears that optimal α_p increases with Re_D. As far as the author is aware, this is the first publication of these dependencies, shown in Fig. 3.25.

A more usual way to describe CFT geometry is to combine N and c/R into a single value of solidity (σ, Eq. 3.1). However, this work demonstrates that solidity is an extremely poor parameter for describing the effect of geometry on rotor performance. Again considering the optimal preset pitch angle, but this time as a function of solidity, we see no clear trend emerge (Fig. 3.26, **(a)**). This is because, as illustrated in Fig. 3.26, **(b)**, inversely varying N

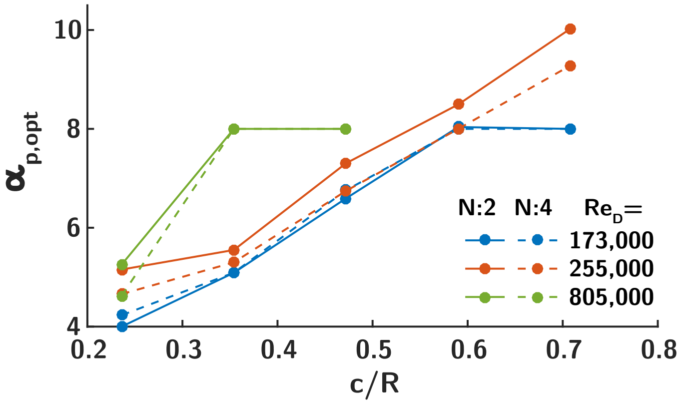

Figure 3.25: Optimal preset pitch angle versus chord-to-radius ratio for two and four-bladed rotors.

and c/R can result in turbines with the same solidity, but with different preset pitch angles.

For larger values of c/R it is beneficial to operate the turbine at a lower TSR (see Fig. 3.27). This is likely a combination of two aspects. The larger solidity turbines slow down the flow more as it approaches the rotor, so to achieve the same local angle of attack, the ωR vector in Fig. 1.3 needs to be shortened (by spinning slower). Second, the larger the c/R, the larger the virtual camber. Large virtual camber likely generates significant drag, penalizing high rotation rates. However, operation at lower TSR will increase the range of angles-of-attack experienced by the foil. Increasing the preset pitch angle has the effect of decreasing the maximum angle of attack on the upstream (power generating) portion of the stroke, as demonstrated in section 3.3. This is the likely mechanism for the increase in optimal α_n with increased c/R. Further investigation is necessary to determine why optimal preset pitch weakly increases with Reynolds number.

Optimal c/R

Figure 3.28 shows, for optimized α_p, the optimal c/R as a function of Re_D for two- and four-bladed turbines. Generally speaking, optimal c/R decreases with Re_D. Though this

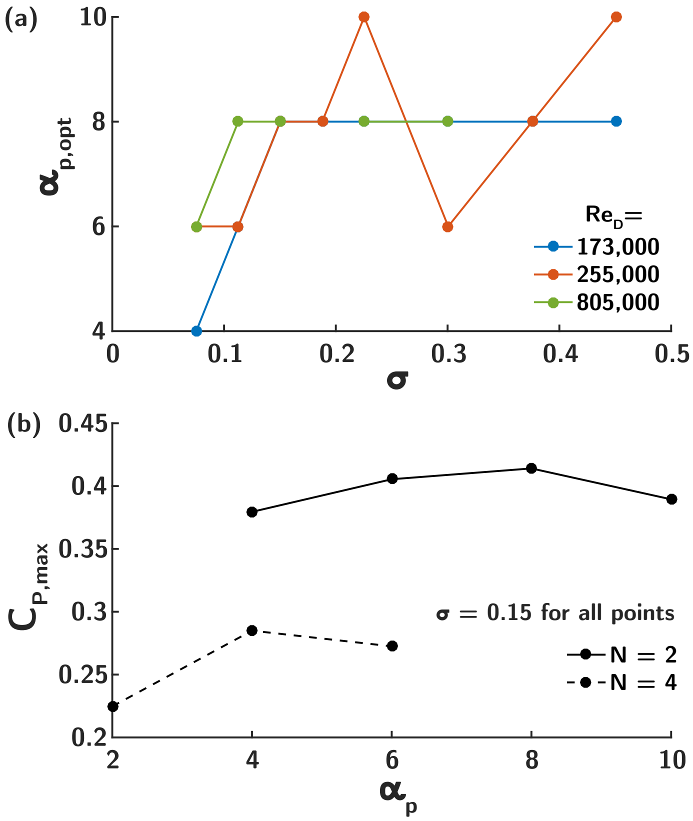

Figure 3.26: **(a)** Optimal preset pitch angle versus solidity and **(b)** peak performance versus preset-pitch angle for two rotors with the same solidity but differing numbers of blades. Solidity is shown to be an inappropriate choice of non-dimensional parameter for analyzing the effect of geometric changes on performance.

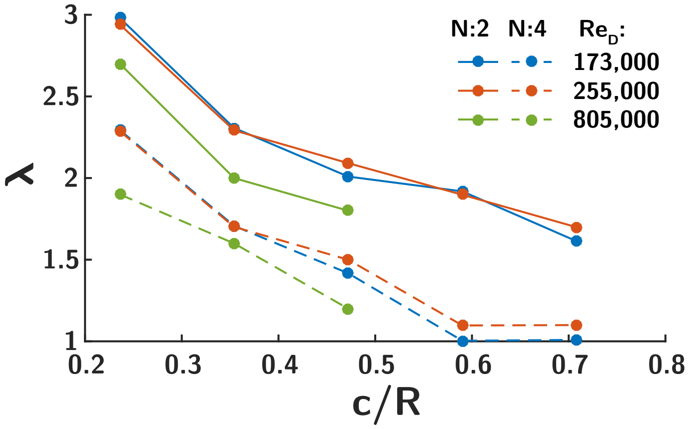

Figure 3.27: TSR of peak performance for optimized preset pitch angle as a function of c/R.

trend may be teased out though the comparison of many separate studies, this is the first time this is shown in a single experiment with all other parameters controlled. Given the previous discussion on the effects of Reynolds number and c/R and thus solidity, we propose the following explanation. At small turbine scales or low freestream velocities, where the chord-based Reynolds number is in the transitional regime, an optimal turbine geometry will consist of few blades with large chord in order to maximize the local chord Reynolds number. The resulting higher solidity will result in a lower optimal tip-speed ratio to maintain an optimal dynamic solidity. Optimal turbine geometries for larger Reynolds numbers, above the transitional chord-based Reynolds number can get away with smaller chord-to-radius ratios, thus lower solidities and higher optimal TSRs. For larger turbines, the smaller total forces applied to relatively smaller chord lengths is made up for by the higher number of blade passes per unit time.

Figure 3.28 gives a false impression that this work has fully captured the trends in the effect of c/R on performance. Figure 3.29 shows peak performance at the optimal preset-pitch angle for the Reynolds numbers and blade counts tested. Examining the lower plot, **(b)**, where each line is normalized by its maximum value, it appears that this study did not fully capture the optimal c/R , especially for the lowest and highest Reynolds numbers. At

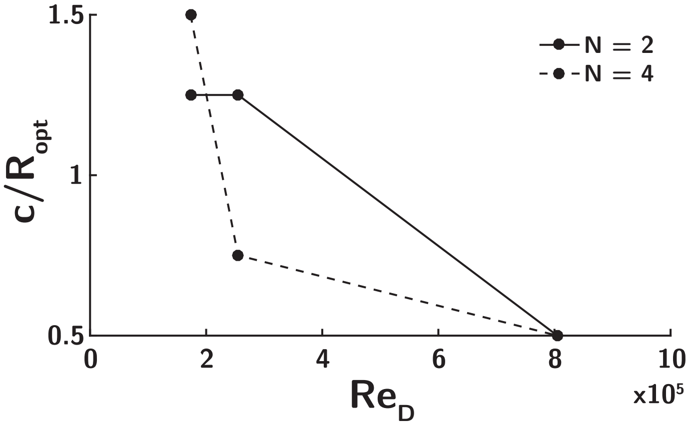

Figure 3.28: Optimized chord-to-radius ratio (with preset pitch angles optimized) as a function of diameter-based Reynolds number.

the lowest Re_D, it appears as if further increasing c/R may continue to increase performance, particularly for the 2-bladed rotor. This is remarkable, given that the $c/R = 0.708$ is likely the highest c/R turbine to be published. At the highest Re_D, further decreases in c/R may continue to improve performance for both $N = 2$ and $N = 4$ turbines. However, at some point, structural concerns will limit the minimum viable c/R.

Given the inter-dependencies above, we hypothesize the following. At small turbine scales or low freestream velocities, where the chord-based Reynolds number is in the transitional regime, an optimal turbine geometry will consist of few blades with large chord and a moderately high solidity. This will result in a lower optimal tip-speed ratio to maintain an optimal dynamic solidity. Because dynamic stall is more significant at lower tip-speeds, optimizing preset pitch is important for maximizing power. Optimal turbine geometries for large scales, well above the transitional chord-based Reynolds number, will have more blades, a smaller relative chord-length, and a lower solidity. Here, conversely, only a small preset pitch is optimal.

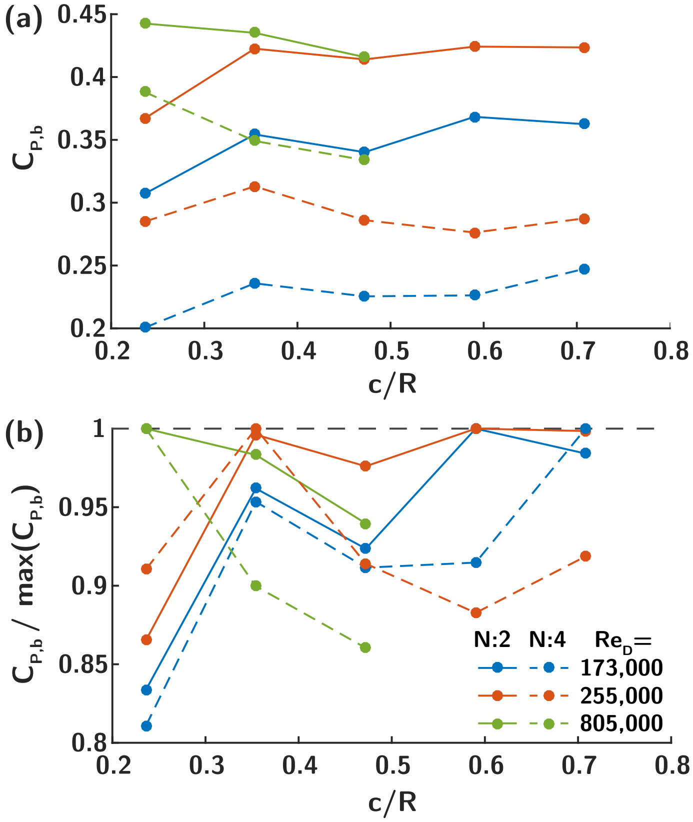

Figure 3.29: **(a)** Peak blade performance Eq. 3.4 versus chord-to-radius ratio. **(b)**, the same, but performance is normalized by the maximum C_P for that N, Re_D combination. This demonstrates that this experiment did not test low enough values of c/R at the highest Reynolds numbers, nor high enough values of c/R at the lowest Reynolds numbers.

3.4.4 Conclusions

This work shows for the first time that optimal preset pitch angle increases with c/R, and to a lesser degree, Re_D. Solidity is shown to be a poor parameter for analyzing optimal rotor geometry due to the competing effects of N and c/R. For the first time in a single study, optimal c/R is shown to vary inversely with Re_D. Further work on rotor geometries with higher and lower c/R should be tested to fill in the details of this trend. Significantly, this work shows that good-performing CFTs can be design for low Reynolds number operation, with a peak blade performance at $Re_D = 173{,}000$ of $C_{P,b} = 0.37$. Further analysis of this dataset into the trends of performance curve shape could be useful for designing turbines with particular power output and control characteristics.

Chapter 4

WAKE ANALYSIS

4.1 Introduction

The average rotor performance in a densely-packed array has been shown to be 20% higher than the performance of a single isolated turbine [32]. Similarly, the authors have demonstrated a 30% increase in average rotor output in an array of two CFTs compared to isolated turbine performance [187]. The remarkable performance of densely packed CFTs stems from several phenomena. First, the orientation of the rotation axis results in an acceleration of the bypass flow, especially on the side of the rotor where the blades are retreating (traveling downstream). Neighboring rotors placed in this flow experience an increased incoming flow velocity. Second, the tip vorticies shed from CFTs blades have an axis of rotation that lies in a plane parallel to the ground. These vortices induce vertical mixing, increasing the transfer of momentum from the high-speed flow above the array to the rotor level, increasing the streamwise wake recovery rate [12]. Finally, we speculate that performance may be enhanced through the interaction between periodic coherent structures shed by an upstream turbine and the blades of a downstream turbine. This hypothesis is inspired schooling fish who have been shown to benefit from well-time interactions with vortices shed from upstream individuals [118]. These potential performance increase mechanisms motivate the study of the mean, periodic, and time-resolved components of a CFT wake, with a special focus on periodic coherent structures that may be harnessed by nearby turbines in an array.

Measurement and analysis of cross-flow and vertical-axis turbine wakes have been been conducted for decades, starting with [137]. Point measurements using Pitot tubes [137, 20] hot wire [20, 23, 146, 147], and laser [38] and acoustic [12, 101, 102] and Doppler velocimetry have been used to describe the mean wake structure, spectra, and time-average turbulence statistics. Two- [6, 5, 58, 149] and three-component [86, 156, 192] planar particle image velocimetry (PIV) and magnetic resonance velocimetry [159] measurements as well as simulations [29, 141, 164, 163, 171] have been used to investigate the wake spatial variability, including wake geometry and recovery rate and the roles of turbulence. Despite the widely varying rotor configurations and operating conditions of these studies, a set of features common to CFT wakes have emerged. The most common measurement location has been the mid-plane of the rotor (perpendicular to the rotation axis). In this plane, all studies report some asymmetry or angular deflection of the wake in the direction of turbine rotation, with a more intense shear layer on side where the blades are transiting upstream (the advancing side). Flow structures shed at the blade pass frequency have been identified in nearly all studies on the retreating side of the wake (for example [31, 12, 20, 159]) and on both the retreating and advancing sides by a few [149, 5, 29, 86]. [5] determined that the flow oscillations transition to those corresponding to a bluff body in the far wake. Areas of high turbulence intensity have been identified in a streak on the advancing side of the wake deficit [12] and on both sides [86, 156]. Studies that examined the 3D wake structure have identified the primary mechanism for wake recovery as axial (vertical) flow induced by vortices shed from the blade tips [101, 102, 29] or the induced cross-stream (horizontal) flow [12]. In contrast, the wake recovery in axial-flow turbines is driven primarily by turbulent mixing upon the breakdown of the helical tip vortices [113, 29]. Wake recovery rates have been documented to be significantly faster than those of axial-flow turbines [29, 48]. In addition to wake measurements, multiple studies have performed measurements within the rotor, demonstrating the importance of dynamic stall and subsequent blade-vortex interactions in normal CFT operation [31, 71, 66, 60, 58].

The objectives of this work are three-fold. Time-resolved, three-component, planar PIV measurements are used to compare the mean wake structure of an unusually high chord-to-radius ratio turbine to prior work considering more typical rotor geometries. Because the performance of small CFTs generally increases with Reynolds number [14, 129] a rotor designed for small-scale applications can benefit from maximizing the chord-length, thus maximizing the blade-chord based Reynolds number. Additionally, structural constraints may encourage the use of high chord-to-radius ratio rotors. The second objective is to demonstrate how an algorithm incorporating the dynamic mode decomposition (DMD) can be used to perform a triple decomposition that identifies energetically important modes that may remain obsured using other methods. The algorithm is extended to apply to measurements made separately over multiple regions, and is brought to bear on the turbine wake. The final objective is to use modern tools to analyze the coherent structures shed into the near-wake of the turbine. The geometry and trajectory of these structures and their impact on the mean flow has not been described in-depth in prior work.

4.1.1 CFT Operation

At large turbine scales, such as those used for commercial power production, rotor geometries with few, relatively small chord-length blades exhibit high maximum efficiency. For example, the Sandia 34 m test bed turbine, with a peak C_P of approximately 0.41 exhibited this geometry [8]. However, as discussed in section 3.4, because CFT performance can increase rapidly with Reynolds number [14, 129], at smaller scales it can be useful to increase the chord-length of the turbine to maximize the blade Reynolds number. Larger chord-length foils may also be more structurally robust, important because blade fatigue is often the cause of CFT structural failure [132]. Finally, large chord-to-radius turbines have a reduced the tip-speed ratio at peak performance, reducing losses from rotating blades supporting structures. These factors motivate the study of an unusually high chord-to-radius turbine. The low tip-speed ratio at peak efficiency of this geometry results in large local angle-of-attack variations (Fig. 1.2), all but guaranteeing separation and stall behavior during normal operation.

4.1.2 The Triple Decomposition and Dynamic Mode Decomposition

Flows with natural or forced periodicity, such as the wake of a CFT, contain fluctuations that are regular in space or time, and thus cannot be characterized as turbulence. It is then useful to analyze flows with periodic, organized content in terms of the triple decomposition

[92], given by

$$\boldsymbol{U}(\boldsymbol{x},t)=\overline{\boldsymbol{u}}(\boldsymbol{x})+\widetilde{\boldsymbol{u}}(\boldsymbol{x},\phi(t))+\boldsymbol{u}'(\boldsymbol{x},t). \tag{4.1}$$

The total flow, $\boldsymbol{U}$, is given by sum of time-averaged flow, $\overline{\boldsymbol{u}}$, the periodic flow, $\widetilde{\boldsymbol{u}}$, and turbulent motion, $\boldsymbol{u}'$. Here $\phi(t)$ is the phase of oscillation of the periodic component. While $\overline{\boldsymbol{u}}$ is trivial to calculate, there are multiple approaches for separating the remaining periodic and random fluctuations. For flows where the forcing mechanism or flow periodicity are measured simultaneously with the velocity field, $\widetilde{\boldsymbol{u}}$ can be calculated using by a phase-average, or the ensemble mean of measurements occurring at the same phase of the forcing oscillator. This was the approach taken by the pioneers of the triple decomposition [92], and is commonly employed, for example in the wake of an axial-flow wind turbine by [62]. Drawbacks to this approach include the necessity of measuring the phase of the forcing oscillator, as well as the introduction of statistical uncertainty in the case that measurements are not locked to the forcing oscillator [39]. A potential solution is to use a weighted average, where measurements are weighted based on their phase offset from the phase in question. Fourier averaging, where $\widetilde{\boldsymbol{u}}$ is estimated using a truncated Fourier series [178], eliminates the need to measure the forcing signal simultaneously with flow measurements and removes error associated with phase uncertainty. However, since the base forcing frequency must be known or assumed, periodic flow structures due to phenomena other than the primary forcing mechanism may not be included in $\widetilde{\boldsymbol{u}}$.

The desire to automatically extract and rank the importance of spatially coherent and temporally periodic flow phenomena of multiple scales without a priori knowledge of the frequencies of interest has inspired a number of methods. Instead of an oscillatory component composed of a single base frequency, these methods yield a triple decomposition of the form

$$\boldsymbol{U}(\boldsymbol{x},t)=\overline{\boldsymbol{u}}(\boldsymbol{x})+\sum_{n=1}^{R}\widetilde{\boldsymbol{u}}_n(\boldsymbol{x},\phi_n(t))+\boldsymbol{u}'(\boldsymbol{x},t), \tag{4.2}$$

where R is the number of oscillatory modes used in the reconstruction.

Proper orthogonal decomposition (POD) is a widely used technique for oscillating mode extraction [59, 142], including in the wake of an axial-flow turbines [150, 113]. POD extracts spatially coherent modes and ranks them by energy content. For further details on POD, there are a number of excellent references [24, 88, 189]. Determination of the POD basis does not consider the system dynamics. A single POD mode can then contain a spectrum of frequencies, and thus does not guarantee temporal coherence of the identified structure. This is illustrated by the fact that the snapshot POD [176, 10, 33] mode shapes do not depend on the order of the flow data time-series. Many instances of the failure of POD to extract dynamically important modes for multi-scale systems have been documented [162, 16, 189].

A related, alternative method is the dynamic mode decomposition (DMD) [168, 195, 106]. DMD can be thought of as a combination of the spatial rank reduction of POD and combined with Fourier analysis in time. DMD has recently been connected to spectral POD [194], used to analyze a CFT wake by [5], and the resolvent operator [172]. Another view is that DMD is an approximation of the Koopman operator, which is an infinite-dimensional linear operator that steps a system forward in time by operating on an infinite-dimensional Hilbert space of all scalar-valued functions of system measurements [158, 126]. This approximation results in a set of modes that are coherent in space and have distinct oscillation frequencies and growth or decay rates. The original DMD algorithm of [168] has shown to be suboptimal on noisy data, and there are several recent approaches to de-bias the DMD algorithm for noisy data [53, 84, 9]. The optimized DMD (optDMD) algorithm of [9] provides an efficient way of solving a nonlinear least-squares regression problem using variable projection, which allows for an optimal DMD fit from data that is unevenly spaced in time. The optimized DMD method also provides a mechanism for constraining the eigenvalues of the returned modes, for example to keep them on the unit circle. This allows for solving of periodic-only optDMD modes, and can be used to restrict the oscillation frequencies. The data taken in these experiments consists of overlapping fields-of-view taken at separate times. When optDMD is performed on the entire dataset, the resulting modal oscillations are out-of-phase. The field-of-view overlap regions are used to correct the phase misalignment, resulting in full-field DMD modes. This method is likely useful for modal analysis in any experiment utilizing multiple overlapping measurement areas.

In this work we compare the efficacy of a number of triple decomposition methods, including the new method using the optDMD algorithm. Oscillatory structures that are not evident from phase-averaged or Fourier-based triple-decomposition techniques are revealed, and performance based on error and energy capture is compared.

4.1.3 Coherent Structure Analysis

In an effort to provide a detailed description of the dynamics of coherent structures in the non-turbulent component of the wake ($\overline{\boldsymbol{u}}+\widetilde{\boldsymbol{u}}$), the Finite-Time Lyapunov exponent (FTLE) fields [82, 170, 79, 64] and Lagrangian Coherent Structure (LCS) ridges, defined here using ridges of of the FTLE field are examined. FTLE detects coherent structures via their boundaries by computing the maximum strain rate of a Lagrangian packet of fluid over a finite time period. Integration backward and forward and time yields attracting and repelling FTLE ridges, which enclose coherent structures. Unlike Eulerian methods, such as the Q-Criterion [91], the FTLE field does not require a user-defined, subjective threshold. Additionally, as an integration-based method, FTLE analysis is much more robust to noise than derivative-based methods [79]. Though other methods have been shown to identify coherent structures more rigorously [83], the ridges of the FTLE field remain practically useful due to their ease of computation, mathematical simplicity, and conceptual accesibility. Structures associated with shear-layer roll-up, blade-vortex shedding, and bluff-body wake oscillation are identified. The role of these structures in wake mixing and recovery is examined. Finally, vortex-core tracking is performed on the full time-resolved wake to determine vortex longevity and trajectory repeatability. The focus of discussion is on potential impact on downstream turbines.

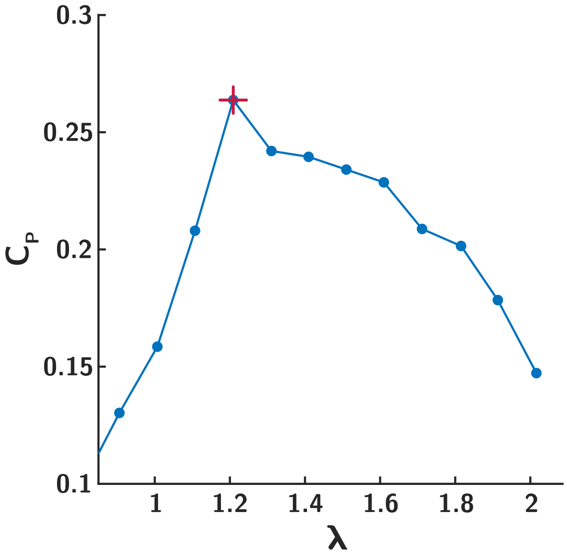

Figure 4.1: Performance curve (mechanical efficiency versus tip-speed ratio) for the experimental turbine. Red cross indicates operating point during wake data collection.

4.2 Experimental Setup

4.2.1 Flume and Turbine

Experiments were performed in the University of Washington Tyler Flume. The diameter-based Reynolds number,

$$Re_D = \frac{DU_\infty}{\nu}, \tag{4.3}$$

was 1.1×10^5, where ν is the water kinematic viscosity. The turbine was the same as that described in the methods chapter, except that the chord length was greater, 0.061 m, giving a chord-to-radius ratio of 0.71. The turbine was operated under constant angular velocity control at its peak performance point of $C_P = 0.26$ at a tip-speed ratio of $\lambda = 1.2$. The turbine performance curve is given in Fig. 4.1.

The turbine operated using the standard setup, but without load cells. In this configuration, the rotor was cantilevered from the face of the servomotor. This turbine acquisition was synced with the PIV measurement system. The turbine rotor and servomotor were mounted

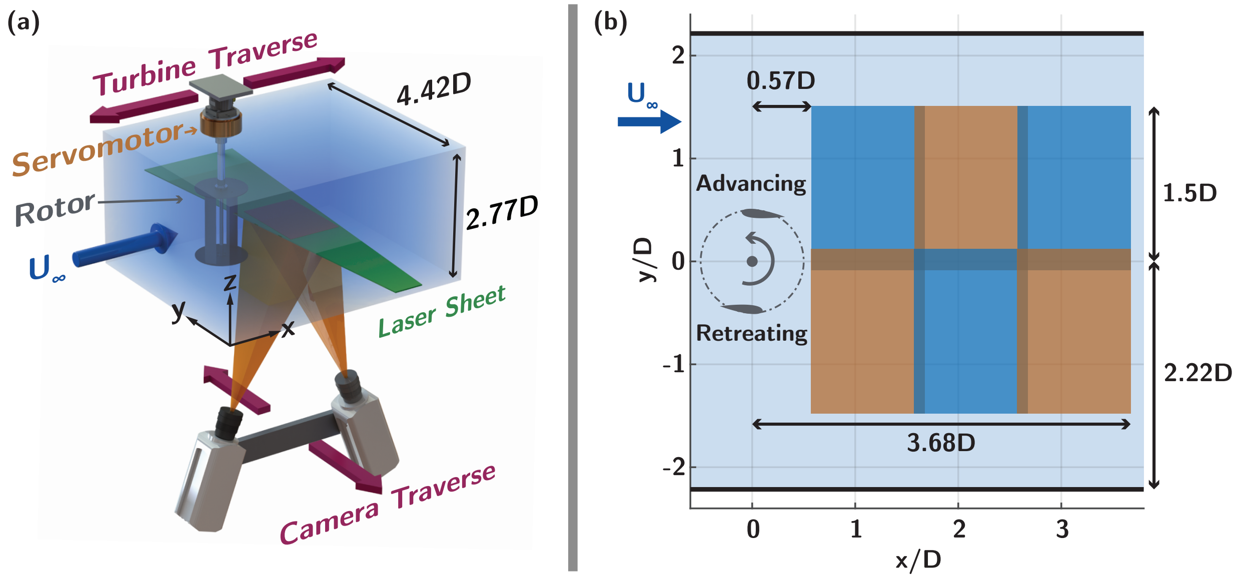

Figure 4.2: Turbine and PIV measurement setup diagram **(a)** and PIV measurement locations in the mid-plane along the z direction **(b)**.

to a robotic gantry system, providing accurate translation of the rotor in the streamwise direction.

4.2.2 PIV Measurement

Measurements of the turbine wake were taken using time-resolved stereo planar PIV. Data was collected in a free-running manner at 100 Hz, corresponding to 5.35 degrees of blade rotation between measurements, and was not locked to specific blade positions. Measurements were taken at the mid-span of the turbine, in the plane normal to the axis of rotation. Illumination was provided by a Continuum TerraPIV Nd:YLF laser, and images were captured by two Phantom V641 cameras, with resolutions of 2560 × 1600 pixels. Cavitation bubbles from the flume recirculation pump were used as passive tracers and measured approximately 1.5 pixels in diameter. Measurement resolution was increased by capturing the wake using six overlapping fields-of-view, as illustrated in Fig. ?? **(a)**. The combined measurement area, shown in Fig. ?? **(b)**, started $0.57D$ downstream from the turbine axis, and extended $3.68D$ downstream, and $3D$ in the cross-stream direction.

Spatial calibration was performed with custom stereo calibration target spanning the entire width of the flume section in conjunction with a robotic camera gantry used to repeatably move the cameras in the cross-stream direction. Post processing was performed with custom image manipulation software and TSI Insight for the cross-correlation. Ghost velocities due to small laser-sheet / calibration target misalignment was corrected through image warping in post processing. Velocity fields were calculated using iterative multi-grid processing, with initial square interrogation window side size of 64 pixels and a final size of 16 pixels. With 50% window overlap, the resulting velocity vector spacing was $0.0068D$.

4.3 Triple Decomposition Methods

In this work, a new triple decomposition method using the optimal dynamic mode decomposition algorithm is compared with several traditional methods. The PIV data was collected in a free-running manner, so was not locked to the turbine blade position. Three types of conditional averages based on the turbine blade position at the time of PIV image capture were computed. In these methods, PIV data was binned based on blade position. Subsequently, the median, mean, or weighted mean flow field velocities are calculated. Because of the free-running nature of the data acquisition, some error is introduced in these methods due to the error between the actual blade position and the position of the bin center. This motivates the use of a Fourier-series based reconstruction, wherein a series of sine functions are fit to the data, then the resulting function is used to reconstruct the data at the bin-center blade positions of the average-based methods, eliminating the inter-bin blade position error. For a finite number of terms in the Fourier series, selection of the base oscillation frequency becomes paramount to Fourier-based method performance. A natural choice for this flow is the blade-pass frequency and its harmonics. However, the question of whether other frequencies play an important role in the energetics of the wake motivate the use of DMD as a tool for identifying multiple wake oscillation frequencies and ranking and reconstructing their mode shapes. This method draws strong inspiration from the so-called optimal mode decomposition based triple decomposition of [16] but is presented in the framework of DMD. A related method that could be used is spectral POD, an implementation of the original POD of [117], with the ”spectral POD” terminology introduced by [148]. A detailed account of the relationship between spectral POD and DMD is given by [194].

Blade Position Conditional Averages

The first and simplest method of computing the oscillating component of the flow field at single point in space is to collect all n measurements for which the blade position, θ satisfies

$$|\theta - \theta_i| < \Delta\theta, \tag{4.4}$$

where $\Delta\theta$ is the half bin width and θ_i denotes the ith bin center, and compute the bin mean as

$$\widetilde{\boldsymbol{u}}(\boldsymbol{x}, \theta_i) = \frac{1}{n}\sum_{j=1}^{n}\left(\boldsymbol{U}(\boldsymbol{x}, \theta_j) - \overline{\boldsymbol{u}}(\boldsymbol{x})\right). \tag{4.5}$$

In an effort to reduce the sensitivity of this method to potential measurement outliers, the bin-median is similarly computed. The bin-mean method also introduces error through gradients in the flow field over the range of blade positions over the bin width. One solution is to shrink the bin width, but the number of measurements n occurring in the bin vary inversely with $\Delta\theta$. If n becomes small, turbulent fluctuations result in an average that does not accurately represent the periodic component of the flow. In an effort to reduce bin-width error while maintaining higher statistical certainty, a weighted average, where the weight of each measurement varies inversely with its distance from the bin center, is computed as

$$\widetilde{\boldsymbol{u}}(\boldsymbol{x}, \theta_i) = \frac{\sum_{j=1}^{n}\left(\boldsymbol{U}(\boldsymbol{x}, \theta_j) - \overline{\boldsymbol{u}}(\boldsymbol{x})\right)|\theta_i + \Delta\theta - \theta_j|}{\sum_{j=1}^{n}|\theta_i + \Delta\theta - \theta_j|}. \tag{4.6}$$

In these methods, each half rotation of the rotor is assumed to be one period of flow oscillation due to the rotor geometric symmetry. Reconstruction error, when compared with the full flow field, was minimized with $\Delta\theta = 3°$, or 30 bins per half-revolution, resulting in, on average, $n = 66.7$ flow snapshots per bin.

Fourier Series Reconstruction

Another solution to statistical and bin-width errors of averaging methods is to perform a Fourier-series decomposition of the oscillating flow, given by

$$\widetilde{\boldsymbol{u}}(\boldsymbol{x}, \theta(t)) = \sum_{m=1}^{r} A_m(\boldsymbol{x}) \sin\left[m\omega t + \phi_m(\boldsymbol{x})\right]. \tag{4.7}$$

In the case of this flow, selection of the base oscillation frequency, ω, is simple given that the blade-pass frequency is the primary driver of flow oscillations. The same flow-field as the conditional average methods is then computed by reconstructing at times t_i that correspond to bin centers θ_i. In practice the coefficients and phase fields $A_m(\boldsymbol{x})$ and $\phi_m(\boldsymbol{x})$ are computed via the windowed fast Fourier transform, with the time series zero-padded appropriately to ensure the FFT output includes all r frequencies exactly equal to $m\omega$, removing potential frequency interpolation error. This is referred to in the following as the discrete Fourier transform (DFT) method.

Multi-Modal Decompostion

In many cases, the base oscillation frequency may be unknown, or the flow may exhibit features that oscillate at unrelated frequencies. In the case of a CFT wake, the blade-pass frequency may not be the only mechanism determining the time-scale of periodic fluctuations. This motivates a generalization of the triple decomposition to Eq. (4.2) as introduced by [16]. Here $\widetilde{\boldsymbol{u}}$ is split into fluctuating components whose frequencies are not necessarily related. Data-driven methods allow the triple decomposition to be used as an exploratory/diagnostic tool. The oscillatory components can be derived by a variety of techniques. In this work, we harness the Dynamic Mode Decomposition. Frequency, amplitude, and phase of oscillations are determined directly from velocity time series, reducing error introduced by conditional average and DFT methods.

Dynamic mode decomposition and optimized DMD

The dynamic mode decomposition (DMD) was introduced by [168] in the fluids community to identify spatiotemporal coherent structures from time-series data. In the simplest form, the DMD algorithm extracts the dominant eigenvalues and eigenvectors of the best-fit linear operator that approximately advances the measured state forward in time. The DMD algorithm starts with two snapshot matrices:

$$\mathbf{X} = \begin{bmatrix} | & | & & | \\ \mathbf{x}_1 & \mathbf{x}_2 & \cdots & \mathbf{x}_{m-1} \\ | & | & & | \end{bmatrix} \qquad \mathbf{X}' = \begin{bmatrix} | & | & & | \\ \mathbf{x}_2 & \mathbf{x}_3 & \cdots & \mathbf{x}_m \\ | & | & & | \end{bmatrix}. \tag{4.8}$$

The best-fit linear operator that maps $\mathbf{X}$ into $\mathbf{X}'$ is given by $\mathbf{A}$, satisfying the approximate relationship:

$$\mathbf{X}' \approx \mathbf{A}\mathbf{X}. \tag{4.9}$$

In practice, this matrix $\mathbf{A}$ may be approximated using the pseudo-inverse of $\mathbf{X}$, which is computed by taking the singular value decomposition $\mathbf{X} = \mathbf{U}\mathbf{\Sigma}\mathbf{V}^T$ and inverting each of the matrices $\mathbf{U}$, $\mathbf{\Sigma}$, and $\mathbf{V}^T$:

$$\mathbf{A} = \mathbf{X}'\mathbf{V}\mathbf{\Sigma}^{-1}\mathbf{U}^T. \tag{4.10}$$

The matrix $\mathbf{\Sigma}$ is diagonal, and both $\mathbf{U}$ and $\mathbf{V}$ are unitary, so matrix inversion is simple. However, if the state $\mathbf{x}$ is a large discretized fluid velocity or vorticity field, the matrix $\mathbf{A}$ may be intractably large to represent, let alone to analyze. Instead, we compute the projection of $\mathbf{A}$ onto the leading POD modes, given by the columns of $\mathbf{U}$:

$$\tilde{\mathbf{A}} = \mathbf{U}^T\mathbf{A}\mathbf{U} = \mathbf{U}^T\mathbf{X}'\mathbf{V}\mathbf{\Sigma}^{-1}. \tag{4.11}$$

The matrices $\mathbf{A}$ and $\tilde{\mathbf{A}}$ share the same eigenvalues, so it is possible to compute the spectrum of $\mathbf{A}$ by computing the eigendecomposition of $\tilde{\mathbf{A}}$:

$$\tilde{\mathbf{A}}\mathbf{W} = \mathbf{W}\mathbf{\Lambda} \tag{4.12}$$

where $\mathbf{W}$ contain the eigenvectors of $\tilde{\mathbf{A}}$ and $\mathbf{\Lambda}$ contains the eigenvalues. Finally, it is possible to compute the high-dimensional eigenvectors $\mathbf{\Phi}$ of the matrix $\mathbf{A}$, e.g. the DMD modes, from the low-dimensional eigenvectors $\mathbf{W}$ using the *exact* DMD algorithm of [195]:

$$\mathbf{\Phi} = \mathbf{X}'\mathbf{V}\mathbf{\Sigma}^{-1}\mathbf{W}. \tag{4.13}$$

It is well known that DMD is sensitive to noisy data [53, 84, 9], and the optimized DMD algorithm of [9] overcomes this sensitivity by considering the evolution of all of the snapshots at once, instead of through a single iteration through the map $\mathbf{A}$. This is, in general, a non-convex procedure, although there are efficient algorithms to compute this optimization, and the results indicate considerable noise robustness over standard algorithms. In addition, optimized DMD enables processing on time-series data that are not evenly space in time and further allows for constraints and restrictions on the eigenvalues, for example, allowing the user to specify that all eigenvalues are on the unit circle. This is critical for the triple decomposition, where modes are expected to have zero growth or decay. The standard DMD algorithm could be used to determine oscillatory flow components by either selecting modes with imaginary-only Eigenvalues, or by manually zeroing the real part of the eigenvalues. However, the original mode shapes returned by exact DMD are no longer guaranteed to best represent the data given the now altered Eigenvalues. Optimal DMD circumvents this issue by iteratively optimizing the mode shapes given constraints on the eigenvalues.

In this work, the optDMD-based triple decomposition is compared with the methods described above. Additionally, it is used as a discovery tool to explore the dynamics of the CFT wake.

4.3.1 LCS Methods

Lagrangian coherent structures (LCS) are useful for identifying coherent regions of unsteady fluid flows that are segmented by time-varying separatrices, which are the unsteady analogues of stable and unstable invariant manifolds from dynamical systems [82, 170]. LCS are often computed as the second derivative ridges of the finite-time Lyapunov exponent (FTLE) field

[170] which describes the maximum rate of stretch of a Lagrangian packet of fluid over a finite time period.

The more recent method of [64] uses variational theory to compute LCS from FTLE fields. The FTLE field is generally computed by integrating passive tracer particles along the flow of the velocity field $u(x, t)$ as follows:

$$\Phi_{t_0}^{T}\left(x(t_0)\right) = x(T) = x(t_0) + \int_{t_0}^{t_0+T} u(x(\tau), \tau)\, d\tau, \tag{4.14}$$

where $\Phi_{t_0}^{T}$ is the flow map. Next, the flow map Jacobian, $D\Phi_{t_0}^{T}$ is approximated via finite-difference derivatives with neighboring points in the flow. In two dimensions, the flow map Jacobian at a point $\mathbf{x}_{i,j}$ is:

$$\left(D\Phi_{t_0}^{T}\right)_{i,j} \approx \begin{bmatrix} \frac{x(t_0+T)_{i+1,j} - x(t_0+T)_{i-1,j}}{x(t_0)_{i+1,j} - x(t_0)_{i-1,j}} & \frac{x(t_0+T)_{i+1,j} - x(t_0+T)_{i-1,j}}{y(t_0)_{i+1,j} - y(t_0)_{i-1,j}} \\ \\ \frac{y(t_0+T)_{i,j+1} - y(t_0+T)_{i,j-1}}{x(t_0)_{i+1,j} - x(t_0)_{i-1,j}} & \frac{y(t_0+T)_{i,j+1} - y(t_0+T)_{i,j-1}}{y(t_0)_{i+1,j} - y(t_0)_{i-1,j}} \end{bmatrix}. \tag{4.15}$$

From a continuum mechanics standpoint, this is a numerical computation of the deformation gradient. The finite-time Lyapunov exponent σ is computed from the largest eigenvalue λ of the Cauchy-Green deformation tensor $\mathbf{\Delta} = \left(D\Phi_{t_0}^{T}\right)^{\intercal} D\Phi_{t_0}^{T}$, which is the maximum singular value of the flow map Jacobian:

$$\sigma(x_0, t_0, T) = \frac{1}{T} \ln\left(\sqrt{\lambda_{\max}\left[\mathbf{\Delta}(x_0, t_0, T)\right]}\right). \tag{4.16}$$

The variable σ is a scalar field that is typically computed on a discrete grid of particles, and for unsteady flows this field is recomputed at every time step, introducing redundant computations that may be eliminated [35, 116]. When σ is large, then neighboring particles undergo considerable stretching along the flow, while particles with small σ will tend to remain in coherent patches with their neighbors. The FTLE field may be computed by integrating particles either forward or backward time, and the ridges correspond to repelling or attracting structures, respectively.

As the integration period, T, is increased, the ridges of the FTLE field become more defined, though their locations remain constant [79]. For studies with limited interrogation windows, such as this one, this can present a problem. Increasing integration time results in more finely resolved FTLE ridges, but increases the chance that a passive tracer will exit the flow-field before the end of the integration. A partial solution to this issue is to subtract the global (for all time and space) mean velocity vector from the flow field, thereby slowing the propagation of seeded particles through the domain. This will not effect the mechanics of a Lagrangian fluid packet. However, with flows that exhibit local velocities differing significantly from the global mean, this strategy is only partially effective since the local velocities can still eject the passive tracers. FTLE computations presented here assign passive tracers that leave the domain their FTLE value at the time of exit, resulting in a decrease in FTLE ridge definition near some domain edges.

4.4 Results and Analysis

4.4.1 Mean Flow

The mean wake deficit contours and normalized velocities are shown in Fig. 4.3. As in prior work, we observe an asymmetric wake deficit with an intense shear layer on the advancing side of the wake (see Fig. **??** **(b)** for advancing versus retreating sides). Wake deficit recovery occurs faster on the retreating side, as described by [192]. The mean wake deficit is never negative, meaning there is no recirculation region at this turbine operating point at this turbine operating point. [5] showed a decrease in wake deficit with reduction in the number of blades, however, even the two-bladed turbine showed some negative streamwise velocity. A survey of wake measurements in prior work indicates that neither rotor efficiency, solidity, nor the expression of dynamic solidity of [5] are good predictors of whether or not a negative wake deficit occurs. It is possible that some combination of these factors in addition to the test section blockage ratio would be necessary to predict the magnitude of the wake deficit.

Despite the differing geometry, the streamwise wake velocity is very similar to those

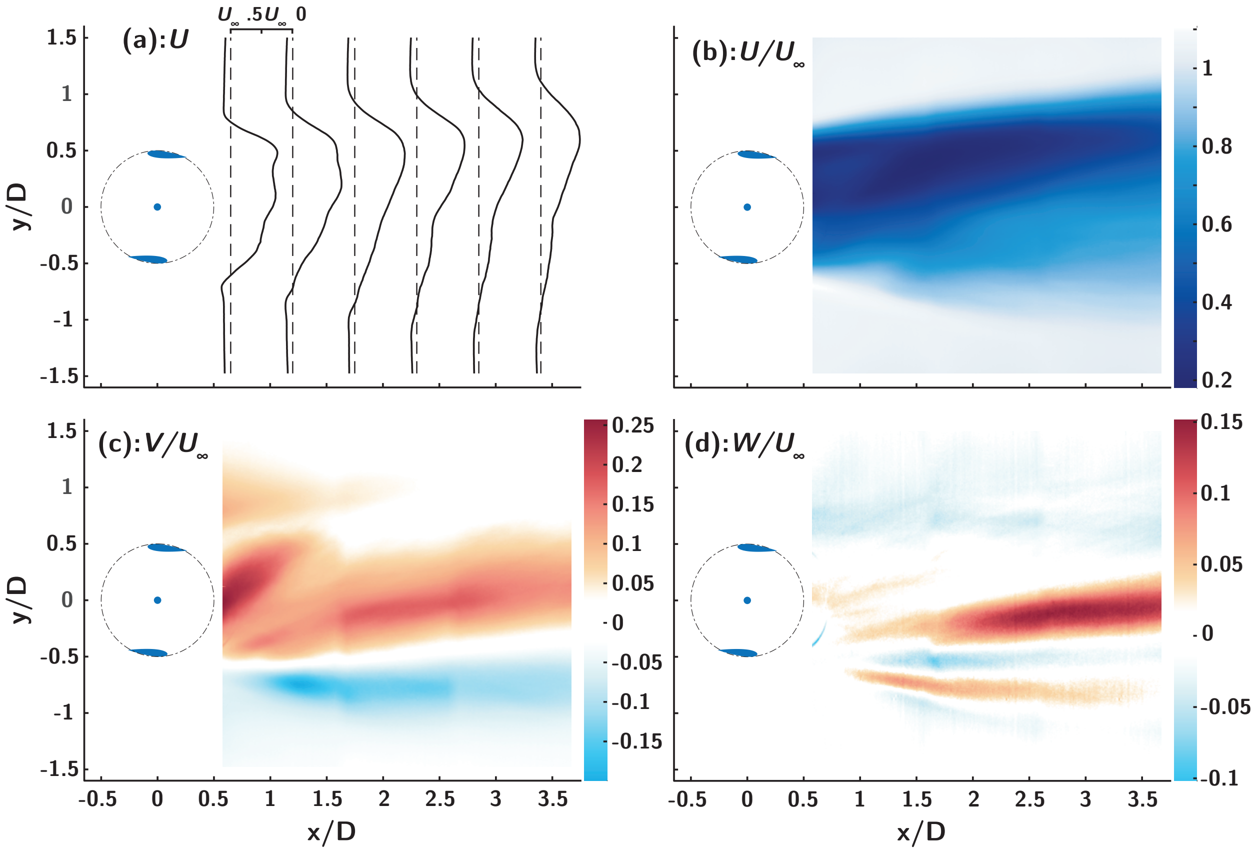

Figure 4.3: **(a)** Mean wake deficit profiles. Streamwise velocity profiles along cross-stream stations (dashed lines). The distance from one station to the next is a change in velocity equivalent to the mean freestream velocity, U_∞. **(b)** The mean streamwise, **(c)** cross-stream, and **(d)** vertical (axial) velocities, normalized by the freestream velocity. The turbine is rotating counter-clockwise

published by [146] (five blades, high c/R) and [86] (three blades, low c/R), suggesting that rotor geometry has limited effect on the mean wake.

There seems to be significant disagreement concerning the root cause of the asymmetry of the mean wake profile. Some of these are given here:

- [5] “In all cases, there is a notable asymmetry of the VAWT wake. This is attributed to the stronger shear layer that forms on the side of the turbine where the blades are advancing upstream.”

- [86] “This behavior is as expected, as the majority of the power is generated on the advancing side of the turbine, and therefore a larger momentum deficit will be seen on this side.”

- [12] compares the effect to that of a rotating cylinder, stating “Compared with the rotating cylinder wake measurements...” “we see a similar asymmetry in the mean streamwise velocity. The wake is less asymmetrical with respect to the wake centreline for the turbine compared to the rotating cylinder for the same nondimensional rotation rate, although some of these differences may be due to the cylinder experiments.”

- [146] gives multiple explanations: “There are two major factors that may contribute to this wake asymmetry. One factor is that more turbulent structures are produced at the windward than at the leeward. When the blade advances under adverse pressure gradients at the windward, stronger vortex shedding and much severer flow separations take place. The other factor is that the wake flows are transported toward the windward. First, when the blade moves upwind at the windward, it causes stronger blockage effect compared to that at the leeward. Therefore, at the windward, the blade wake is characterized by a lower pressure, which induces the cross-wind flows. Second, when

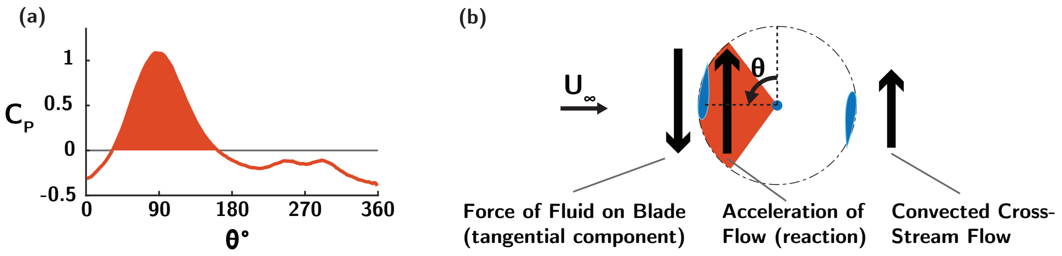

Figure 4.4: **(a)** Measured power coefficient as a function of azimuthal blade position for a single blade in a CFT. **(b)** Diagram of the force exerted on the blade by the fluid necessary for power production, the resulting reaction force and acceleration of flow, and the resulting convected cross-stream flow which leads to wake deflection.

> the blade operates at the downstream half-revolution, the strong angular momentum drags and propels the wake flows toward the windward. ”

We propose a simpler explanation as the main mechanism for wake asymmetry. Force measurements of a single blade of a CFT indicate that the majority, it not all of the power is produced on the upstream side of the rotor, with peak power production center on approximately $\theta = 90°$ (immediately eliminating the explanation of [86]). This is illustrated in Fig. 4.4 **(a)**. Power production requires a force component be applied to the blade in the tangential direction during this region, generally in the $-\widehat{y}$ direction in the coordinate system used here. As a consequence of this application of force, the fluid must experience an acceleration in the opposite direction, in this case in the $+\widehat{y}$ direction. The incoming freestream flow has no significant velocity in the $\widehat{y}$ direction. This effect is analogous to the angular velocity induced in an axial-flow turbine wake, where the induced flow is opposite the direction of turbine rotation. In the case of the CFT, this flow velocity induced in the cross-stream direction is advected downstream through the rotor to the wake, as depicted in Fig. 4.4 **(b)**. Strong evidence of this cross-stream velocity is seen in the Fig. 4.3 **(c)**, though the action of blade tip vortices could also induce flow in this direction [20].

Examining Fig. 4.3 **(d)**, it is curious to note significant vertical (axial) velocities present. Because we are sampling on the mid-plane and the turbine rotor is symmetric about this plane, one would expect the wake to reflect this symmetry, resulting in no out-of-plane velocities. However, [146] and [156] both observe similar asymmetries. Interactions with the free-surface or the flume floor boundary layer could be mechanisms for this phenomenon, though the former is unlikely as mid-plane vertical flows have been observed in wind-tunnel measurements. The stability of coherent wake structures may play some role in this asymmetry, as described later.

4.4.2 Triple Decomposition Methods Comparison

Next, the oscillatory component of the flow is analyzed. However, first the performance of several methods of extracting the periodic flow is compared, including a new method harnessing the optDMD algorithm. For each algorithm, described in the methods of this chapter, the periodic component is extracted, reconstructed for the full length of the original data set, then added back to the mean flow ($\overline{\boldsymbol{u}} + \widetilde{\boldsymbol{u}}$). The reconstruction is compared to the original flow in two ways. First, the average $L2$ error between the reconstruction and original data is computed. Second, the total sum of the flow kinetic energy over space and time is computed for the original and reconstructed flow. The ratio of these energies is indicated by the vertical axis of Fig. 4.5**(a)**, while the error is on the horizontal. The DMD-based method results in more energy explained and a lower error from the original dataset. For the DFTc method, the base oscillation frequency (the blade pass) is calculated from the average location of the peak of the flow data spectra. In the DFTm method, this base frequency is calculated from the encoder data collected during turbine operation. Small error in the encoder-measured frequency versus the true frequency results in large oscillation phase errors during reconstruction. This illustrates the importance of knowing or calculating the base frequency of interest exactly using these methods.

The DMD method does not require a-priori knowledge of the base frequency, and can be used as a tool to uncover flow phenomena oscillating at related or unrelated frequencies. As

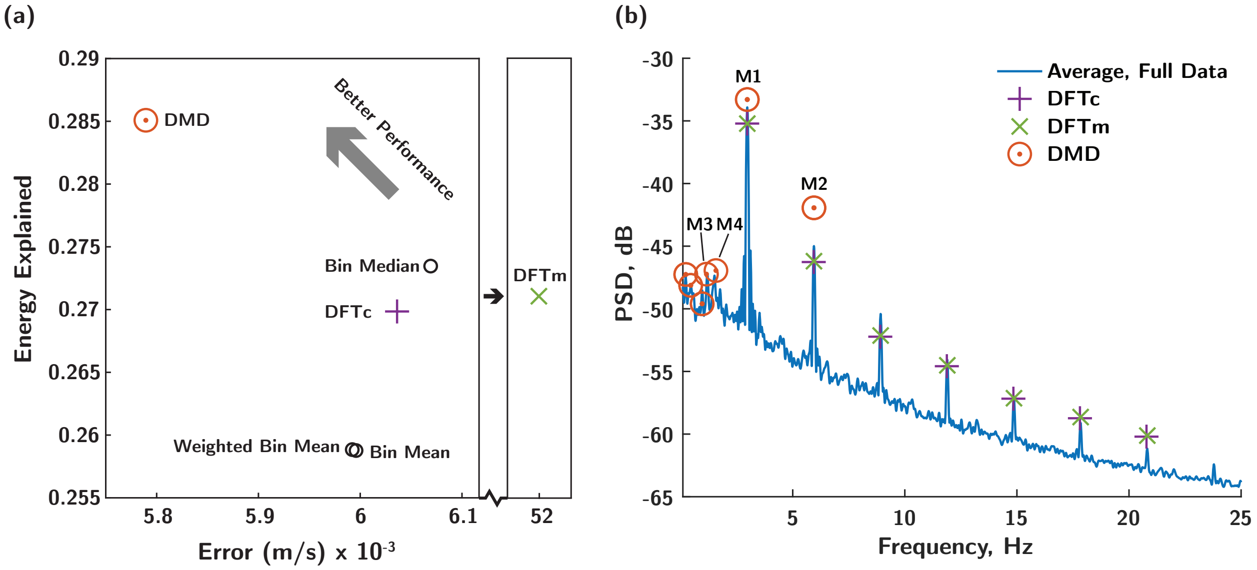

Figure 4.5: **(a)** Kinetic energy content of the mean plus the reconstructed periodic flow normalized by the kinetic energy content of the full flow measurements versus the $L2$ error of the reconstruction versus the original flow. We expect the most effective triple decomposition method to minimize the error while maximizing the amount of energy capture (as indicated by the arrow). **(b)** Power spectra of the modes of the DFT and DMD methods. DMD indicates importance of low-frequency modes that may not be discovered by other methods. The first four DMD modes are labeled **M 1**→ **4**.

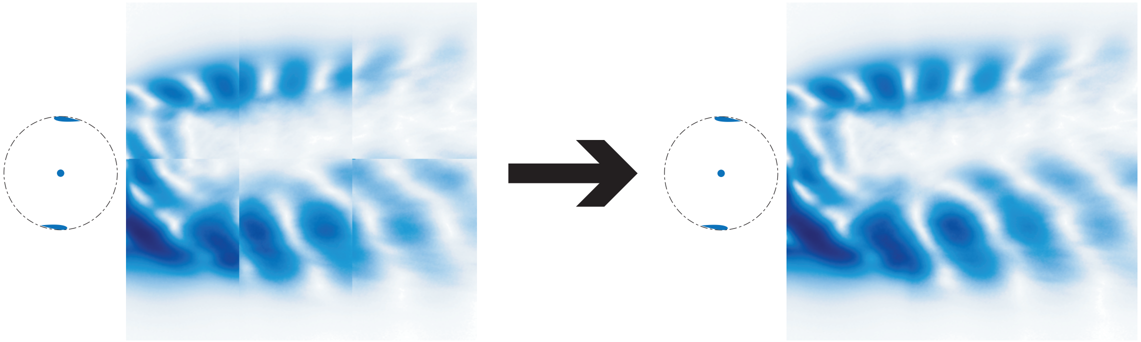

Figure 4.6: DMD mode phase correction process shown on the first DMD mode of the turbine wake data. Because data was collected at differing times, the phase of oscillation of the same mode in differeing fields-of-view are not aligned. A numerical minimization of the error in field-of-view overlap regions is used to correct the phase. For this example, this is a five-variable optimization problem (one field-of-view is the reference).

illustrated by Fig. 4.5**(b)**, the first seven modes extracted by the optDMD algorithm contain the blade pass frequency and its first harmonic, followed by five lower-frequency modes. To view these modes in terms of the full wake, not just the separate fields-of-view collected, the phase of oscillation of each mode in each individual field-of-view was adjusted via numerical optimization to match the oscillation of neighboring fields-of-view. This process is illustrated in Fig. 4.6 and details are given in appendix A.2.

4.4.3 Wake DMD Modes

The optDMD triple decomposition extracts and ranks oscillatory modes in terms of energy content. The first four modes are shown in Fig. 4.7 and their corresponding frequencies are identified in Fig. 4.5**(b)**. Modes are computed using all three velocity components as measurement inputs. For compactness, the horizontal velocity magnitude, or

$$U_H = \sqrt{u^2 + v^2} \tag{4.17}$$

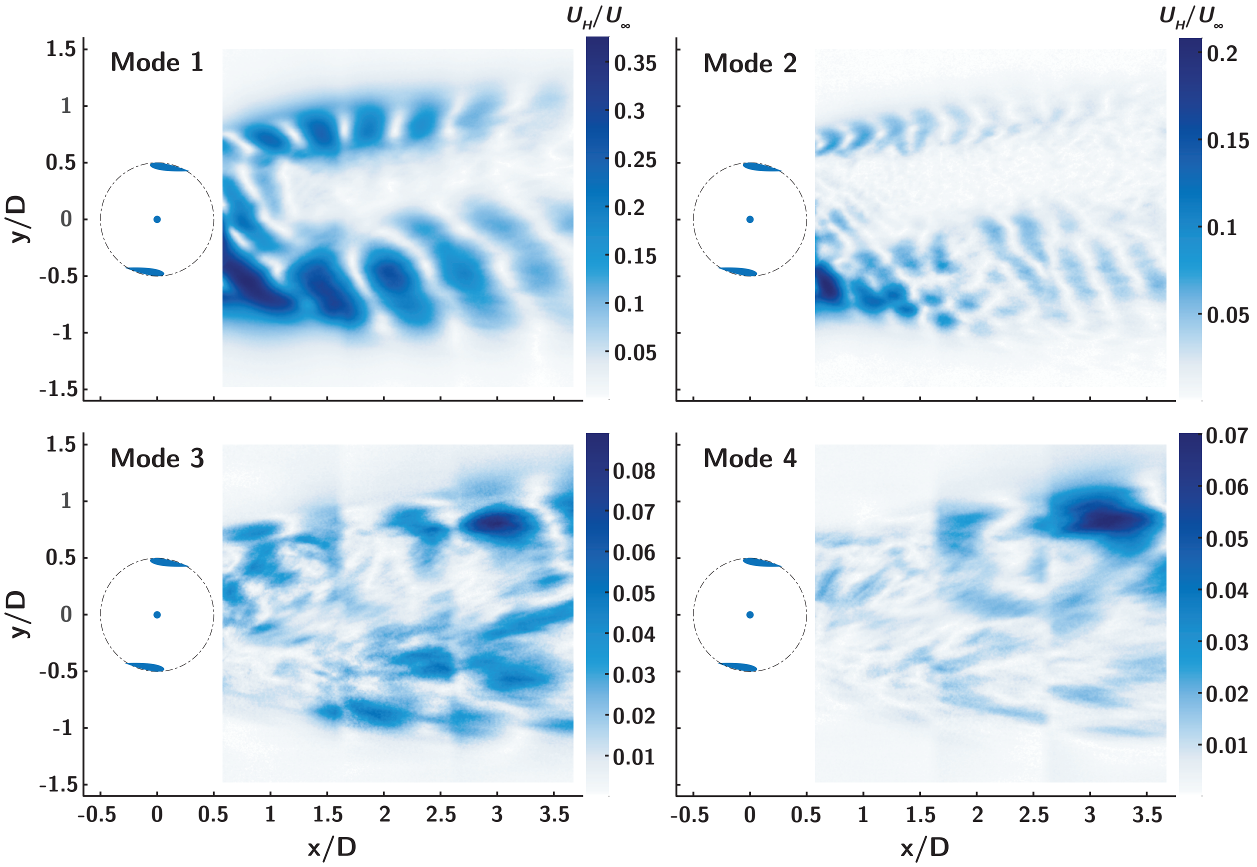

Figure 4.7: Modes extracted using the optDMD algorithm, with the phase of oscillations corrected. Modes are ranked by energy content and are identified by the **M** labels in Fig. 4.5**(b)**.

is plotted in Fig. 4.7. As mentioned previously, modes one and two correspond to the blade pass frequency and its first harmonic. The prominence of mode two indicates that the waveforms of the blade pass oscillation deviate significantly from sinusoidal. The first harmonic energy content decreases faster in the downstream direction than the fundamental frequency, perhaps due to the more rapid dissipation of the smaller-scale features. The structures responsible for the energetic oscillations at the blade-pass frequency will be discussed in the following section. The frequency of the third mode is half the blade-pass frequency. In the very near wake, energy in this mode illustrates changes in flow due to small geometric differences in the rotor blades or their mounting angle. Together, modes three and four illustrate illustrate a phenomenon on the advancing side of the wake. Structures that initially occur at the blade pass frequency seem to be breaking down or combining into lower-frequency structures in a repeatable manner. This could be evidence of a transition toward the to the bluff-body far wake oscillation documented by [5]. However, the frequency of mode four is 1.18 Hz, while the predicted bluff-body frequency for a cylinder of the same diameter as the rotor is 0.8 Hz. It is possible that full transition to the bluff-body frequency has not yet occurred, and that measurements made further downstream would show lower dominant frequencies.

4.4.4 Wake Coherent Structures

In addition to analyzing the frequencies of different components of the oscillating wake, it is illuminating to examine the time evolution of periodic coherent structures. In Fig. 4.8 we show the forward and backward FTLE fields computed from the mean and the reconstructed periodic component from the DMD analysis above. In these figures we observe the structures driving the flow oscillation that was evident in the first two DMD modes. On the advancing side of the wake is a vortex street with vorticity opposite the direction of turbine rotation. Roll up of the strong shear layer in the flow, as shown in Fig. 4.3**(a)** and **(b)** is likely the energetic source for these vortices, while the disturbance caused by the blade pass ensures the roll-up occurs at a regular frequency. It is possible that the blade sheds some vorticity as

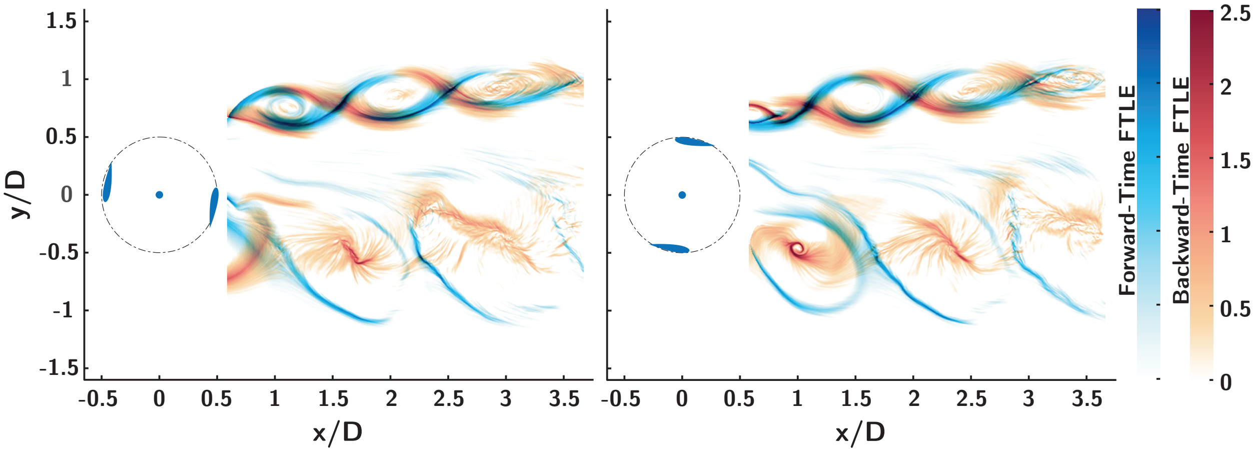

Figure 4.8: Forward and backward FTLE fields computed on $\overline{\boldsymbol{u}} + \widetilde{\boldsymbol{u}}$. These fields represent areas of maximum stretch and convergence respectively, and together outline the boundaries of coherent structures.

well, but the arrangement of the shear layer means this is not necessary for vortex roll-up.

On the retreating side of the wake, a large vortex structure is also shed, but is due to a completely different mechanism. During the lift production portion of the blade stroke (the center of which is when the blade is farthest upstream) lift production requires the generation of counter-clockwise circulation around the blade. Because this circulation is not permanent, but is created every rotation, packets of opposite circulation must be shed into the wake[20]. Detailed analysis of the actual formation of this vortex structure on the blade would require further measurements upstream, but the vortex has the correct sign to be a trailing edge vortex perhaps partly in response to a leading edge vortex formed during dynamic stall. This structure dissipates more quickly than the vortex street on the advancing side, perhaps in part due to the lack of a strong energizing shear layer on this side of the wake. At the same time, mixing due to this structure may contribute to the lesser shear layer and faster wake recovery on the retreating side (see Fig. 4.3**(a)**).

The shed vortex structure on the retreating side is more complex than a single rotating

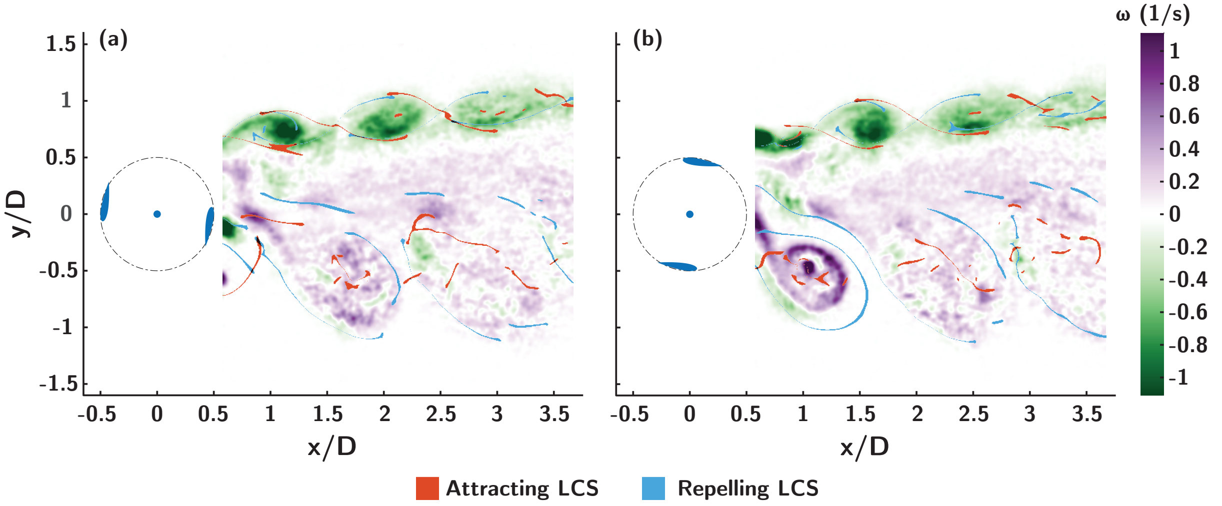

Figure 4.9: Second derivative ridges of the FTLE field superimposed on the flow vorticity.

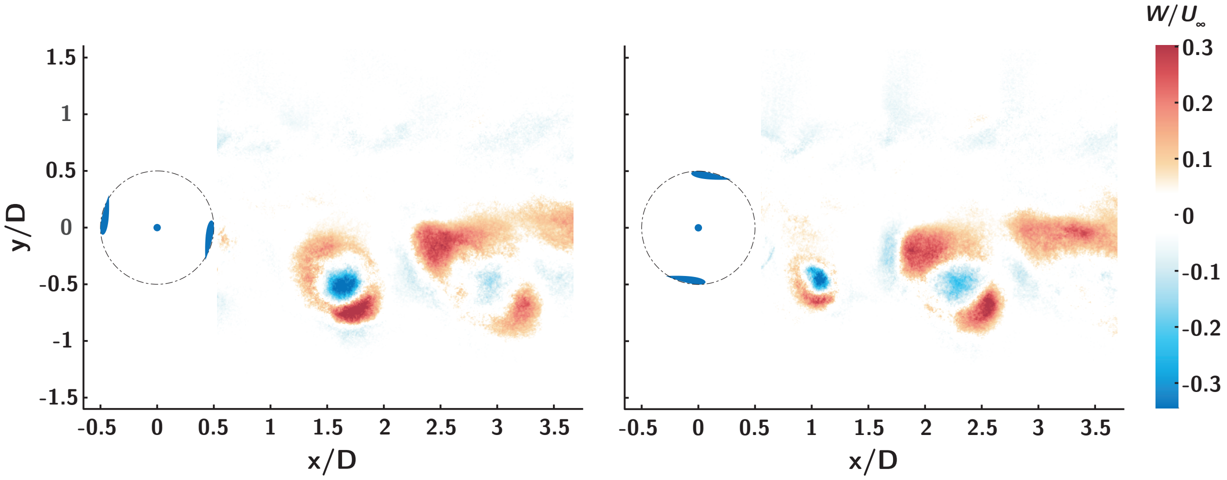

Figure 4.10: Out-of plane (vertical) velocity, mean and periodic component ($\bar{w}+\tilde{w}$). Regions of vertical flow correspond to the core and periphery of the retreating side vortex structure.

packet of fluid. It appears that a intense core of vorticity is surrounded by a ring of vorticity of the same sign. This unstable arrangement may be partially responsible for the rapid breakdown of this structure, though to see why it is able to survive at all we must examine the out-of-plane (w) velocity, shown in Fig. 4.10. The inner vortex core has intense axial velocity in the negative direction, while the outer vorticity ring has vertical velocity towards the flume free surface. We see now that the out-of-plane velocity observed in the mean wake (Fig. 4.3**(d)**) is entirely due to this structure. It appears that this structure already contains significant axial flow when it is shed into the wake, so it seems unlikely that it due purely to asymmetries in the freestream velocity and their influence on shed tip vortices. Axial flow in dynamic-stall related structures has been reported in insect flight [25] and delta wing aircraft [204]. Additionally, the results of section 3.2 indirectly suggest the importance of axial flow in CFT performance. However, the source of the pressure gradient that can drive vertical flow within a rotor that is symmetric about the mid-plane remains unknown.

Of interest in terms of closely spaced downstream turbines is the predictability of the trajectory of wake coherent structures. Very regular structures may be more easily harnessed or avoided. In figure Fig. 4.11**(a)** and **(b)**, the core of the retreating side vortex is tracked. All tracks are shown in Fig. 4.11**(c)**, and in **(d)**, the probability density of the cross-stream location of the vortex core is plotted as a function of streamwise vortex core position. The position of the vortex core increases in uncertainty rapidly. This indicates that the vortex longevity may be greater than that predicted by just the periodic component of the flow, which both the optDMD modes and FTLE are based. However, regardless of longevity, the rapid increase in uncertainty of trajectory means the structure is unlikely to be intercepted predictably by downstream turbines.

4.5 Discussion

In an array setting, vortices shed on the retreating side of the wake likely dissipate too fast to be of concern in terms of effecting downstream rotor performance. The vorticies in the advancing side shear layer last longer in the wake and transition to lower frequency structures.

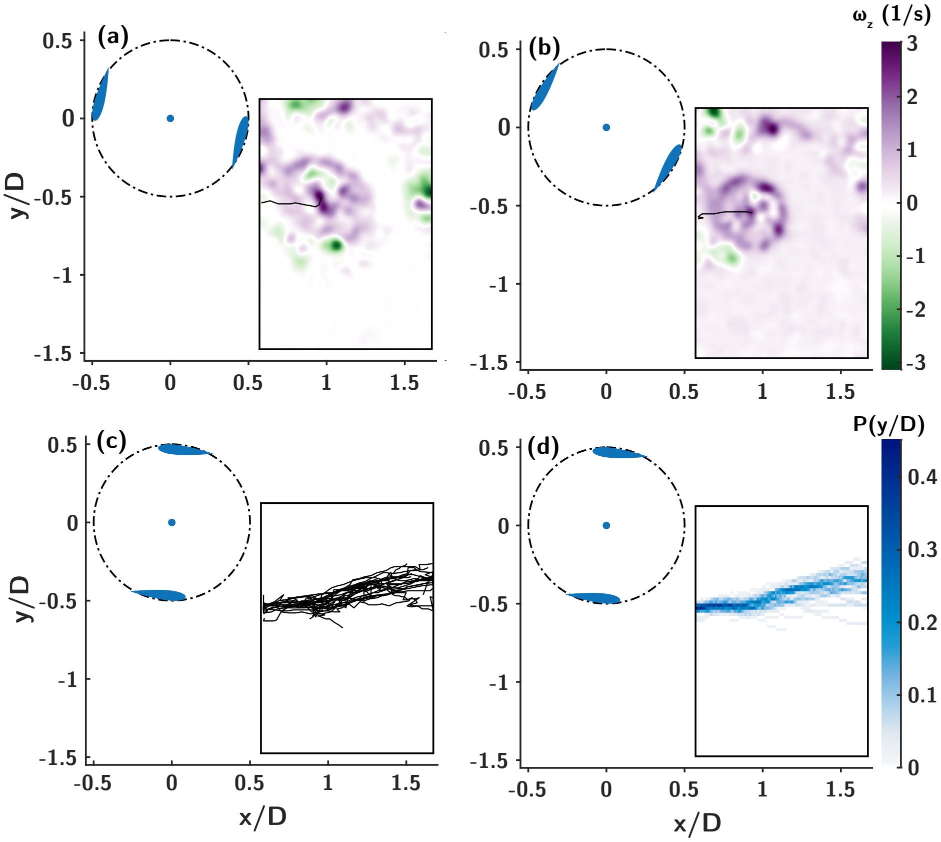

Figure 4.11: Retreating side vortex core tracking. **(a)** and **(b)**, example tracks and the corresponding vorticity fields. **(c)** All 50 tracks for the sampling period. **(d)** Probability distribution of track y/D location.

These may be large enough to engulf entire downstream rotors, though the energy contained in these structures is quite low (see the magnitude of DMD mode 4, Fig. 4.7).

This dataset is collected at a Reynolds number that is likely lower than that of commercial-scale turbines. An increase in Reynolds number may increase the dissipation rate of coherent structures, as well as their trajectory and strength[154]. However, it is felt that general trends and phenomena observed will hold true for large scales. The blockage ratio of 11% may increase the bypass flow velocity and reduce the wake velocity deficit compared to the unconfined case, thereby intensifying the shear on the advancing and retreating sides..

4.6 Conclusions

Detailed analysis of a CFT wake through stereo PIV measurements of the rotor mid-plane has been presented. The mean wake structure has been found to be similar to prior experiments, despite the uniquely high c/R of this turbine. A simple explanation for CFT wake skew in the direction of rotation is presented. A new method using the optDMD algorithm for extracting the periodic component of a flow is presented. This may be used a discovery tool for oscillating structures, especially in cases were multiple unrelated frequencies are present. Additionally, through phase correction, this method can be used on data that has been collected on overlapping fields-of-view, without knowledge of the temporal relationship between data acquisition runs. Finally, we present the first detailed description of Lagrangian coherent structures in a CFT wake. Vortex streets on the advancing and retreating sides are observed and their formation mechanisms described. We observe remarkably high axial flow in the core of the vorticies associated with lift production, those on the retreating side of the wake. This axial flow appears to be present before the vortex leaves the confines of the rotor.

Chapter 5

ADVANCED CFT CONTROL

Control of CFTs to maximum power output by optimizing the position on the TSR-C_P curve (region II control), or to limit the power output when the available power in the freestream exceeds the generator rating (region III) is still an active area of research [136, 96, 69]. Generally speaking, these control schemes seek to optimize in response to variations in the freestream velocity that have time-scales on the order of the diameter advection time ($\Delta t \approx \frac{D}{U_\infty}$). The control schemes presented in this chapter have a different objective. Here we aim to increase the maximum efficiency CFTs through optimization of the fluid-blade interactions via blade kinematics. The time-scales of importance in this type of control are much shorter, on the order of one chord translation of the blade ($\Delta t \approx \frac{c}{\omega R}$).

In the first section, we present a controller that, by carefully oscillating the angular velocity of the rotor, is able to boost mean power output 59%. In the second section, we optimize control and geometry of a two-rotor array, including a new control type that seeks to leverage the coherent wake structures described in the previous chapter.

5.1 Variable Angular Velocity Control

The following contains content from [184][1]

In some operating conditions, the flow separates from CFT blades, leading to the formation of leading-edge vortices. Drawing inspiration from biology, where flying and swimming animals achieve exceptional performance by harnessing similar unsteady flow struc-

---

[1] This work was published in Nature Energy as *Intracycle angular velocity control of cross-flow turbines*, DOI: 10.1038/nenergy.2017.103 and was co-authored with Brian Polagye and Steve Brunton. The author performed the experiments and wrote the manuscript. Springer Nature allows reproduction of an author's work in a dissertation.

tures [25, 197, 135, 43], it is possible to enhance turbine performance by actively controlling the blade kinematics. Previous approaches [103, 144, 169] have pitched the blade mechanically, much as a helicopter will pitch blades down during blade advance and up during blade retreat to achieve balanced loads.

Here we demonstrate an angular rotation rate controller based on blade position that requires no additional degrees of freedom (i.e., no additional moving parts) and instead optimizes the blade's nominal, or effective, angle of attack. As mechanical power is the product of torque and angular velocity, this approach directly controls one of these variables and maximizes the power extraction during periods of largest fluid forcing. For a structurally-robust turbine that operates at relatively low angular velocity, this method yields a 59% increase in power output over standard control methods. The increase in efficiency, which does not come at the expense of high rotation rates or mechanical complexity, could inspire mass commercial development of low-impact CFTs for power from wind and water currents.

Let us revisit the equation for the local, or nominal angle of attack of CFT blades, neglecting flow induced by the rotor:

$$\alpha_n(\theta) = -\tan^{-1}\left[\sin(\theta), \lambda(\theta) + \cos(\theta)\right] + \alpha_p(\theta), \tag{5.1}$$

where $\tan^{-1}$ is the four quadrant arctangent. Thus, the nominal angle of attack depends only on the blade pitch angle α_p and the tip-speed ratio λ:

$$\lambda(\theta) = \frac{\omega(\theta)\, R}{U_\infty}. \tag{5.2}$$

In their most general form, α_p and ω can be functions of θ, but in most cross-flow implementations both are held constant when compared to the timescale of one rotor rotation. The control set point, such as resistive torque or angular velocity, may be altered to adapt to the freestream conditions, but these changes are slow compared to the turbine rotation rate. In the control scheme presented here the varied parameter is the angular velocity function $\omega(\theta)$, which alters the tip-speed ratio and thus the angle of attack, as indicated by the red terms above.

As detailed previously, dynamics stall can occur in CFTs depending on the operating conditions and geometry. While dynamic stall is sometimes considered undesirable for CFT operation [37], birds [200], bats [135], insects [54], and falling maple seeds [111] have all been shown to execute maneuvers that exploit the dynamic stall process and resulting vortical structures. Dynamic stall has been used to maximize the objectives of engineering problems including the lift of a flapping flat plate [128], the thrust of an oscillating foil [89], and the power produced by a pitching and heaving foil [100, 7, 205, 186]. This suggests that CFTs may also benefit from dynamic stall if the increase in lift can be harnessed while minimizing the impact of the drag increase. This may be possible via careful timing between blade rotation and dynamic stall. First, due to the periodic variation in the nominal flow velocity, it may be possible to align the initial lift increase with a large nominal velocity and the subsequent drag increase with a region of lower nominal velocity. Second, optimized blade kinematics may hold a leading-edge vortex near the lifting surface of the foil for a significant portion of the rotation, thus increasing lift.

5.1.1 Intracycle control approach

Control based on the angular position of a CFT blade (i.e., $\alpha_p(\theta)$, $\omega(\theta)$) is referred to here as *intracycle control* to differentiate it from schemes that optimize turbine power over longer time scales in response to changes in the freestream velocity, such as [136, 96]. Approaches to intracycle control of CFTs can be split into two categories: schemes that alter the turbine kinematics and those that apply flow control to the foil surface to eliminate or delay separation of the upper foil boundary layer at high angles of attack (e.g., plasma actuators [80], synthetic jets [206]). While flow control has demonstrated benefits, many types of actuators would be difficult and expensive to implement commercially [34]. Here, we demonstrate a kinematic intracycle controller that exploits the benefits of dynamic stall rather than attempting to suppress it. The primary kinematic intracycle control scheme studied to date is active pitch control, in which the blade pitch angle varies as a function of angular position. This alters the nominal angle of attack via Eq. (1.3), where α_p is a function of θ. This con-

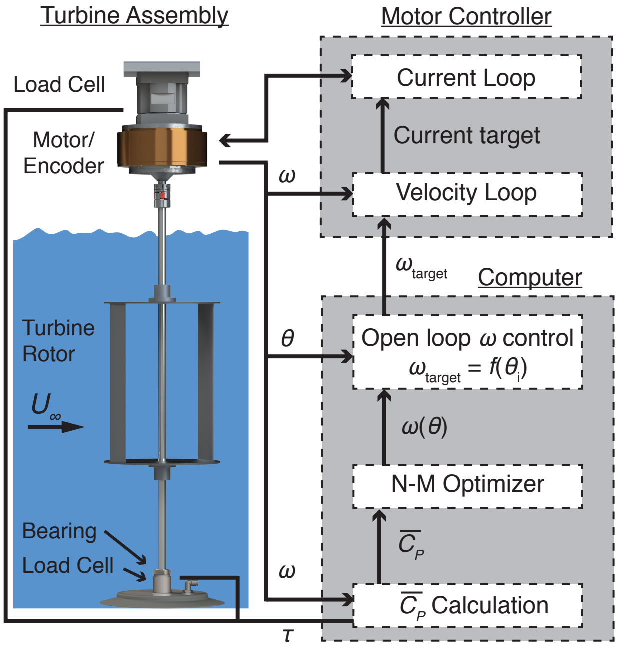

Figure 5.1: Turbine Setup and Control System. Schematic of the experimental setup and diagram of the control scheme including the Nelder-Mead optimization procedure. Turbine performance equipment and methods are as detailed in the methods chapter. During optimization of intracycle angular velocity control, turbine data is recorded for a period of 30 seconds while operating using a fixed control law. Control laws, consisting of periodic angular velocity profiles, are implemented by sending a velocity command to the motor controller based on the current turbine position. Turbine performance is then computed and used as the reward function for optimization via the Nelder-Mead algorithm. Additional details are provided in the methods chapter.

cept has been well studied both experimentally and numerically [103, 144, 169]. Increases in turbine efficiency of up to 24% have been demonstrated in experiments [103]. However, these methods have not been commercially adopted, perhaps because the increase in mechanical complexity outweighs the efficiency gains.

As is evident from Eq. (1.3), an alternative to blade pitch control is to modify the turbine rotation rate and thus the tip-speed ratio as a function of azimuthal blade position. As shown by the red terms in Eqs. (5.1) and (5.2), this provides another means of altering the nominal angle attack of the foil. An additional consequence is modification of the nominal velocity profile, Eq. (1.6). This method may be implemented without increasing the mechanical complexity of the CFT. Here, we explore the performance implications of two angular velocity profile parameterizations: a sinusoidal profile

$$\omega(\theta) = A_0 + A_1 \sin(N\theta + \phi_1), \tag{5.3}$$

and a semi-arbitrary profile (truncated Fourier series)

$$\omega(\theta) = A_0 + \sum_{i=1}^{3} A_i \sin(iN\theta + \phi_i). \tag{5.4}$$

The frequency is a multiple of the number of blades N to enforce periodicity and ensure that each blade experiences identical kinematics. If the freestream velocity U_∞ is quasi-steady, controlling ω is equivalent to controlling the tip-speed ratio $\lambda(\theta)$. Experimental tests of this control scheme were performed using a turbine with two straight blades in a recirculating water flume with a chord based Reynolds number of 31,000. The turbine control and measurement setup is shown in Fig. 5.1. Details of this system and turbine power calculations are given in the methods section. Angular velocity profiles were optimized using the Nelder-Mead downhill simplex method [139]. Figure 5.2 provides a high-level overview of the interplay between fluid forcing, control actuation, and power output.

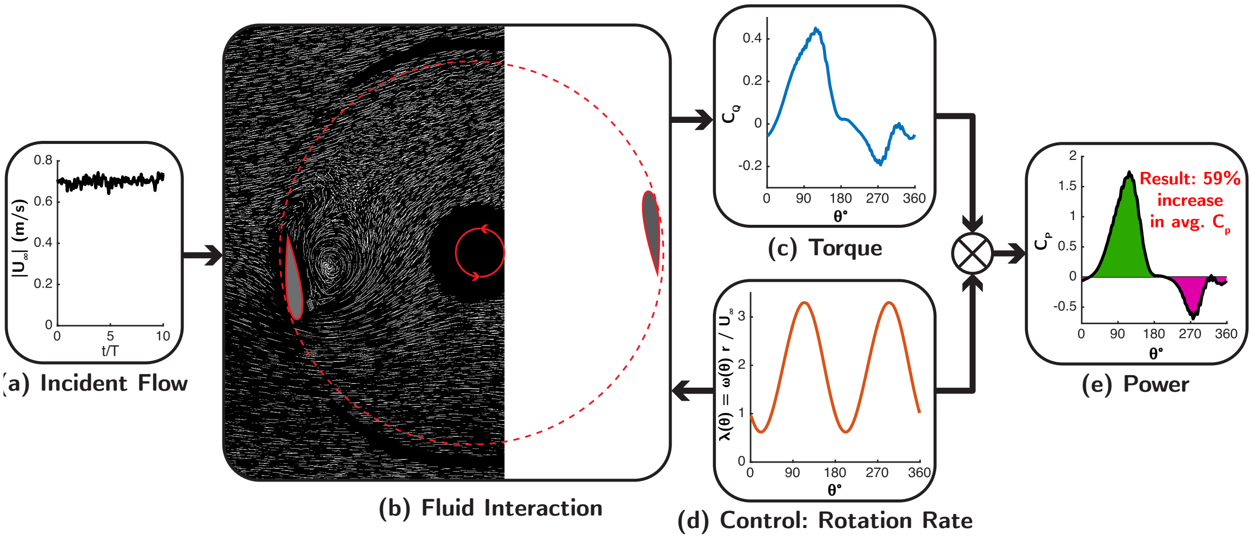

(a) Incident Flow

(b) Fluid Interaction

(c) Torque

(d) Control: Rotation Rate

(e) Power

Figure 5.2: Control Scheme Overview. An illustration of the interdependence of the control kinematics (angular velocity), the fluid structure interaction, forcing, and resulting power output. **(a)**, Freestream velocity magnitude input to the turbine system, plotted versus time normalized by the turbine rotation period T. **(d)**, Turbine control actuation via the rotation rate as a function of the blade azimuthal position, presented in non-dimensional form as the tip-speed ratio. **(b)**, Interaction between the fluid and the turbine blades. This is affected by both the incident flow and the control actuation. Here, bubble streak flow visualization shows the roll-up of a leading edge vortex. The areas lacking streaks are due to diffraction from the edge of the lower turbine end plate. **(c)**, Torque produced by the turbine rotor as a result of the fluid-rotor interaction. Here torque produced by a single blade is presented in non-dimensional form as the torque coefficient, or $C_Q(\theta) = \tau(\theta)/\left(\frac{1}{2}\rho U_\infty^2 Ar\right)$. **(e)**, The power output, presented as the efficiency, Eq. 1.9, is the product of the torque output and the rotation rate. This means the timing of the controlled angular velocity profile not only affects the fluid forcing by changing the local flow structure, but also directly affects the power output. An effective angular velocity controller then both maximizes beneficial fluid structure interaction and aligns the highest angular velocity with the highest fluid torque. The torque used to calculate the instantaneous torque coefficient and efficiency (C_Q and C_P respectively) does not include the torque necessary to accelerate and decelerate the turbine. Due to the periodic nature of the accelerations, these torques do not contribute to the mean power output (see methods chapter).

5.1.2 Methods

The methods in this work reflected those described in the methods chapter. Experiments were performed in the UW Tyler flume. The experimental Reynolds number, based on the chord length and freestream velocity, was 31,000. The temperature of the water was maintained at 15°C.

The turbine was controlled using a servomotor and motor controller. The servomotor control system can absorb power from the turbine as a generator as well as add power to the turbine as a motor. For constant torque and angular velocity control, control actuation that maximized C_P was identified by incrementing the respective values (see Fig. 5.3 for the corresponding performance curves). Values for A_i and ϕ_i that maximized C_P under intracycle angular velocity control in Eqs. (5.3) and (5.4) were selected by the Nelder-Mead downhill simplex method [139] with the RS + S9 improvements for stochastic objective functions given in [19]. The downhill simplex method was chosen due to the small number of required function evaluations as inspired for use in this type of problem by [130]. The control and optimization procedure, shown in Fig. 5.1, consisted of first evaluating the mean turbine performance at a given control parameter set, then incrementing the parameter set as required by the Nelder-Mead algorithm, and finally implementing the new parameter set. The optimizations were performed five times with randomized starting conditions to ensure that the solutions converged to a global maximum (see Fig. 5.4 for plots of the optimization process). For comparison, the optimized versions of the four control schemes (constant torque, constant, sinusoidal, and semi-arbitrary angular velocity) were each tested ten times, alternating control schemes for each test, thus reducing the risk of the influence of changes in test conditions.

5.1.3 Intracycle control performance and interpretation

The optimized intracycle angular velocity control profiles are found to produce a substantial increase in turbine efficiency, as compared to two standard control methods: constant torque

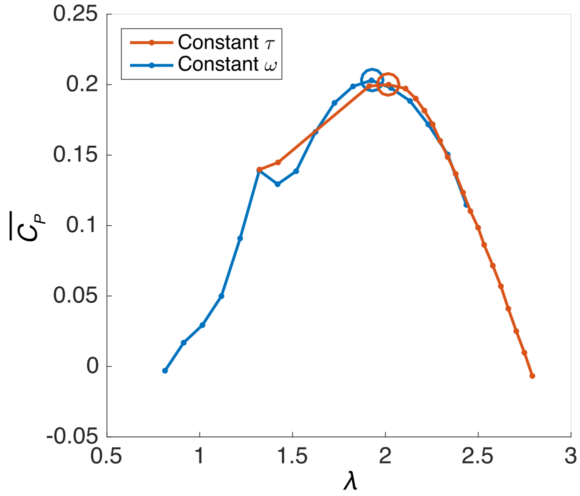

Figure 5.3: Performance curves of efficiency versus tip-speed ratio for the two-bladed experimental turbine under constant angular velocity (blue) and constant resistive torque (red) control. The performance curves vary slightly due to the differing kinematics: In constant torque control, the angular velocity oscillates slightly. In addition, the turbine is unable to operate at low tip-speed ratios under torque control (system stall occurs at the point of maximum torque). The peak efficiency points (circled dots) are used for comparison with intracycle angular velocity control.

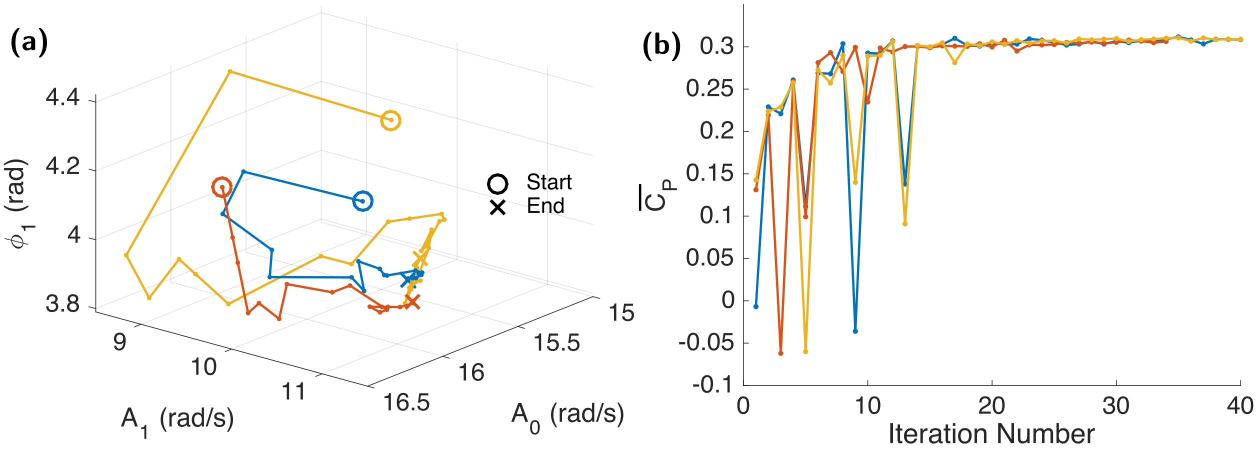

Figure 5.4: Sample Optimization Process. **(a)**, Trajectories of the centroid of the Nelder-Mead simplex for three optimizations of sinusoidal velocity control. Trajectories converge to a small region, but do not collapse to the same point. This may be a result of small variations in mean C_P between function evaluations. The final optimal parameter set is taken as the mean ultimate parameter sets from individual optimization trials.**(b)**, Efficiency as a function of iteration number during optimization.

Control Scheme	**Control Parameters**	$\langle C_P \rangle$	$\sigma(C_P)$[a]	**Gain**[b]
Constant τ	$\tau = 0.082$ N-m	**0.199**	0.005	
Constant ω	$\omega = 15.47$ rad/s	**0.203**	0.009	**0%**
Sinusoidal ω	$\omega = 15.58 + 10.58 \sin(2\theta + 3.96)$ rad/s	**0.311**	0.010	**53%**
Semi-arbitrary ω	$\omega = 16.43 + 10.56 \sin(2\theta + 3.83) +$ $0.02 \sin(4\theta + 1.02) +$ $2.63 \sin(6\theta + 1.32)$ rad/s	**0.321**	0.011	**59%**

[a] Standard deviation of C_P among turbine revolutions. At least $n = 500$ revolutions were sampled for each control scheme.

[b] Percent increase in $\overline{C_P}$ in comparison to constant angular velocity control

Table 5.1: Optimized Control Performance Comparison. The performance of optimized standard controllers, constant torque control and constant angular velocity control, is compared with optimized sinusoidal and semi-arbitrary intracycle angular velocity control. Optimum control parameters for the schemes tested, as well as their respective mean efficiencies ($\overline{C_P}$) are given. Mean efficiency is also calculated over each complete revolution of the turbine and the standard deviation of these efficiencies is reported as $\sigma(C_P)$. The semi-arbitrary and sinusoidal control schemes show a 59% and 53% increase in efficiency over the constant angular velocity controller respectively. Note that the mean efficiency values presented are identical whether the total or fluid torque is used due to the angular velocity periodicity (see methods section and Supplementary Table 1).

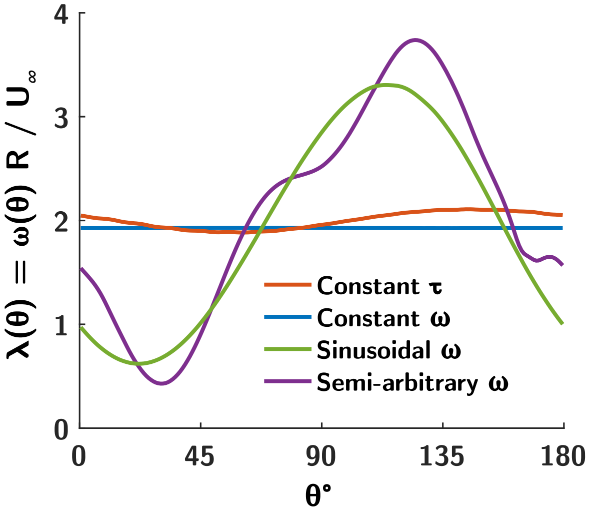

Figure 5.5: Phase-averaged variation in tip-speed ratio as a function of azimuthal blade position are given for the optimized control schemes described in Table 5.1. A half revolution is presented as the profiles are twice periodic over a single revolution of the two-bladed turbine.

and constant angular velocity control (see Supplementary Fig. 3 for performance as a function of average tip-speed ratio for these controllers). Relative to the constant velocity control case, which outperformed constant torque control, optimized sinusoidal and semi-arbitrary angular velocity control schemes yield a 53% and 59% increase in efficiency, respectively. Optimized control scheme parameters and their respective efficiencies are given in Table 5.1. The resulting tip-speed ratio profiles are shown in Fig. 5.5.

To investigate the mechanisms by which performance increases are realized, results from a single-bladed turbine under constant and sinusoidal angular velocity control schemes identical to those listed in Fig. 5.5 are compared. The semi-arbitrary control scheme is not investigated in this manner because it provides only a small increase in performance over the sinusoidal control scheme at the cost of much larger control torques and the more rapid acceleration of the added mass (the volume of fluid that is accelerated with the turbine blade), making the fluid torques more difficult to interpret. Further, a one-bladed turbine is used to isolate the fluid forcing on a single blade. The validity of a single-bladed turbine as a proxy for the individual blade forcing of a two-bladed turbine is shown in Fig. 5.6.

In Fig. 5.7, various measured and computed quantities of interest are shown as functions of turbine blade position. Values for a single-bladed turbine under constant and sinusoidal angular velocity control are compared. The figure is split into five zones. These zones are ranges of angular position corresponding regimes of operation. Zone 1 ranges from $\theta = 305^\circ$ to 42°, and thus wraps around both sides of the figure.

Figure 5.7b shows the angular $C_P(\theta)$ profiles for the constant and sinusoidal angular velocity schemes implemented on a single-bladed turbine. Also shown is the difference in efficiency between the sinusoidal and constant angular velocity control as a function of angular blade position. The net performance increase of the sinusoidal control over the constant angular velocity control is examined as a function of azimuthal blade position. The blade stroke is broken into zones (see Fig. 5.7a) based on the differences in performance of the two controllers (ΔC_P is the difference between C_P for sinusoidal and constant angular velocity control schemes).

For $\theta > 180^\circ$, the blade passes through a region disturbed by its upstream passage. Consequently, C_P is substantially reduced, even though the foil encounters favorable nominal angles of attack during both the upstream and downstream portions of the stroke. Further, in this region, the assumptions underpinning these nominal values (e.g. local velocity comparable to the freestream velocity) are violated and the nominal values provide only a qualitative description of the hydrodynamics. Throughout, it should be recalled that the constant rotation rate and sinusoidal profile employed on this single-bladed turbine were optimized for the two-bladed turbine and an optimization for a single-bladed turbine would likely converge to a different velocity profile.

Intracycle angular velocity control is successful for the following reasons: From the perspective of the nominal angle of attack, α_n, leading up to and during the power generation portion of the cycle ($\theta = 42^\circ$ to 180°), the foil under sinusoidal control executes a pitch-up

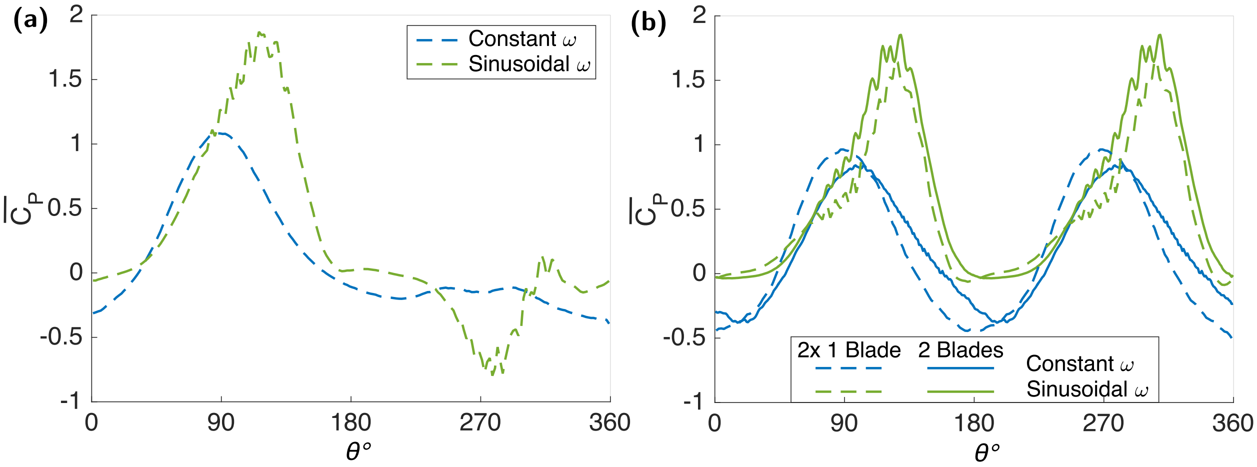

Figure 5.6: One-bladed turbine measurement validity. Two arguments are presented for the validity of examining the forcing on a single-bladed turbine as a proxy for the forcing on one blade of a two-blade turbine. **(a)** shows the efficiency as a function of blade position for a single-bladed turbine under constant and sinusoidal velocity control. We note that the majority of power is produced during the first half of the cycle, despite the fact that during some regions of the downstream sweep of the blade ($\theta > 180°$) the nominal angle of attack is favorable. This is likely because the extraction of energy from the flow during the upstream portion of the blade stroke leaves little energy to be extracted on the downstream portion of the stroke. For a two-bladed turbine, with twice the solidity of a single-bladed turbine, this is also expected to occur. Therefore, the forces imparted to the blade during the upstream portion of the stroke, where the flow is relatively undisturbed by previous blade passes, should be relatively unaffected by the reduction of the number of blades from two to one. **(b)** shows a comparison between the efficiency profiles for the two-bladed turbine and a reconstruction of the efficiency profiles for a two-bladed turbine using single-bladed turbine data. The reconstruction adds the single-bladed efficiency to itself offset by half a rotation as follows: $C_{p,\text{ 2x 1 Blade}} = C_{p,\text{ one blade}}(0° \rightarrow 360°) + C_{p,\text{ one blade}}(180° \rightarrow 360°, 0° \rightarrow 180°)$. As shown, good agreement is found between the reconstructed and actual efficiency profiles, with more phase error evident in the constant angular velocity control. In the future, individual blade instrumentation or flow field measurements near the blades may improve direct comparisons between control schemes.

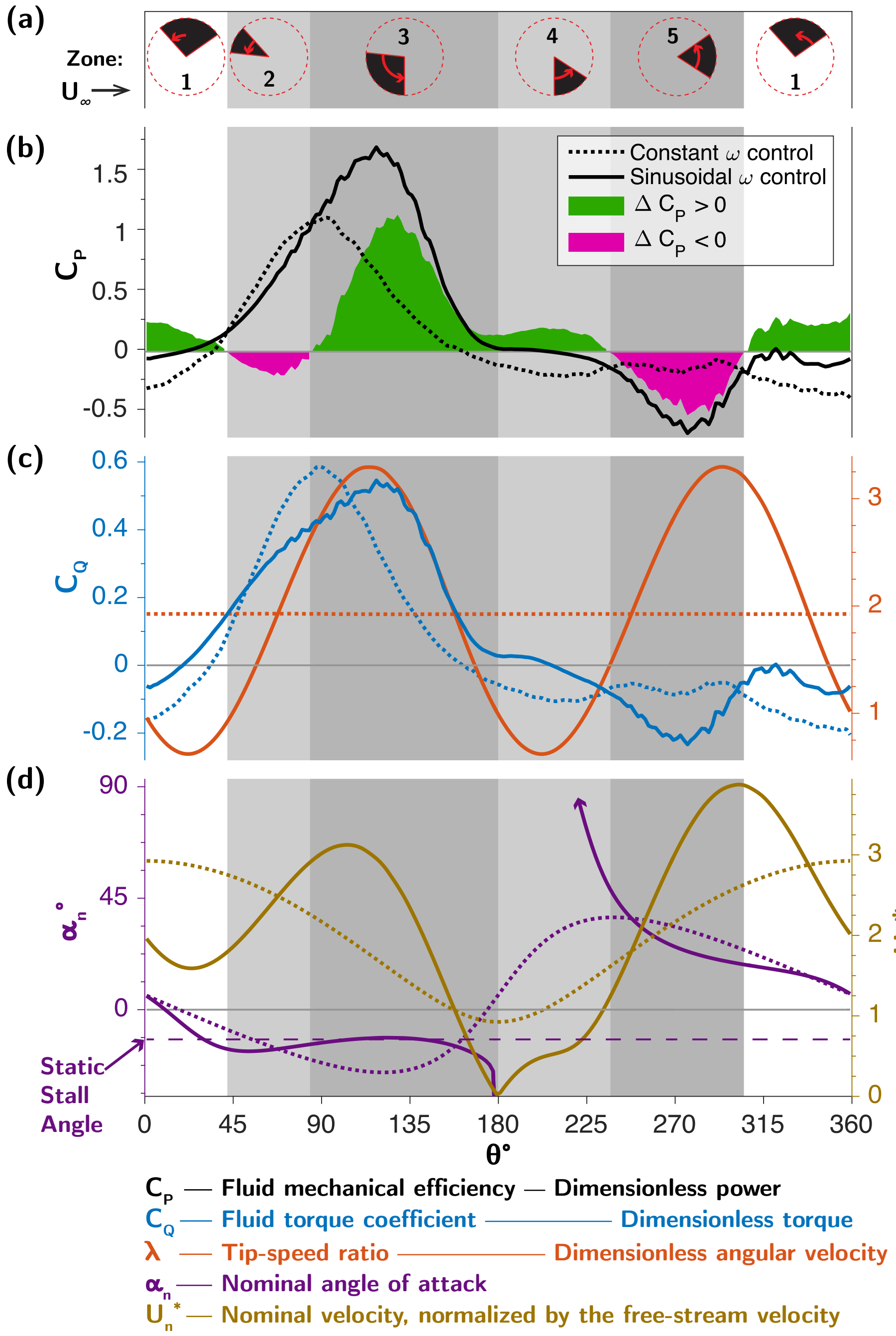

Figure 5.7: (Caption next page.)

Figure 5.7: (Previous page.) Per Zone Control Comparison. Efficiency, torque coefficient, and kinematics for a single-bladed turbine under constant and sinusoidal angular velocity control are compared. Throughout, a dotted line corresponds to constant angular velocity control and a solid line corresponds to sinusoidal angular velocity control. **(a)**, The turbine rotation is split into five zones based on azimuthal blade position. Circular segments indicate the angular blade sweep over the zone. Vertical shaded bands are provided as visual guides to distinguish the zones in panels b, c, and d. Zone 1 spans from $\theta = 305°$ to $42°$, and thus wraps around both sides of the plot. **(b)**, Phase-averaged instantaneous efficiency profiles as a function of azimuthal blade position for constant and sinusoidal angular velocity control schemes given in Table 5.1 are compared. The instantaneous difference in efficiency is illustrated, with green and magenta areas indicating that the sinusoidal controller is performing better or worse than the constant velocity controller, respectively. Panels **c** and **d** provide operational context for these differences. **(c)**, The torque coefficient, given by $C_Q = \tau/(\frac{1}{2}\rho U_\infty^2 A r)$, is given in blue. The tip-speed ratio profiles are given on the same plot in red. Because the freestream velocity is quasi-steady, this non-dimensionalizes the rotation rate, thus the constant velocity control tip-speed ratio is a horizontal line. **(d)**, The nominal angle of attack (purple) and the nominal freestream velocity (gold), which are calculated by Eqs. (1.3) and (1.6). The static stall angle for this foil, 12°, is given by the purple dashed line for reference. For sinusoidal control, the nominal angle of attack is greater than 90° during the first part of zone 4, as indicated by the arrow on the nominal angle of attack line. It should be noted, that because mean C_P is found by integrating over time, rather than θ, the sinusoidal control profiles are dilated or contracted, depending on the instantaneous rotation rate, but because this effect is small, it is more instructive to index performance to azimuthal blade position.

and hold maneuver to just over the static stall angle. In contrast, the foil under constant velocity control experiences a near constant increase in nominal angle of attack, to about twice the static stall angle. As a result, the peak torque under sinusoidal control is delayed, due to the delay or reduction of dynamic stall. This delay aligns the peak torque production with the peak in angular velocity (illustrated by the peak in λ, Fig. 5.7c). Thus power, as the product of these two quantities, is increased. Additionally, during the first part of this region (zones 2 and 3), the nominal freestream velocity, U_n^*, experienced by the foil under sinusoidal control increases, while under constant angular velocity control it steadily decreases. Increasing U_n^* may help delay separation or slow the dynamic stall process. Additional nominal freestream velocity also likely increases the magnitude of the lift force, and thus torque applied to the turbine rotor.

5.1.4 Performance by zone

Further nuances of the effect of kinematics on flow conditions and resulting power output are explored in each zone, as identified in Fig. 5.7a, in the following.

Zone 1 is defined as $\theta = 305° \rightarrow 42°$. Here, a single-bladed turbine under constant angular velocity control loses energy (it has a negative instantaneous efficiency), while the power produced by the sinusoidal angular velocity control scheme is near zero. The foil is translating almost directly up stream in this region. This means that little of the lift produced is projected onto the direction of turbine rotation and, consequently, drag is likely to dominate the blade forcing. Because the turbine under sinusoidal velocity control rotates more slowly than under constant velocity control, the nominal relative velocity, U_n^*, is reduced, consequently reducing drag in the direction of rotation. Another factor likely at play in this zone is the lower nominal angle of attack leading up to and beginning the zone for sinusoidal control, potentially resulting in a faster reattachment of flow after the large nominal angles of attack in zones 4 and 5. At the very end of zone 1 ($\theta = 20° \rightarrow 42°$), the nominal angle of attack increases faster under sinusoidal velocity control, thus resulting in larger lift forces and a larger torque coefficient.

Zone 2 is defined as $\theta = 42° \rightarrow 84°$. During this portion of the rotation, the constant angular velocity control outperforms the sinusoidal controller. This is partially a consequence of the delay in peak lift forces under sinusoidal control as discussed previously. Additionally, during the first part of zone 2, where the torque coefficients are similar, the rotation rate under sinusoidal control is lower, resulting in less power for the same torque applied to the rotor.

Zone 3 is defined as $\theta = 84° \rightarrow 180°$. The majority of energy harvesting by the foils occurs in this region due to the favorable angle of attack. In the case of constant velocity control, some of these forces are undoubtably a result of dynamic stall, wherein during an increase in the nominal angle of attack past the static stall angle, boundary layer separation occurs. This process is associated with a large increase in lift, followed shortly by a large increase in drag. The increase in drag likely explains the precipitous drop in rotor torque under constant velocity control at the beginning of this zone. Since the static stall angle of this foil is around 12° at these Reynolds numbers [72] and the nominal angle of attack during zone 2 reaches 17°, dynamic stall likely also plays a role in the forcing under sinusoidal control. It is possible that a small leading edge vortex forms, but the decrease in nominal angle of attack and increase in nominal freestream velocity at the beginning of zone 3 act to stabilize this vortex for a time. This would help maintain lift longer and delay the increase in drag until later in the stroke, resulting in the alignment of peak torque and peak rotation rate we observe.

Zone 4 is defined as $\theta = 180° \rightarrow 237°$. Throughout this region, the efficiency of the sinusoidal scheme is usually positive, while the constant control scheme is consistently negative. Here the foil is translating directly downstream, and large nominal angles of attack (likely resulting in fully separated flow) and small nominal freestream velocities result in no power extraction. Under sinusoidal control, the nominal angle of attack is greater than 90° for most of this zone, meaning the local flow direction is from behind the foil. This, combined with the fact that the rotation rate is slow (low λ), reduces power loss. Under constant velocity control the control system is forced to push the foil faster than the local flow at unfavorably large angles of attack resulting in a loss of power.

Zone 5 is defined as $\theta = 237^\circ \rightarrow 305^\circ$. In this zone, both control schemes suffer from a negative efficiency. Several factor likely contribute. First, here the blade is directly downstream of the main power producing regions, zones two and three, and as a result the streamwise velocity is diminished. Second, the nominal angle of attack is too high for lift production, as a result of the abrupt increase during zone four. The sinusoidal angular velocity control has a lower efficiency in this zone due to the same mechanism as the power increase in zone three. The slightly negative torque is multiplied by a higher angular velocity to yield a more negative mechanical power.

5.1.5 Discussion

Though there is a complex interconnection between changes in the turbine kinematics, fluid forcing, and the resulting power output (see Fig. 5.2), the primary success of intracycle angular velocity control is derived from aligning maximum velocity with maximum torque generation. This may be analogous to other unsteady fluid control problems, such as a bird's perching maneuver. Additional benefits are accrued by minimizing velocity when the turbine dynamics are dominated by drag and by modifying the dynamic stall process.

The control scheme introduced here substantially increases turbine performance without actuators, control surfaces, or increasing the degrees of freedom. However, within a single cycle, it is necessary to instantaneously supply the power required to accelerate the turbine and absorb the power required to decelerate the turbine. In the absence of a fluid and parasitic drive-train losses, the power required to accelerate and decelerate the turbine averages to zero over one rotation. The focus of this work is to isolate fluid power extracted (i.e., mechanical turbine power), which is standard for energy harvesting studies. This does not account for bearing friction or electrical inefficiencies, both of which reduce "water-to-wire" efficiency and may be minimized through judicious design. Although there is a reactive power requirement to accelerate the turbine, this power is recovered during deceleration, and there is net power extracted due to the unsteady fluid forcing. This has analogues to reactive power requirements for some wave energy conversion devices [63]. Here, enabling the wave converter to strategically inject energy back into the wave field can increase absorption efficiency over a much broader range of operating conditions [21].

For intracycle control of a single turbine, the electrical grid may be used as the source and sink for the reactive power requirement. Commercial CFT electrical systems are not designed to provide the cyclic power input required for angular acceleration under this control scheme. Additionally, precise rotor position measurements are not typically available. However, if a position encoder is incorporated, a commercial generator and back-to-back inverters can implement this scheme [41]. A prototype of this control and generation system for deployment on a turbine with cross-section of 1.0 m^2 has been assembled and will be tested in the near future. For multiple devices, average power output may be smoothed by electrically coupling the array and operating turbines out of phase. Regardless of electrical connection, any turbine would require a larger generator unit for intracycle control to supply the required control torques and momentary injection of power will reduce balance of system efficiency [41]. Both the reactive power, generator size requirements, and electrical efficiency penalties may be substantially reduced by mechanical coupling two turbines operating out of phase. In this concept, a single generator rotating at a constant speed could drive two turbines connected via non-circular gears, aligned out of phase such that the acceleration of one turbine occurs as the other is decelerating. Thus rotational kinetic energy would be transferred back and forth between the two rotors, in a manner analogous to a spring, thereby reducing or eliminating the need for reactive power. A prototype of a two-rotor system coupled via non-circular gears is shown in Appendix A.3.

Testing this control method at larger scale is a desirable and necessary next step. In this experiment, the blockage ratio was 11% and the freestream and chord-based Reynolds number was 31,000. The primary mechanism for the success of this control scheme, the alignment of maximum rotation rate with periods of maximum fluid torque, is likely to be robust to changes in blockage and Reynolds number. Though the timing and nature of fluid forcing may change with Reynolds number or blockage, the fact that the angle of attack must pass through zero twice per revolution guarantees that favorable lift will be limited to certain portions of the rotation, which is the necessary condition for success of this control mechanism. Similarly, a higher blockage ratio generally forces more fluid through the rotor than the unconfined case. Though this boosts mean power output, blockage is unlikely to influence the unsteady effects from which this control scheme derives its success. The reported absolute efficiencies may be elevated slightly from unconfined flow conditions at the test scale, but as all cases were tested at the same blockage, the relative efficiency increases are likely robust.

In addition to further exploration of the practical implementation of intracycle control, future work should investigate refinements to the control optimization process. For example, additional terms in the definition of the angular velocity profile could allow the profile to approach a truly arbitrary waveform. Further, variable angular velocity profile parameters could be optimized with objectives other than maximizing turbine efficiency. For instance, the optimization objective could seek a maximum C_P constrained by peak thrust or structural loads. Additionally, on-line optimization could be run continuously on a turbine, allowing it to adapt to inflow conditions that vary over time scales longer than a few minutes. This concept could be applied to optimization of arrays to further enhance array performance based on the bio-inspired gains suggested by [202]. Future work should also include measurement of the flow field near the turbine blades to further explore the fluid dynamics responsible for the success of this control scheme. Finally, for the purposes of employing this control scheme on existing CFT systems, experiments limiting the generator torque to resist the rotor rotation will be explored.

Historical experience with larger-scale CFTs show that efficiency with a constant velocity or torque controller is optimized for systems with a small number of blades (2-3) that have a small chord compared to the radius [201, 45]. These slender blades are prone to vibration and susceptible to damage from impact. In addition, these turbines operate at a higher tip-speed ratio [201], which produces more noise, increases susceptibility to cavitation, and may pose an elevated risk of collision for avian and aquatic species. In this study, we have demonstrated that it is possible to achieve comparable efficiencies with a relatively high chord-to-radius ratio and relatively low rotational velocity. In parallel to refinements in turbine geometry, future optimization should explore the benefits of dynamic control to exploit unsteady fluid forces, as inspired by bio-propulsion, to realize transformative gains in efficiency for unconventional turbines.

5.2 A Two Turbine Array: Geometric and Control Optimization

The coordinated control concept and preliminary results were published here[183]. The expanded and refined data set presented here has yet to be published.

As mentioned previously, it has been shown that CFTs can be more densely-packed in an array than HAWTs, resulting in significantly increased power output per-unit-land-area [49]. However, comprehensive CFT array optimization has not been undertaken, partially due to the previously described difficulties in simulating CFT fluid dynamics. This study has two objectives. The first is to perform the first experimental combined geometric and control optimization on a two-rotor array using standard control methods. The second is to introduce a new control concept for closely-spaced CFTs. By controlling both turbine rotors via a parent controller (Fig. 5.8), this scheme attempts to minimize the negative impact of the coherent structures described in chapter 4 on closely positioned downstream turbines. More optimistically, we hope to take advantage of the circulation of these structures to boost the performance down-stream turbines. Specifically, the turbines are controlled to ensure a constant angular phase difference between the turbine blade positions. This allows periodic flow structures to be intercepted in a repeatable manner. We term this concept *coordinated control*.

Closely spacing cross-flow turbines for increased energy density per unit land or seafloor area has many potential benefits. First, the potential for environmental or stakeholder conflicts and the cost electrical cabling is reduced. In both wind and hydrokinetic applications, regions of economically viable resource intensity (high flow speeds) are often highly localized. Dense CFT arrays could maximize the power output from these areas. In some

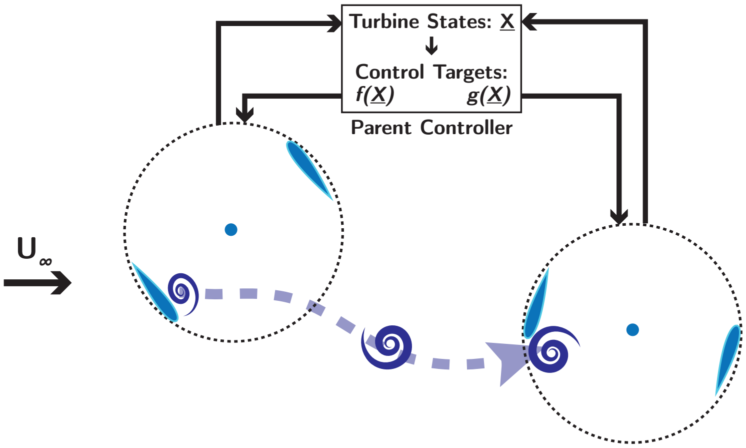

Figure 5.8: Illustration of the coordinated control concept.

deployments, array area may be constrained by other factors, such as on the roof tops of buildings, in mountain passes, and in narrow tidal channels. In the latter case, high density arrays may be used to increase the array blockage ratio of a channels. A high blockage ratio array may increase efficiency by harnessing the potential energy in addition to the kinetic energy in the flow [160]. Finally, high-density arrays may reduce the land-lease costs of wind energy. Currently, lease costs account for 20% of wind farm operations and maintenance expenses [133].

Prior Work

The research group of Dr. John Dabiri has performed CFT array tests in the field [48, 101] and on a two-turbine array in the laboratory [32]. The field experiments demonstrated an approximately eight-fold increase in energy density per unit area compared to traditional AFT wind farms. Additional wind-tunnel tests where performed by [3] and a number of groups have performed CFD simulations [56, 30, 57, 44]. A common theme of results is an increase in power output above that of isolated turbine performance for certain array geometric configurations, namely when the rotors are side-by-side when facing the flow.

Though [44] did so computationally, this is the first experimental optimization of both turbine control and array geometry. Additionally, this appears to be the first demonstration of the coordinated control concept.

5.2.1 Methods

Thes tests were performed in the Bamfield Marine Science Centre flume, as described in the methods chapter. During these tests, on turbine was fixed in space and used the setup described in the Methods chapter. The other turbine was cantilevered from a Velmex BiSlide robotic gantry system, allowing precision control of the rotor position in the streamwise and cross-streamwise directions. To perform accurate performance measurements, this turbine was mounted to the face of a Professional Instruments Company Block-Head air bearing. The air bearing allowed essentially frictionless rotation of the turbine rotor, while resisting the thrust and lateral fluid loading. The motion was driven by a Yaskawa SGMCS-02B3C41 servomotor. The reaction torque of this servomotor was measured by a Futek F400 torque cell.

The flow speed was 0.55 m/s and the temperature was held at $32^\circ \pm 0.5^\circ$ C, resulting in a diameter-based Reynolds number of $Re_D = 123,000$. The two turbine rotors used in the array were identical to the standard turbine of the methods section, except that instead of circular end-plates, foils were mounted via NACA0008 struts, as described in 3.2. The blockage ratio of the array in the test section ranged from 2.8% (turbines in-line) to 5.6% (turbines side-by-side).

The test matrix of relative rotor positions sampled is given in Fig. 5.9. Arranged on a polar grid, positions ranged from side-by-side ($x = 0$) to $x = 3.61D$ in the streamwise direction, and a maximum spacing of $1.83D$ in the cross-stream direction. The minimum distance between rotor centers was $2.1D$.

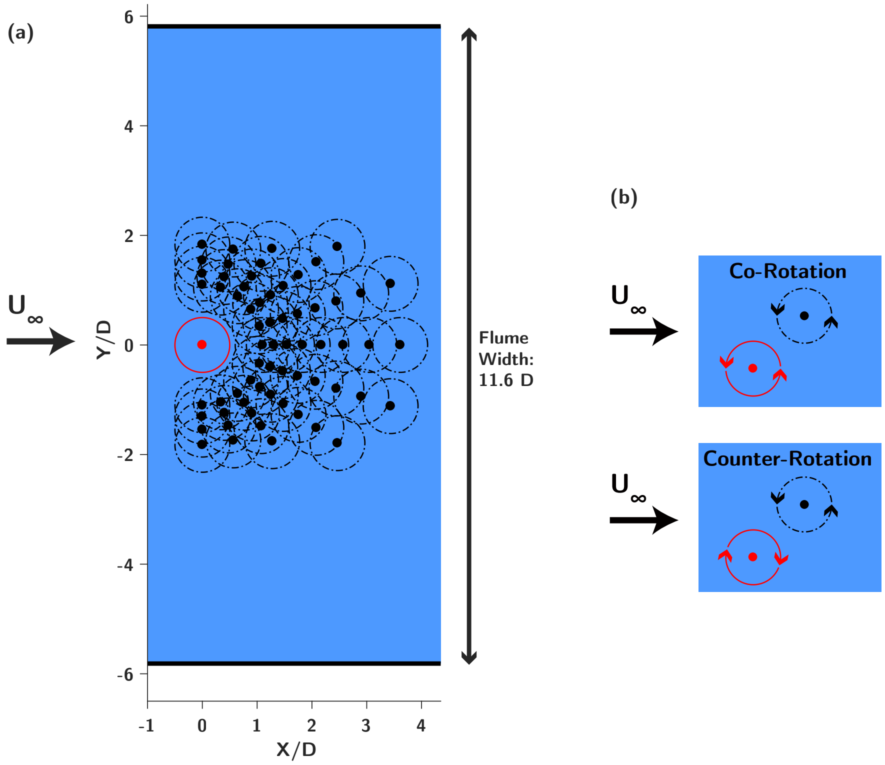

Figure 5.9: **(a)** Relative test positions in the flume section, fixed turbine in red. **(b)** Definition of co- and counter-rotation cases.

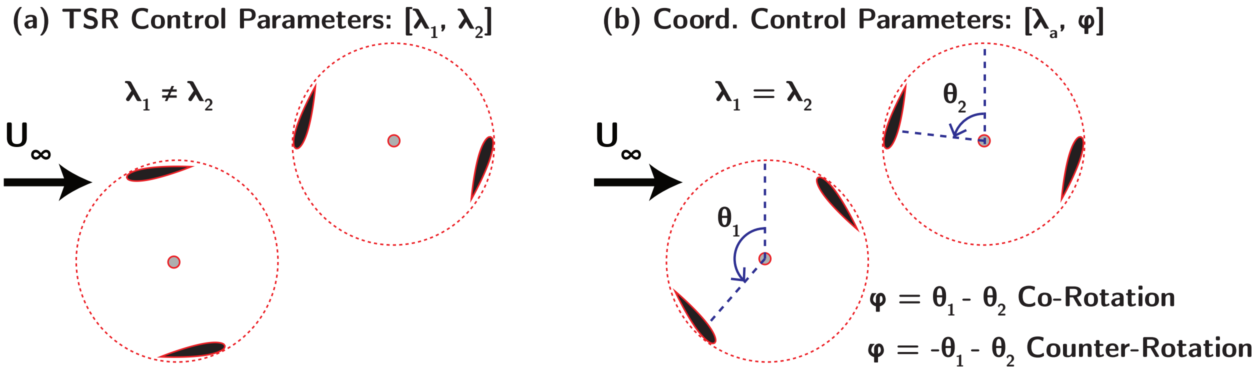
(a) TSR Control Parameters: $[\lambda_1, \lambda_2]$

(b) Coord. Control Parameters: $[\lambda_a, \varphi]$

Figure 5.10: **(a)** TSR control. **(b)** Coordinated control.

Turbine Control

At each of the locations illustrated in Fig. 5.9, two types of control were optimized for maximum array power output. Additionally, each control type was optimized at each position for co- and counter-rotating rotors. In the first control type, here referred to as *TSR control*, the rotation rate of each rotor was optimized simultaneously (two-parameter optimization of $[\lambda_1, \lambda_2]$), assuming the freestream velocity is nominally constant) to produce maximum array power. The objective of this control scheme is to optimize rotor operation in the mean flow field induced by the rotors. This is a non-trivial optimization problem as there is a co-dependence between turbine rotation rates, the resulting flow field, and the array power output. In the second control scheme, *coordinated control*, the angular velocities, or nominal tip-speed ratios of the of the two turbines are locked to the same value ($\lambda_a = \lambda_1, \lambda_2$) and the angular blade offset, or phase difference ($\phi = \theta_1 - \theta_2$), between the two rotors was controlled. This resulted in another two-parameter optimization of $[\lambda_a, \phi]$. A closed-loop controller was used to ensure a constant ϕ while testing a control instance. Figure 5.10 illustrates these two control schemes.

Optimization of the control parameter sets was performed using the Nelder-Mead algorithm described in section 5.1. To speed optimization convergence, initial simplex values were chosen in part based on data already collected. The first simplex point was the optimum control set point found for any downstream rotor position so far. The second point was the optimum control set point for downstream rotor positions within $1D$ of the current position if that control set point was suitably different from the first simplex point. If not, a psuedo-random second simplex was chosen, ensuring sufficient distance in parameter space. The third simplex point was always psuedo-random, but with a lower bound set on the initial simplex volume. Optimization was halted if (a) the simplex reached a minimum volume or (b) 30 control set points had been tested since the last improvement on array performance.

Performance Metric

The two turbine rotors and setups were tested separately, in isolation. Their individual peak performances are denoted by $C^*_{P,1}$ and $C^*_{P,2}$, where an asterisk denotes performance at the optimized tip-speed ratio. The performance of the array is evaluated on how much more normalized power is produced by the two turbines interacting than the sum of their power produced in isolation. The normalized sum of the peak power produced in isolation is

$$C^*_P = \frac{C^*_{P,1} + C^*_{P,2}}{2}, \tag{5.5}$$

If inflow conditions are identical, this is equivalent to the sum of the power produced by both turbines in isolation, divided by the kinetic energy incident on two turbine projected areas. The array performance metric, using the mean power produced in isolation as the normalizing factor, is then

$$C_{P,N} = \frac{\frac{1}{2}\left(C_{P,1} + C_{P,2}\right)}{\langle C^*_P \rangle} = \frac{C_{P,1} + C_{P,2}}{C^*_{P,1} + C^*_{P,2}}. \tag{5.6}$$

If inflow conditions were identical across all tests, this is equivalent to the power produced by the turbines in the array divided by the power produced by the turbines in isolation. However, measurements must be normalized in order to account for small fluctuations in the free stream velocity, leading to differences in the fluid power available during the test.

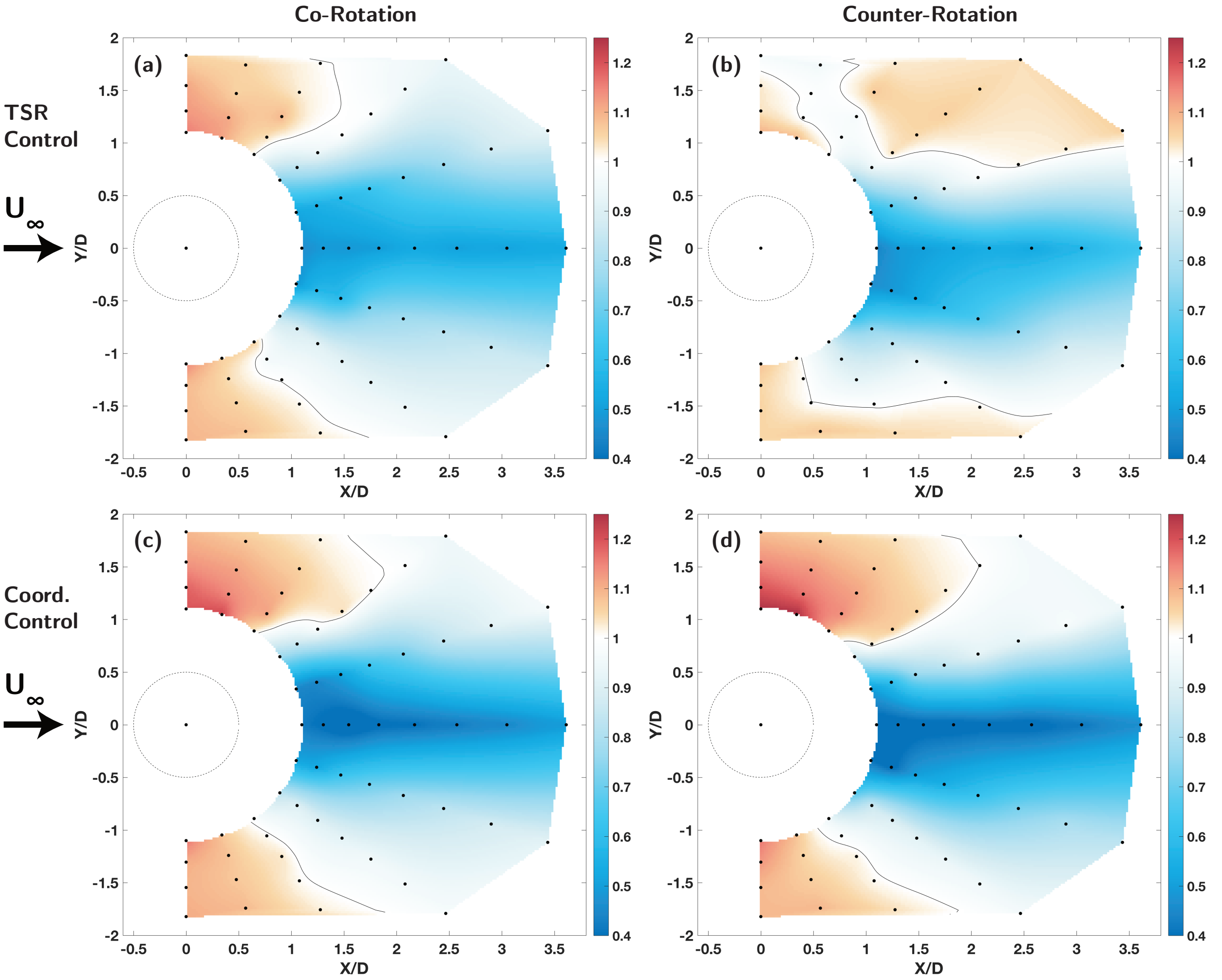

Figure 5.11: Color indicates optimized array performance (Eq. 5.6) at each relative rotor position. The contour line outlines regions where the array is outperforming equivalent isolated turbines. **(a)** TSR control, co-rotation. **(b)** TSR control, counter-rotation. **(c)** Coordinated control, co-rotation. **(d)** Coordinated control, counter-rotation.

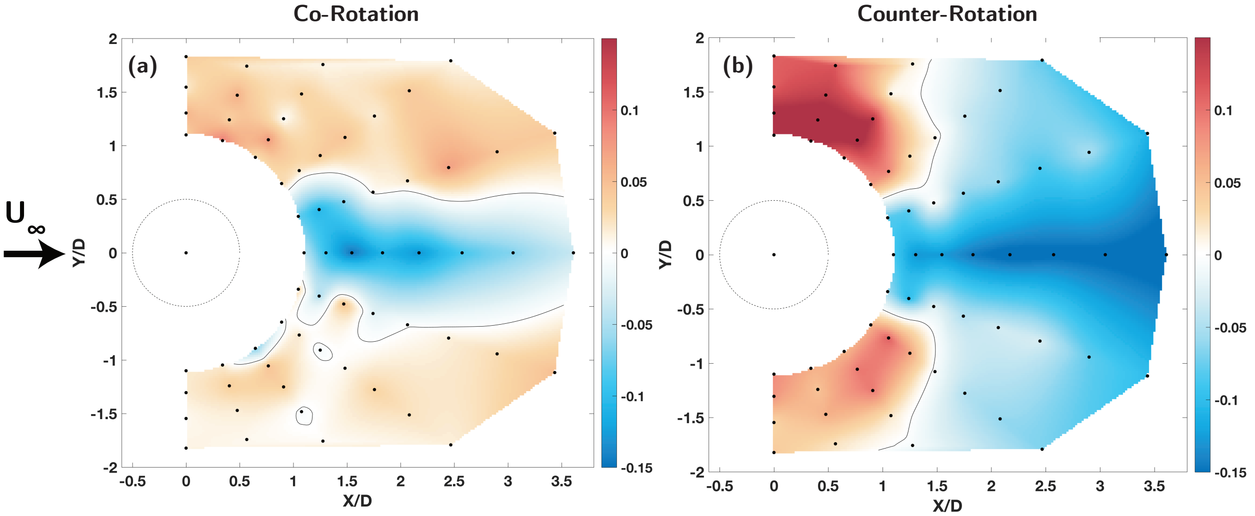

Figure 5.12: Color indicates optimized array performance of the coordinated controls strategy minus the optimized performance of TSR control. Red indicates coordinated control outperforms TSR control at that location **(a)** Co-rotation. **(b)** Counter-rotation.

5.2.2 Results and Discussion

The optimized array performance for each control scheme as a function of downstream turbine position is show in Fig. 5.11. Notably, for large regions to either side of the upstream rotor, the array outperforms equivalent isolated turbines for all control types and rotations. The largest increase in performance of 1.3x occurs using the coordinated control scheme and counter-rotating turbines.

As shown in the wake analysis chapter, there are bypass flow regions to either side of a CFT with flow faster than the freestream velocity. Here, more energy is incident on the downstream rotor. However, turbine rotors apply resistance to the flow, which mean there is some degree of deceleration of the flow velocity as it approaches the rotor from upstream (streamwise induction). This means that a downstream rotor has the potential decrease the performance of an upstream rotor. Apparent from this dataset is that this does not occur to a significant degree when the downstream rotor is offset to the side of the upstream one.

Figure 5.12 shows the difference in performance between coordinated and TSR control. Coordinated control suffers when the rotors are in-line, as holding the rotation rates equal cause the local velocity-based TSR of the downstream rotor to be far higher than optimal. When the downstream rotor is to the sides of the upstream rotor, coordinated control outperforms TSR control, particularly for the counter-rotating case.

Figure 5.13 examines the array performance as a function of phase offset (blade position difference) under coordinated control for three positions where coordinated control outperforms TSR control. A boost of between 1.025x and 1.04x in performance is observed by implementing coordinated control versus not controlling for phase offset.

5.2.3 Conclusions

Experimental control control and array geometry optimization was performed for two CFTs. Control optimization was performed on an array power output, rather than an individual output basis. Two control types were explored. In the first, the rotation rates of the turbines were allowed to differ. In the second, they were held equal, and the phase difference between the blade positions was also optimized. Termed coordinated control, we showed that this new control strategy is capable of boosting array power to 1.3 times that of two isolated turbines. The mechanism for power increase is likely a combination of direction of faster bypass flow into neighboring rotors and proper phase alignment of the rotors. The phase alignment appears to minimize mutual disturbances between the rotors in the array.

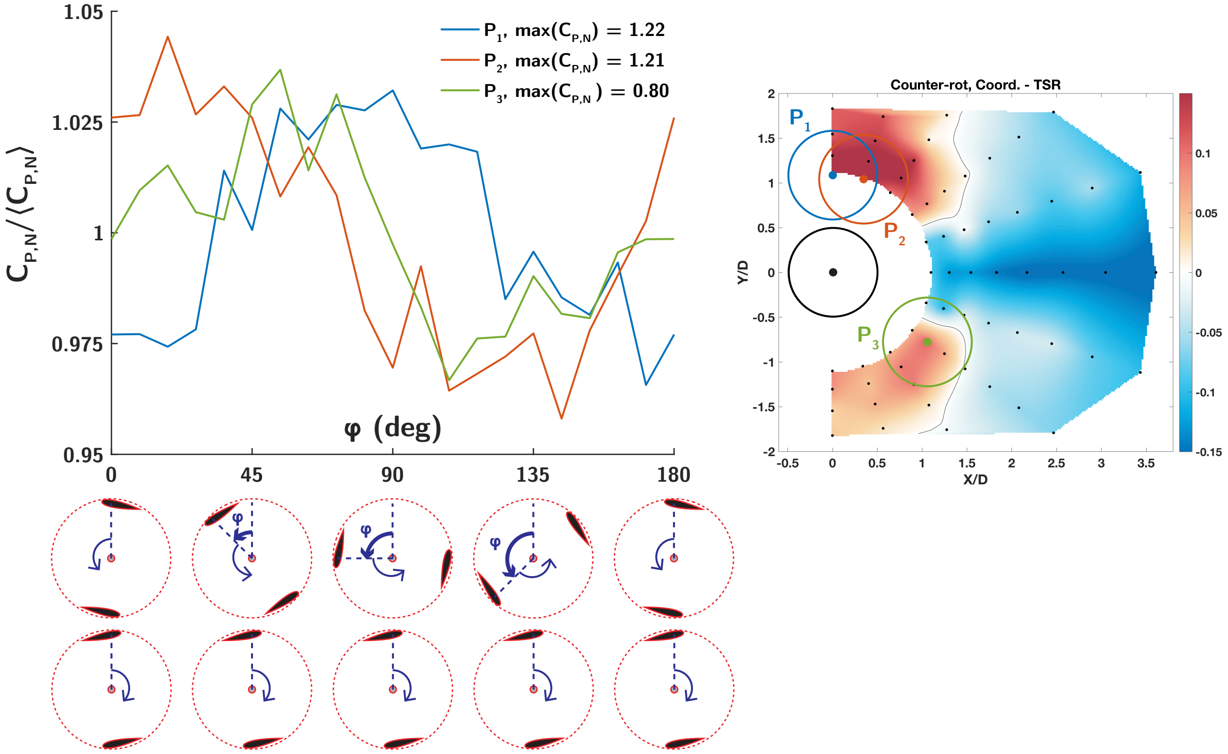

Figure 5.13: Plot of sensitivity of performance to changes in phase under coordinated control. Three relative rotor positions for counter-rotating coordinated control are shown. Array performance is normalized by the mean performance across all rotor position phase differences (ϕ). Values above or below 1.0 indicate a benefit or detriment in performance due to coordinated control operation compared to randomized values of ϕ (uncoordinated control with both rotors at the same rotation rate).

Chapter 6

CONCLUSIONS AND OUTLOOK

6.1 Conclusions: Geometry

Blade mounting structure geometry, preset pitch angle, and the effect of Reynolds number on optimal preset pitch angle, coord-to-radius ratio, and number of blades are examined in this chapter. Mounting the blades via thin foil struts at the blade ends results in the most efficient rotor. Mounting blades with a single strut at the mid-span decreases performance through tip losses and also some unknown mechanism, possibly related to span-wise flow on the blade. Analytical models for the drag losses of different strut geometries are presented. Turbine performance is shown to be very sensitive to changes in preset pitch angle. Between zero an the optimum of six degrees, performance increased by 24% and 59% for two- and four-bladed turbines respectively. Results indicate that a critical maximum nominal angle of attack may help to explain the location of CFT performance curve peaks. A low-TSR secondary peak is shown through bubble visualization to correspond to a matching between the translation speed of the blade on the retreating side of the rotor and the downstream advection speed of a leading edge vortex. The work on optimal geometry scaling with Reynolds number showed that the optimal chord-to-radius ratio decreases with Reynolds number. Optimal preset pitch angle grows as chord-to-radius ratio is increased. TSR of peak performance decreases with increased chord-to-radius ratio. Solidity is shown to be a poor descriptor of the influence of geometric changes on turbine performance.

6.2 Conclusions: Wake Analysis

Wake of a high chord-to-radius turbine is measured on the mid-span plane using stereo particle-image velocimetry. The mean wake is similar to prior work, despite the unique turbine geometry. A new method of extracting and ranking oscillatory modes using the optimal dynamic mode decomposition is introduced and shown to outperform other methods based on error and energy capture. This technique reveals dual structures on the advancing and retreating sides of the wake oscillating at the blade-pass frequency. The advancing-side structure is vortex roll-up due to the strong shear layer, triggered by the blade pass. The retreating-side structure is shed circulation due to lift generation, likely a trailing-edge vortex. The optDMD method also shows a transition towards lower-frequency oscillation on the advancing side, perhaps indicating a transition to a bluff-body type oscillation in the far wake. The unusual structure, consisting of vortex surrounded by a ring of vorticity of the same sign, is described and shown to be associated with significant axial velocity. The time-resolved trajectory of this vortex core is tracked and the statistical distribution of the path is determined. The cycle-to-cycle repeatability of the vortex core position rapidly decreases after about one diameter downstream.

6.3 Conclusions: Advanced Control

Variation of the angular velocity of a CFT rotor is shown, like variable pitch control, to alter the local angle of attack. This method requires no additional mechanisms and also allows for control over the local flow velocity magnitude. Sinusoidal and three-term Fourier series angular velocity profiles are optimized to maximize cycle-averaged power output. The optimized waveforms increase mean turbine power output by as much as 59%, compared to the typical control strategies of constant torque and constant velocity control. The success of this method is attributed to optimization of the blade kinematics during the dynamic stall process and an alignment of regions of high torque production with high angular velocity.

An array of two turbines is explored by altering the relative positions of the rotors and by simultaneous optimization of the rotor control. Two control strategies are optimized. In the first, the angular velocity of each turbine is optimized to maximize the array power output. In the second, the angular velocity of the two turbines is locked to the same value. This angular velocity, as well as the blade position phase offset of the rotors is optimized.

This scheme is termed coordinated control. Both control schemes yield power output greater than two isolated turbines, primarily in configurations where the rotors are side-by-side. A maximum of a 30% increase over isolated turbines is observed for coordinated control. The majority of the power increase appears to be due to location of the rotors in each others accelerated bypass flow, though examination of performance as a function of blade position offset during coordinated control shows some benefit of phase-locking.

6.4 Future Directions

One of the major short-comings of this work is that on-blade flow measurements were never taken to directly analyze the mechanisms by which control or geometry changes effect performance. Not only could the explanations of the mechanisms presented here be strengthened, but it is probable that on-blade flow information will result in inspiration for further improvements in CFT performance.

A large question remaining is the role of flow three-dimensionality in the operation of CFTs. Both the blade mounting structure study and the wake analysis indicate that axial (vertical) flow plays an important role within the rotor. However, no other studies to date have suggested this, and certainly no study has explicitly examined axial flow within a rotor.

The remarkably power increase resulting from optimized variable angular velocity control comes at the expense of large power fluxes to and from the generator. A more economically realistic approach would be to approach this control type from the perspective of selectively extracting power from the rotor based on the blade position, rather than strict velocity control. Under this method, power could be restricted to flow from the rotor to the generator, and the maximum generator current could be regulated, paving the way for an economical implementation of this approach.

Translating laboratory results to larger turbines is difficult due to the effects illustrated in the Reynolds number scaling section. A simple improvement could be to trip the blade boundary layer from laminar to turbulent as near the leading edge as possible. The success of this approach could be evaluated by comparing to the higher Reynolds number data collected in the scaling work.

The interdependence of control, operating conditions, and rotor geometry make optimization of cross-flow turbine performance a difficult non-linear and high-dimensional task. In the end, understanding how each parameter effect turbine performance and loads may be more useful than global optimization. This is because other constraints, such as economics or structural concerns may force CFT designers to select configurations that are off-optimal in some respects. Understanding how these choices effect performance would be valuable information for those performing techno-economic optimization. For example, in the blade mounting structures section, it was determined that free blade tips are very detrimental to performance. However, adding to the turbine rotor height without additional blade mounting arms could add power output while incurring minimal additional cost. A more thorough understanding of tip-loss trends in CFTs would be necessary to perform this evaluation.

BIBLIOGRAPHY

[1] Ira Herbert Abbott and Albert Edward Von Doenhoff. *Theory of wing sections, including a summary of airfoil data.* Courier Corporation, 1959.

[2] U.S. Energy Information Agency. Electric power annual. Technical report, U.S. Department of Energy, 2017.

[3] Mojtaba Ahmadi-Baloutaki, Rupp Carriveau, and David SK Ting. A wind tunnel study on the aerodynamic interaction of vertical axis wind turbines in array configurations. *Renewable Energy*, 96:904–913, 2016.

[4] Joao Vicente Akwa, Horacio Antonio Vielmo, and Adriane Prisco Petry. A review on the performance of savonius wind turbines. *Renewable and sustainable energy reviews*, 16(5):3054–3064, 2012.

[5] Daniel B Araya, Tim Colonius, and John O Dabiri. Transition to bluff-body dynamics in the wake of vertical-axis wind turbines. *Journal of Fluid Mechanics*, 813:346–381, 2017.

[6] Daniel B Araya and John O Dabiri. A comparison of wake measurements in motor-driven and flow-driven turbine experiments. *Experiments in Fluids*, 56(7):150, 2015.

[7] MA Ashraf, J Young, JC S. Lai, and MF Platzer. Numerical analysis of an oscillating-wing wind and hydropower generator. *AIAA journal*, 49(7):1374–1386, 2011.

[8] Thomas D Ashwill. *Measured data for the Sandia 34-meter vertical axis wind turbine.* Sandia National Laboratories Albuquerque, NM, 1992.

[9] Travis Askham and J Nathan Kutz. Variable projection methods for an optimized dynamic mode decomposition. *SIAM Journal on Applied Dynamical Systems*, 17(1):380–416, 2018.

[10] Nadine Aubry, Philip Holmes, John L Lumley, and Emily Stone. The dynamics of coherent structures in the wall region of a turbulent boundary layer. *Journal of Fluid Mechanics*, 192:115–173, 1988.

[11] P. Bachant. *Experimental investigation of helical cross-flow axis hydrokinetic turbines, including effects of waves and turbulence.* PhD thesis, University of New Hampshire, 2011.

[12] Peter Bachant and Martin Wosnik. Characterising the near-wake of a cross-flow turbine. *Journal of Turbulence*, 16(4):392–410, 2015.

[13] Peter Bachant and Martin Wosnik. Performance measurements of cylindrical-and spherical-helical cross-flow marine hydrokinetic turbines, with estimates of exergy efficiency. *Renewable Energy*, 74:318–325, 2015.

[14] Peter Bachant and Martin Wosnik. Effects of reynolds number on the energy conversion and near-wake dynamics of a high solidity vertical-axis cross-flow turbine. *Energies*, 9(2):73, 2016.

[15] Peter Bachant, Martin Wosnik, Budi Gunawan, and Vincent S Neary. Experimental study of a reference model vertical-axis cross-flow turbine. *PloS one*, 11(9):e0163799, 2016.

[16] Pawel Baj, Paul JK Bruce, and Oliver RH Buxton. The triple decomposition of a fluctuating velocity field in a multiscale flow. *Physics of Fluids*, 27(7):075104, 2015.

[17] Francesco Balduzzi, Alessandro Bianchini, Ennio Antonio Carnevale, Lorenzo Ferrari, and Sandro Magnani. Feasibility analysis of a Darrieus vertical-axis wind turbine installation in the rooftop of a building. *Applied Energy*, 97:921–929, 2012.

[18] Francesco Balduzzi, Alessandro Bianchini, Riccardo Maleci, Giovanni Ferrara, and Lorenzo Ferrari. Blade design criteria to compensate the flow curvature effects in h-darrieus wind turbines. *Journal of Turbomachinery*, 137(1):011006, 2015.

[19] Russell R Barton and John S Ivey Jr. Nelder-mead simplex modifications for simulation optimization. *Management Science*, 42(7):954–973, 1996.

[20] L Battisti, L Zanne, S DellâAnna, V Dossena, G Persico, and B Paradiso. Aerodynamic measurements on a vertical axis wind turbine in a large scale wind tunnel. *Journal of energy resources technology*, 133(3):031201, 2011.

[21] Scott J Beatty, Matthew Hall, Bradley J Buckham, Peter Wild, and Bryce Bocking. Experimental and numerical comparisons of self-reacting point absorber wave energy converters in regular waves. *Ocean Engineering*, 104:370–386, 2015.

[22] Gabriele Bedon, Stefano De Betta, and Ernesto Benini. Performance-optimized airfoil for darrieus wind turbines. *Renewable Energy*, 94:328–340, 2016.

[23] G Bergeles, A Michos, and N Athanassiadis. Velocity vector and turbulence in the symmetry plane of a darrieus wind generator. *Journal of Wind Engineering and Industrial Aerodynamics*, 37(1):87–101, 1991.

[24] Gal Berkooz, Philip Holmes, and John L Lumley. The proper orthogonal decomposition in the analysis of turbulent flows. *Annual review of fluid mechanics*, 25(1):539–575, 1993.

[25] J. Birch and M. Dickinson. Spanwise flow and the attachment of the leading-edge vortex on insect wings. *Nature*, 412:729–733, 2001.

[26] Ben F Blackwell, Robert E Sheldahl, and Louis V Feltz. Wind tunnel performance data for the darrieus wind turbine with naca 0012 blades. Technical report, Sandia Labs., Albuquerque, N. Mex.(USA), 1976.

[27] Radu Bogateanu, Alexandru Dumitriache, Horia Dumitriscu, and Stoica. Reynolds number efects on the aerodynamic performance of small vawts. *Scientific Bulletin, Universitatea Politehnica Bucuresti*, 2014.

[28] Michael Borg, Andrew Shires, and Maurizio Collu. Offshore floating vertical axis wind turbines, dynamics modelling state of the art. part i: Aerodynamics. *Renewable and Sustainable Energy Reviews*, 39:1214–1225, 2014.

[29] Matthieu Boudreau and Guy Dumas. Comparison of the wake recovery of the axial-flow and cross-flow turbine concepts. *Journal of Wind Engineering and Industrial Aerodynamics*, 165:137–152, 2017.

[30] J Bremseth and K Duraisamy. Computational analysis of vertical axis wind turbine arrays. *Theoretical and Computational Fluid Dynamics*, 30(5):387–401, 2016.

[31] G Brochier, P Fraunie, C Beguier, and I Paraschivoiu. Water channel experiments of dynamic stall on darrieus wind turbine blades. *Journal of Propulsion and Power*, 2(5):445–449, 1986.

[32] Ian D Brownstein, Matthias Kinzel, and John O Dabiri. Performance enhancement of downstream vertical-axis wind turbines. *Journal of Renewable and Sustainable Energy*, 8(5):053306, 2016.

[33] S. L. Brunton and J. N. Kutz. *Data-Driven Science and Engineering: Machine Learning, Dynamical Systems, and Control.* Cambridge University Press, 2018.

[34] S. L. Brunton and B. R. Noack. Closed-loop turbulence control: Progress and challenges. *Applied Mechanics Reviews*, 67:050801–1–050801–48, 2015.

[35] S. L. Brunton and C. W. Rowley. Fast computation of FTLE fields for unsteady flows: a comparison of methods. *Chaos*, 20:017503, 2010.

[36] Steven L Brunton, Clarence W Rowley, and David R Williams. Reduced-order unsteady aerodynamic models at low reynolds numbers. *Journal of Fluid Mechanics*, 724:203–233, 2013.

[37] Abel-John Buchner, MW Lohry, Luigi Martinelli, Julio Soria, and AJ Smits. Dynamic stall in vertical axis wind turbines: Comparing experiments and computations. *Journal of Wind Engineering and Industrial Aerodynamics*, 146:163–171, 2015.

[38] Abel-John Buchner, Julio Soria, Damon Honnery, and Alexander J Smits. Dynamic stall in vertical axis wind turbines: scaling and topological considerations. *Journal of Fluid Mechanics*, 841:746–766, 2018.

[39] Brian Cantwell and Donald Coles. An experimental study of entrainment and transport in the turbulent near wake of a circular cylinder. *Journal of fluid mechanics*, 136:321–374, 1983.

[40] Travis J Carrigan, Brian H Dennis, Zhen X Han, and Bo P Wang. Aerodynamic shape optimization of a vertical-axis wind turbine using differential evolution. *ISRN Renewable Energy*, 2012, 2012.

[41] Robert J. Cavagnaro, Benjamin Strom, Brian Polagye, and Andy Stewart. Power collection from multiple hydrokinetic generators utilizing advanced control. In *European Wave and Tidal Energy Conference*, 2017.

[42] Chein-Chang Chen and Cheng-Hsiung Kuo. Effects of pitch angle and blade camber on flow characteristics and performance of small-size darrieus vawt. *Journal of Visualization*, 16(1):65–74, 2013.

[43] K. K. Chen, T. Colonius, and K. Taira. The leading-edge vortex and quasisteady vortex shedding on an accelerating plate. *Physics of Fluids*, 22:033601, 2010.

[44] Wei-Hsin Chen, Ching-Ying Chen, Chun-Yen Huang, and Chii-Jong Hwang. Power output analysis and optimization of two straight-bladed vertical-axis wind turbines. *Applied energy*, 185:223–232, 2017.

[45] CA Consul, RHJ Willden, E Ferrer, and MD McCulloch. Influence of solidity on the performance of a cross-flow turbine. In *8th European Wave and Tidal Energy Conference. Uppsala, Sweden*, 2009.

[46] Claudio A Consul. *Hydrodynamic analysis of a tidal cross-flow turbine.* PhD thesis, Oxford University, 2011.

[47] Thomas C Corke and Flint O Thomas. Dynamic stall in pitching airfoils: Aerodynamic damping and compressibility effects. *Annual Review of Fluid Mechanics*, 47:479–505, 2015.

[48] John O Dabiri. Potential order-of-magnitude enhancement of wind farm power density via counter-rotating vertical-axis wind turbine arrays. *Journal of Renewable and Sustainable Energy*, 3(4):043104, 2011.

[49] John O Dabiri. Emergent aerodynamics in wind farms. *Physics today*, 67(10):66–67, 2014.

[50] Louis Angelo Danao, Ning Qin, and Robert Howell. A numerical study of blade thickness and camber effects on vertical axis wind turbines. *Proceedings of the Institution of Mechanical Engineers, Part A: Journal of Power and Energy*, page 0957650912454403, 2012.

[51] László Daróczy, Gábor Janiga, and Dominique Thévenin. Computational fluid dynamics based shape optimization of airfoil geometry for an h-rotor using a genetic algorithm. *Engineering Optimization*, 50(9):1483–1499, 2018.

[52] Georges Jean Marie Darrieus. Turbine having its rotating shaft transverse to the flow of the current, December 8 1931. US Patent 1,835,018.

[53] Scott TM Dawson, Maziar S Hemati, Matthew O Williams, and Clarence W Rowley. Characterizing and correcting for the effect of sensor noise in the dynamic mode decomposition. *Experiments in Fluids*, 57(3):1–19, 2016.

[54] Michael H Dickinson, Fritz-Olaf Lehmann, and Sanjay P Sane. Wing rotation and the aerodynamic basis of insect flight. *Science*, 284(5422):1954–1960, 1999.

[55] Mark Drela. Xfoil: An analysis and design system for low reynolds number airfoils. In *Low Reynolds number aerodynamics*, pages 1–12. Springer, 1989.

[56] Karthikeyan Duraisamy and Vinod Lakshminarayan. Flow physics and performance of vertical axis wind turbine arrays. In *32nd AIAA Applied Aerodynamics Conference*, page 3139, 2014.

[57] Naveed Durrani, Ning Qin, Harris Hameed, and Shahab Khushnood. 2-d numerical analysis of a vawt wind farm for different configurations. In *49th AIAA Aerospace Sciences Meeting including the New Horizons Forum and Aerospace Exposition*, page 461, 2011.

[58] Okeoghene Eboibi, Louis Angelo M Danao, and Robert J Howell. Experimental investigation of the influence of solidity on the performance and flow field aerodynamics of vertical axis wind turbines at low reynolds numbers. *Renewable Energy*, 92:474–483, 2016.

[59] Daniel Edgington-Mitchell, Kilian Oberleithner, Damon R Honnery, and Julio Soria. Coherent structure and sound production in the helical mode of a screeching axisymmetric jet. *Journal of Fluid Mechanics*, 748:822–847, 2014.

[60] Jonathan M Edwards, Louis Angelo Danao, and Robert J Howell. Piv measurements and cfd simulation of the performance and flow physics and of a small-scale vertical axis wind turbine. *Wind Energy*, 18(2):201–217, 2015.

[61] Enerdata. Global energy statistical yearbook, 2018.

[62] Pål Egil Eriksen and Per-Åge Krogstad. Development of coherent motion in the wake of a model wind turbine. *Renewable Energy*, 108:449–460, 2017.

[63] Johannes Falnes et al. Optimum control of oscillation of wave-energy converters. *International Journal of Offshore and Polar Engineering*, 12(02), 2002.

[64] M. Farazmand and G. Haller. Computing Lagrangian coherent structures from their variational theory. *Chaos*, 22(013128):013128–1–013128–12, 2012.

[65] Carlos Simão Ferreira and Ben Geurts. Aerofoil optimization for vertical-axis wind turbines. *Wind Energy*, 18(8):1371–1385, 2015.

[66] Carlos Simão Ferreira, Gijs van Kuik, Gerard van Bussel, and Fulvio Scarano. Visualization by piv of dynamic stall on a vertical axis wind turbine. *Experiments in Fluids*, 46(1):97–108, 2009.

[67] CJ Simao Ferreira, H Bijl, G Van Bussel, and G Van Kuik. Simulating dynamic stall in a 2d vawt: modeling strategy, verification and validation with particle image velocimetry data. In *Journal of physics: conference series*, volume 75, page 012023. IOP Publishing, 2007.

[68] Andrzej J Fiedler and Stephen Tullis. Blade offset and pitch effects on a high solidity vertical axis wind turbine. *Wind engineering*, 33(3):237–246, 2009.

[69] Dominic Forbush, Robert J Cavagnaro, and Brian Polagye. Power-tracking control for cross-flow turbines. *Journal of Renewable and Sustainable Energy*, 11(1):014501, 2019.

[70] P Fraunie, C Beguier, I Paraschivoiu, and G Brochier. Water channel experiments of dynamic stall on Darrieus wind turbine blades. *Journal of Propulsion and Power*, 2(5):445–449, 1986.

[71] Nobuyuki Fujisawa and Satoshi Shibuya. Observations of dynamic stall on Darrieus wind turbine blades. *Journal of Wind Engineering and Industrial Aerodynamics*, 89(2):201–214, 2001.

[72] Ryan Gerakopulos, Michael Boutilier, and Serhiy Yarusevych. Aerodynamic characterization of a naca 0018 airfoil at low reynolds numbers. In *AIAA, 40th Fluid dynamics conference and Exhibit*, volume 4629, 2010.

[73] P Gipe. Wind energy for the rest of us: http://www.wind-works.org/cms/index.php?id=116.

[74] Harry J Goett and W Kenneth Bullivant. Tests of naca 0009, 0012, and 0018 airfoils in the full-scale tunnel, report no.647. Technical report, National Advisory Commitee for Aeronautics, 1939.

[75] Derek G Goring and Vladimir I Nikora. Despiking acoustic doppler velocimeter data. *Journal of Hydraulic Engineering*, 128(1):117–126, 2002.

[76] A Gorlov. Development of the helical reaction hydraulic turbine. final technical report, july 1, 1996–june 30, 1998. Technical report, Northeastern Univ., Boston, MA (United States), 1998.

[77] Rémi Gosselin, Guy Dumas, and Matthieu Boudreau. Parametric study of h-darrieus vertical-axis turbines using cfd simulations. *Journal of Renewable and Sustainable Energy*, 8(5):053301, 2016.

[78] Anders Goude, Staffan Lundin, and Mats Leijon. A parameter study of the influence of struts on the performance of a vertical-axis marine current turbine. In *Proceedings of the 8th European wave and tidal energy conference, EWTEC09, Uppsala, Sweden*, pages 477–483. Citeseer, 2009.

[79] Melissa A Green, Clarence W Rowley, and George Haller. Detection of lagrangian coherent structures in three-dimensional turbulence. *Journal of Fluid Mechanics*, 572:111–120, 2007.

[80] David Greenblatt, Amos Ben-Harav, and Hanns Mueller-Vahl. Dynamic stall control on a vertical-axis wind turbine using plasma actuators. *AIAA journal*, 52(2):456–462, 2014.

[81] Daniel Griffith, Matthew F Barone, Joshua Paquette, Brian Christopher Owens, Diana L Bull, Carlos Simao-Ferriera, Andrew Goupee, and Matt Fowler. Design studies for deep-water floating offshore vertical axis wind turbines. Technical report, Sandia National Lab.(SNL-NM), Albuquerque, NM (United States), 2018.

[82] G. Haller. Lagrangian coherent structures from approximate velocity data. *Physics of Fluids*, 14(6):1851–1861, June 2002.

[83] George Haller and Francisco J Beron-Vera. Coherent lagrangian vortices: The black holes of turbulence. *Journal of Fluid Mechanics*, 731, 2013.

[84] Maziar S Hemati, Clarence W Rowley, Eric A. Deem, and Louis N. Cattafesta. Debiasing the dynamic mode decomposition for applied Koopman spectral analysis. *Theoretical and Computational Fluid Dynamics*, 31(4):349–368, 2017.

[85] Craig Hill, Vincent S Neary, Budi Gunawan, Michele Guala, and Fotis Sotiropoulos. Us department of energy reference model program rm2: Experimental results. *Sandia National Laboratories, Albuquerque, NM*, 2014.

[86] TC Hohman, L Martinelli, and AJ Smits. The effects of inflow conditions on vertical axis wind turbine wake structure and performance. *Journal of Wind Engineering and Industrial Aerodynamics*, 183:1–18, 2018.

[87] JG Holierhoek, JB De Vaal, AH Van Zuijlen, and H Bijl. Comparing different dynamic stall models. *Wind Energy*, 16(1):139–158, 2013.

[88] Philip Holmes, John L Lumley, Gahl Berkooz, and Clarence W Rowley. *Turbulence, coherent structures, dynamical systems and symmetry.* Cambridge university press, 2012.

[89] FS Hover, Ø Haugsdal, and MS Triantafyllou. Effect of angle of attack profiles in flapping foil propulsion. *Journal of Fluids and Structures*, 19(1):37–47, 2004.

[90] Robert Howell, Ning Qin, Jonathan Edwards, and Naveed Durrani. Wind tunnel and numerical study of a small vertical axis wind turbine. *Renewable Energy*, 35(2):412–422, 2010.

[91] Julian CR Hunt, Alan A Wray, and Parviz Moin. Eddies, streams, and convergence zones in turbulent flows. In *Studying Turbulence Using Numerical Simulation Databases, 2. Proceedings of the 1988 Summer Program*, number 19890015184. NASA, 1988.

[92] Abul Khair Muhammad Fazle Hussain and William C Reynolds. The mechanics of an organized wave in turbulent shear flow. *Journal of Fluid Mechanics*, 41(2):241–258, 1970.

[93] Eastman N Jacobs and Albert Sherman. Airfoil section characteristics as affected by variations of the reynolds number, report no. 586. Technical report, National Advisory Commitee for Aeronautics, 1937.

[94] Mark Z Jacobson and Cristina L Archer. Saturation wind power potential and its implications for wind energy. *Proceedings of the National Academy of Sciences*, 2012.

[95] M Jafaryar, R Kamrani, M Gorji-Bandpy, M Hatami, and DD Ganji. Numerical optimization of the asymmetric blades mounted on a vertical axis cross-flow wind turbine. *International Communications in Heat and Mass Transfer*, 70:93–104, 2016.

[96] Kathryn E Johnson, Lucy Y Pao, Mark J Balas, and Lee J Fingersh. Control of variable-speed wind turbines: standard and adaptive techniques for maximizing energy capture. *Control Systems, IEEE*, 26(3):70–81, 2006.

[97] Robert T Jones. Correction of the lifting line theory for the effect of the chord. Technical report, NATIONAL ADVISORY COMMITTEE FOR AERONAUTICS LANGLEY FIELD VA LANGLEY â, 1941.

[98] Th. V. Kármán. Über laminare und turbulente reibung. *ZAMM - Journal of Applied Mathematics and Mechanics / Zeitschrift für Angewandte Mathematik und Mechanik*, 1(4):233–252, 1921.

[99] MJ Khan, G Bhuyan, MT Iqbal, and JE Quaicoe. Hydrokinetic energy conversion systems and assessment of horizontal and vertical axis turbines for river and tidal applications: A technology status review. *Applied Energy*, 86(10):1823–1835, 2009.

[100] Thomas Kinsey and Guy Dumas. Parametric study of an oscillating airfoil in a power-extraction regime. *AIAA journal*, 46(6):1318–1330, 2008.

[101] M. Kinzel, Q. Mulligan, and J. O. Dabiri. Energy exchange in an array of vertical-axis wind turbines. *Journal of Turbulence*, 13(38):1–13, 2012.

[102] Matthias Kinzel, Daniel B Araya, and John O Dabiri. Turbulence in vertical axis wind turbine canopies. *Physics of Fluids*, 27(11):115102, 2015.

[103] BK Kirke. Tests on ducted and bare helical and straight blade darrieus hydrokinetic turbines. *Renewable Energy*, 36(11):3013–3022, 2011.

[104] Paul C Klimas and Mark H Worstell. *Effects of blade preset pitch/offset on curved-blade Darrieus vertical axis wind turbine performance*. Sandia National Laboratories, 1981.

[105] Ilan Kroo. Drag due to lift: concepts for prediction and reduction. *Annual Review of Fluid Mechanics*, 33(1):587–617, 2001.

[106] J Nathan Kutz, Steven L Brunton, Bingni W Brunton, and Joshua L Proctor. *Dynamic mode decomposition: data-driven modeling of complex systems*, volume 149. SIAM, 2016.

[107] Charles L Ladson. Effects of independent variation of mach and reynolds numbers on the low-speed aerodynamic characteristics of the naca 0012 airfoil section, nasa technical memorandum 4074. Technical report, NAtional Aeronautics and Space Administration, 1988.

[108] EV Laitone. Wind tunnel tests of wings at reynolds numbers below 70 000. *Experiments in Fluids*, 23(5):405–409, 1997.

[109] Young-Tae Lee and Hee-Chang Lim. Numerical study of the aerodynamic performance of a 500 w darrieus-type vertical-axis wind turbine. *Renewable Energy*, 83:407–415, 2015.

[110] J Gordon Leishman. *Principles of Helicopter Aerodynamics with CD Extra*. Cambridge university press, 2006.

[111] David Lentink, William B Dickson, Johan L Van Leeuwen, and Michael H Dickinson. Leading-edge vortices elevate lift of autorotating plant seeds. *Science*, 324(5933):1438–1440, 2009.

[112] Ye Li and Sander M Calisal. Three-dimensional effects and arm effects on modeling a vertical axis tidal current turbine. *Renewable energy*, 35(10):2325–2334, 2010.

[113] LEM Lignarolo, D Ragni, F Scarano, CJ Simão Ferreira, and GJW van Bussel. Tip-vortex instability and turbulent mixing in wind-turbine wakes. *Journal of Fluid Mechanics*, 781:467–493, 2015.

[114] PBS Lissaman. Low-reynolds-number airfoils. *Annual Review of Fluid Mechanics*, 15(1):223–239, 1983.

[115] Laurence K Loftin Jr and Hamilton A Smith. Aerodynamic characteristics of 15 naca airfoil sections at seven reynolds numbers from 0.7×10^6 to 9.0×10^6, technidal note no. 1945. Technical report, National Advisory Commitee for Aeronautic, 1949.

[116] D. M. Luchtenburg, S. L. Brunton, and C. W. Rowley. Long-time uncertainty propagation using generalized polynomial chaos and flow map composition. *Journal of Computational Physics*, 274:783–802, 2014.

[117] John Leask Lumley. The structure of inhomogeneous turbulent flows. *Atmospheric turbulence and radio wave propagation*, 1967.

[118] Audrey P Maertens, Amy Gao, and Michael S Triantafyllou. Optimal undulatory swimming for a single fish-like body and for a pair of interacting swimmers. *Journal of Fluid Mechanics*, 813:301–345, 2017.

[119] Ion Mălăel, Valeriu Drăgan, and Georgel Vizitiu. The vertical axis wind turbine efficiency evaluation by using the cfd methods. In *Applied Mechanics and Materials*, volume 772, pages 90–95. Trans Tech Publ, 2015.

[120] Martino Marini, Aristide Massardo, and Antonio Satta. Performance of vertical axis wind turbines with different shapes. *Journal of wind engineering and industrial aerodynamics*, 39(1):83–93, 1992.

[121] Ivo Marinić-Kragić, Damir Vučina, and Zoran Milas. Numerical workflow for 3d shape optimization and synthesis of vertical-axis wind turbines for specified operating regimes. *Renewable Energy*, 115:113–127, 2018.

[122] RA McAdam, GT Houlsby, and MLG Oldfield. Experimental measurements of the hydrodynamic performance and structural loading of the transverse horizontal axis water turbine: Part 1. *Renewable Energy*, 59:105–114, 2013.

[123] WJ McCroskey. The phenomenon of dynamic stall. Technical report, National Aeronautics and Space Administration Moffett Field CA, AMES Research Center, 1981.

[124] K McLaren, S Tullis, and S Ziada. Computational fluid dynamics simulation of the aerodynamics of a high solidity, small-scale vertical axis wind turbine. *Wind Energy*, 15(3):349–361, 2012.

[125] S McTavish, Daniel Feszty, and Fred Nitzsche. An experimental and computational assessment of blockage effects on wind turbine wake development. *Wind Energy*, 17(10):1515–1529, 2014.

[126] Igor Mezić. Analysis of fluid flows via spectral properties of the koopman operator. *Annual Review of Fluid Mechanics*, 45:357–378, 2013.

[127] PG Migliore, WP Wolfe, and JB Fanucci. Flow curvature effects on darrieus turbine blade aerodynamics. *Journal of Energy*, 4(2):49–55, 1980.

[128] Michele Milano and Morteza Gharib. Uncovering the physics of flapping flat plates with artificial evolution. *Journal of Fluid Mechanics*, 534:403–409, 2005.

[129] Mark A Miller, Subrahmanyam Duvvuri, Ian Brownstein, Marcus Lee, John O Dabiri, and Marcus Hultmark. Vertical-axis wind turbine experiments at full dynamic similarity. *Journal of Fluid Mechanics*, 844:707–720, 2018.

[130] Michael Miller, Ben Strom, Kenneth Breuer, and Shreyas Mandre. Optimization of energy harvesting efficiency of an oscillating hydrofoil: Sinusoidal and non-sinusoidal trajectories. *Bulletin of the American Physical Society*, 59, 2014.

[131] MH Mohamed, AM Ali, and AA Hafiz. Cfd analysis for h-rotor darrieus turbine as a low speed wind energy converter. *Engineering Science and Technology, an International Journal*, 18(1):1–13, 2015.

[132] Erik Möllerström, Paul Gipe, Jos Beurskens, and Fredric Ottermo. A historical review of vertical axis wind turbines rated 100 kw and above. *Renewable and Sustainable Energy Reviews*, 105:1–13, 2019.

[133] C Moné, M Hand, J. R. Bolinger, , and D Heimiller. 2015 cost of wind energy review. Technical report, Energy Analysis and Environmental Impacts Division, Lawrence Berkeley National Laboratory, 2017.

[134] Nobuhito Mori, Takuma Suzuki, and Shohachi Kakuno. Noise of acoustic doppler velocimeter data in bubbly flows. *Journal of engineering mechanics*, 133(1):122–125, 2007.

[135] FT Muijres, LC Johansson, Ryan Barfield, Marta Wolf, GR Spedding, and Anders Hedenström. Leading-edge vortex improves lift in slow-flying bats. *Science*, 319(5867):1250–1253, 2008.

[136] Iulian Munteanu, Antoneta Iuliana Bratcu, and Emil Ceanga. Wind turbulence used as searching signal for mppt in variable-speed wind energy conversion systems. *Renewable Energy*, 34(1):322–327, January 2009.

[137] Ralph J Muraca and Robert J Guillotte. Wind tunnel investigation of a 14 foot vertical axis windmill. NASA Technical Memorandum NASA TM X-72663, NAtional Aeronautics and Space Administration, Langley Research Center, Hampton, Virginia, 1976.

[138] Jonathan Murray and Matthew Barone. The development of cactus, a wind and marine turbine performance simulation code. In *49th AIAA Aerospace Sciences Meeting including the New Horizons Forum and Aerospace Exposition*, page 147, 2011.

[139] John A Nelder and Roger Mead. A simplex method for function minimization. *The computer journal*, 7(4):308–313, 1965.

[140] Adam L Niblick. Experimental and analytical study of helical cross-flow turbines for a tidal micropower generation system. Master's thesis, University of Washington, 2012.

[141] Michele Nini, Valentina Motta, Giampiero Bindolino, and Alberto Guardone. Three-dimensional simulation of a complete vertical axis wind turbine using overlapping grids. *Journal of Computational and Applied Mathematics*, 270:78–87, 2014.

[142] Kilian Oberleithner, Moritz Sieber, CN Nayeri, CO Paschereit, Christoph Petz, H-C Hege, BR Noack, and I Wygnanski. Three-dimensional coherent structures in a swirling jet undergoing vortex breakdown: stability analysis and empirical mode construction. *Journal of Fluid Mechanics*, 679:383–414, 2011.

[143] Tomohisa Ohtake, Yusuke Nakae, and Tatsuo Motohashi. Nonlinearity of the aerodynamic characteristics of naca0012 aerofoil at low reynolds numbers. *Japan Society of Aeronautical Space Sciences*, 55:439–445, 2007.

[144] I Paraschivoiu, O Trifu, and F Saeed. H-darrieus wind turbine with blade pitch control. *International Journal of Rotating Machinery*, 2009, 2009.

[145] Ion Paraschivoiu. Double-multiple streamtube model for studying vertical-axis wind turbines. *Journal of propulsion and power*, 4(4):370–377, 1988.

[146] HY Peng, HF Lam, and CF Lee. Investigation into the wake aerodynamics of a five-straight-bladed vertical axis wind turbine by wind tunnel tests. *Journal of Wind Engineering and Industrial Aerodynamics*, 155:23–35, 2016.

[147] G Persico, Vincenzo Dossena, Berardo Paradiso, L Battisti, A Brighenti, and E Benini. Three-dimensional character of vawt wakes: an experimental investigation for h-shaped and troposkien architectures. In *ASME Turbo Expo 2016: Turbomachinery Technical Conference and Exposition*, pages V009T46A015–V009T46A015. American Society of Mechanical Engineers, 2016.

[148] C Picard and J Delville. Pressure velocity coupling in a subsonic round jet. *International Journal of Heat and Fluid Flow*, 21(3):359–364, 2000.

[149] Antonio Posa, Colin M Parker, Megan C Leftwich, and Elias Balaras. Wake structure of a single vertical axis wind turbine. *International Journal of Heat and Fluid Flow*, 61:75–84, 2016.

[150] Pavithra Premaratne, Tian Wei, and Hui Hu. Analysis of turbine wake characteristics using proper orthogonal decomposition (pod) and triple decomposition methods. In *46th AIAA Fluid Dynamics Conference*, page 3780, 2016.

[151] George William Rawlings. Parametric characterization of an experimental vertical axis hydro turbine. 2008.

[152] George William Rawlings. Parametric characterization of an experimental vertical axis hydro turbine. 2008.

[153] EG Reid. The effects of shielding the tips of airfoils", naca rep. 201. *Natl. Advis. Comm. Aeronaut., Hampton, VA*, 1924.

[154] Bernardo Luiz Rocha Ribeiro and Jennifer Franck. Energy harvesting and vortex wake structure of an oscillating hydrofoil at high reynolds number. *Bulletin of the American Physical Society*, 2018.

[155] Sung-Cheoul Roh and Seung-Hee Kang. Effects of a blade profile, the reynolds number, and the solidity on the performance of a straight bladed vertical axis wind turbine. *Journal of Mechanical Science and Technology*, 27(11):3299–3307, 2013.

[156] V Rolin and Fernando Porté-Agel. Wind-tunnel study of the wake behind a vertical axis wind turbine in a boundary layer flow using stereoscopic particle image velocimetry. In *Journal of physics: conference series*, volume 625, page 012012. IOP Publishing, 2015.

[157] Nicholas Rott and William S Lewellen. Boundary layers due to the combined effects of rotation and translation. *The Physics of Fluids*, 10(9):1867–1873, 1967.

[158] Clarence W Rowley, Igor Mezić, Shervin Bagheri, Philipp Schlatter, and Dan S Henningson. Spectral analysis of nonlinear flows. *Journal of fluid mechanics*, 641:115–127, 2009.

[159] Kevin J Ryan, Filippo Coletti, Christopher J Elkins, John O Dabiri, and John K Eaton. Three-dimensional flow field around and downstream of a subscale model rotating vertical axis wind turbine. *Experiments in Fluids*, 57(3):38, 2016.

[160] SH Salter. Are nearly all tidal stream turbine designs wrong? In *4th International Conference on Ocean Energy*, 2012.

[161] H Sarlak, T Nishino, LA Martínez-Tossas, C Meneveau, and Jens Nørkær Sørensen. Assessment of blockage effects on the wake characteristics and power of wind turbines. *Renewable Energy*, 93:340–352, 2016.

[162] T Sayadi, JW Nichols, PJ Schmid, and MR Jovanovic. Dynamic mode decomposition of h-type transition to turbulence. In *Proceedings of the Summer Program*, page 5. Citeseer, 2012.

[163] Frank Scheurich and Richard E Brown. Modelling the aerodynamics of vertical-axis wind turbines in unsteady wind conditions. *Wind Energy*, 16(1):91–107, 2013.

[164] Frank Scheurich, Timothy M Fletcher, and Richard E Brown. Effect of blade geometry on the aerodynamic loads produced by vertical-axis wind turbines. *Proceedings of the Institution of Mechanical Engineers, Part A: Journal of Power and Energy*, 225(3):327–341, 2011.

[165] Günter Schewe. Reynolds-number-effects in flow around a rectangular cylinder with aspect ratio 1: 5. *Journal of Fluids and Structures*, 39:15–26, 2013.

[166] H. W. Schiffer. World energy resources. Technical report, World Energy Council, 2016.

[167] Hermann Schlichting. *Boundary-layer theory*. McGraw-Hill, 7 edition, 1979.

[168] P. J. Schmid. Dynamic mode decomposition of numerical and experimental data. *Journal of Fluid Mechanics*, 656:5–28, August 2010.

[169] Alessandro Schönborn and Matthew Chantzidakis. Development of a hydraulic control mechanism for cyclic pitch marine current turbines. *Renewable Energy*, 32(4):662–679, 2007.

[170] S. C. Shadden, F. Lekien, and J. E. Marsden. Definition and properties of Lagrangian coherent structures from finite-time Lyapunov exponents in two-dimensional aperiodic flows. *Physica D*, 212:271–304, 2005.

[171] Sina Shamsoddin and Fernando Porté-Agel. Large eddy simulation of vertical axis wind turbine wakes. *Energies*, 7(2):890–912, 2014.

[172] Ati S Sharma, Igor Mezić, and Beverley J McKeon. Correspondence between koopman mode decomposition, resolvent mode decomposition, and invariant solutions of the navier-stokes equations. *Physical Review Fluids*, 1(3):032402, 2016.

[173] Robert E Sheldahl and Paul C Klimas. Aerodynamic characteristics of seven symmetrical airfoil sections through 180-degree angle of attack for use in aerodynamic analysis of vertical axis wind turbines. Technical report, Sandia National Labs., Albuquerque, NM (USA), 1981.

[174] Mitsuhiro Shiono, Katsuyuki Suzuki, and Seiji Kiho. An experimental study of the characteristics of a darrieus turbine for tidal power generation. *Electrical Engineering in Japan*, 132(3):38–47, 2000.

[175] Mitsuhiro Shiono, Katsuyuki Suzuki, Seiji Kiho, et al. Output characteristics of darrieus water turbine with helical blades for tidal current generations. In *Proceedings of the Twelfth International Offshore and Polar Engineering Conference, Kitakyushu, Japan*, pages 859–864, 2002.

[176] L. Sirovich. Turbulence and the dynamics of coherent structures, parts I-III. *Q. Appl. Math.*, XLV(3):561–590, 1987.

[177] Ante Šoda, Claudio Mannini, and Momir Sjerić. Investigation of unsteady air flow around two-dimensional rectangular cylinders. *Transactions of FAMENA*, 35(2), 2011.

[178] R Sonnenberger, K Graichen, and Pl Erk. Fourier averaging: a phase-averaging method for periodic flow. *Experiments in fluids*, 28(3):217–224, 2000.

[179] Peter South and Raj Rangi. *A wind tunnel investigation of a 14 ft. diameter vertical axis windmill.* National Aeronautical Establishment, Low Speed Aerodynamics Section, 1972.

[180] Peter South and Raj S Rangi. *Preliminary tests of a high speed vertical axis windmill model.* National Research Council of Canada, 1971.

[181] EM Sparrow and JL Gregg. Mass transfer, flow, and heat transfer about a rotating disk. *Journal of Heat Transfer*, 82(4):294–302, 1960.

[182] B. Strom, S. Brunton, and B. Polagye. Consequences of preset pitch angle on cross-flow turbine hydrodynamics. *Proceeding of the European Wave and Tidal Energy Conference*, 2015.

[183] B. Strom, S. Brunton, and B. Polagye. Advanced control methods for cross-flow turbines. *International Marine Renewable Energy Journal*, 1(2):129–138, Nov. 2018.

[184] Benjamin Strom, Steven L Brunton, and Brian Polagye. Intracycle angular velocity control of cross-flow turbines. *Nature Energy*, 2(8):17103, 2017.

[185] Benjamin Strom, Noah Johnson, and Brian Polagye. Impact of blade mounting structures on cross-flow turbine performance. *Journal of Renewable and Sustainable Energy*, 10(3):034504, 2018.

[186] Benjamin Strom, Daegyoum Kim, Shreyas Mandre, and Kenneth Breuer. Parametric dependence of energy harvesting performance with an oscillating hydrofoil. *Bulletin of the American Physical Society*, 59, 2014.

[187] Benjamin Strom, Isabel Scherl, Steven Brunton, and Brian Polagye. Geometric and control optimization of an array of two cross-flow turbines. *Bulletin of the American Physical Society*, 2018.

[188] Herbert J Sutherland, Dale E Berg, and Thomas D Ashwill. A retrospective of VAWT technology. *Sandia Report No. SAND2012-0304*, 2012.

[189] Kunihiko Taira, Steven L Brunton, Scott Dawson, Clarence W Rowley, Tim Colonius, Beverley J McKeon, Oliver T Schmidt, Stanislav Gordeyev, Vassilios Theofilis, and Lawrence S Ukeiley. Modal analysis of fluid flows: An overview. *AIAA Journal*, 55(12):4013–4041, 2017.

[190] Tadakazu Tanino, Shinichiro Nakao, Takeshi Miyaguni, and Kazunobu Takahashi. Influence of reynolds number and scale on performance evaluation of lift-type vertical axis wind turbine by scale-model wind tunnel tests. *International Journal of Fluid Machinery and Systems*, 4(2):229–234, 2011.

[191] Suzanne Tegen, M Hand, B Maples, E Lantz, P Schwabe, and A Smith. 2010 cost of wind energy review. Technical report, National Renewable Energy Lab.(NREL), Golden, CO (United States), 2012.

[192] G Tescione, D Ragni, C He, CJ Simão Ferreira, and GJW Van Bussel. Near wake flow analysis of a vertical axis wind turbine by stereoscopic particle image velocimetry. *Renewable Energy*, 70:47–61, 2014.

[193] Arti Tirkey, Yamini Sarthi, Khemraj Patel, Ritesh Sharma, and Prakash Kumar Sen. Study on the effect of blade profile, number of blade, reynolds number, aspect ratio on the performance of vertical axis wind turbine. *International Journal of Science, Engineering and Technology Research*, 2014.

[194] Aaron Towne, Oliver T Schmidt, and Tim Colonius. Spectral proper orthogonal decomposition and its relationship to dynamic mode decomposition and resolvent analysis. *Journal of Fluid Mechanics*, 847:821–867, 2018.

[195] J. H. Tu, C. W. Rowley, D. M. Luchtenburg, S. L. Brunton, and J. N. Kutz. On dynamic mode decomposition: theory and applications. *Journal of Computational Dynamics*, 1(2):391–421, 2014.

[196] GJW Van Bussel, H Polinder, and HFA Sidler. The development of turby, a small vawt for the built environment. In *Global Windpower 2004 Conference and Exhibition, Chicago, IL*, page 10, 2004.

[197] J. J. Videler, E. J. Samhuis, and G. D. E. Povel. Leading-edge vortex lifts swifts. *Science*, 306:1960–1962, 2004.

[198] Albert E Von Doenhoff and Frank T Abbott. The langley two-dimensional low-turbulence pressure tunnel, technical note no. 1283. Technical report, National Advisory Commitee for Aeronautics, 1947.

[199] TL Wahl. Despiking acoustic doppler velocimeter data. discussion. *Jl of Hyd. Engrg*, pages 484–487, 2003.

[200] Douglas R Warrick, Bret W Tobalske, and Donald R Powers. Aerodynamics of the hovering hummingbird. *Nature*, 435(7045):1094–1097, 2005.

[201] Lawrence I Weingarten and BF Blackwell. Sandia vertical-axis wind turbine program. technical quarterly report, january–march 1976. Technical report, Sandia Labs., Albuquerque, N. Mex.(USA), 1976.

[202] R. W. Whittlesey, S. C. Liska, and J. O. Dabiri. Fish schooling as a basis for vertical-axis wind turbine farm design. *Bioinspiration and Biomimetics*, 5:035005, 2010.

[203] Ryan Wiser and Mark Bolinger. 2010 wind technologies market report. Technical report, National Renewable Energy Lab.(NREL), Golden, CO (United States), 2011.

[204] JZ Wu, AD Vakili, and JM Wu. Review of the physics of enhancing vortex lift by unsteady excitation. *Progress in Aerospace Sciences*, 28(2):73–131, 1991.

[205] Qing Xiao, Wei Liao, Shuchi Yang, and Yan Peng. How motion trajectory affects energy extraction performance of a biomimic energy generator with an oscillating foil? *Renewable Energy*, 37(1):61–75, 2012.

[206] Joshua Yen and Noor A Ahmed. Enhancing vertical axis wind turbine by dynamic stall control using synthetic jets. *Journal of Wind Engineering and Industrial Aerodynamics*, 114:12–17, 2013.

A.1 Encoder Data Differentiation MATLAB Code

```matlab
function [dy,ddy]=multi_poly_diff(y,win,n)
% Moving window differentiator for real data
% Performs least squared fit of polynomial of degree n over windows of
% length win, finds analytical derivatives, evaluates at midpoint of window
% (except win/2 endpoints)

% INPUTS:
% y: data to differentiate
% win: window size (default is 11)
% n: degree of polynomial (default is 2)
% OUTPUTS
% dy: first derivative of y
% ddy: second derivative of y

% Benjamin Strom, 2015

% check inputs
if nargin<3
    n=2;
end
if nargin<2
    win=11;
end
if length(y)<win
    error('Input y must be at least as long window')
end

% make window odd so point of interest is at center
if mod(win,2)~=1
    win=win+1;
end

wr=floor(win/2);
dn=length(y);
rsy=size(y);
y=reshape(y,[1,dn]);
dy=zeros(1,length(y));
ddy=zeros(1,length(y));

M = bsxfun(@power,(1:win)',0:n);
for i=1:dn-2*wr
    c= M\y(i:win+i-1)';
    for j=1:n
        dc(n-j+1)=c(j+1)*j;
        dy(i+wr)=dy(i+wr)+dc(n-j+1)*(wr+1)^(j-1);
    end
    for j=1:n-1
        ddc(n-j+1)=c(j+2)*j*(j+1);
        ddy(i+wr)=ddy(i+wr)+ddc(n-j+1)*(wr+1)^(j-1);
    end
    if i==1
        dc1=dc;
        ddc1=ddc;
    end
    if i==dn-2*wr
        dc2=dc;
        ddc2=ddc;
    end
end

% take care of first end last window/2 points
for i = 1:wr
    if i == 1
        dy(1) = y(2) - y(1);
        dy(end) = y(end) - y(end-1);
    elseif i == 2
        p = polyfit([1 2 3],y(1:3),2);
        dy(2) = 2*p(1)*2+p(2);
        ddy(1:2) = 2*p(1);
        p = polyfit([1 2 3],y(end-2:end),2);
        dy(end-1) = 2*p(1)*2+p(2);
        ddy(end-1:end) = 2*p(1);
    else
        dy(i) = 0;
        dy(end-i+1) = 0;
        ddy(i) = 0;
        ddy(end-i+1) = 0;
        p1 = polyfit(1:i*2-1,y(1:i*2-1),n);
```

```
        p2 = polyfit(1:i*2-1,y(end-(2*i-2):end),n);
        for j = 1:length(p1)-1
           dy(i) = dy(i) + (n-j+1)*p1(j)*i^(n-j);
           dy(end-i+1) = dy(end-i+1) + (n-j+1)*p2(j)*i^(n-j);
        end
        for j = 1:length(p1)-2
            ddy(i) = ddy(i) + (n-j+1)*(n-j)*p1(j)*i^(n-j-1);
            ddy(end-i+1) = ddy(end-i+1) + (n-j+1)*(n-j)*p2(j)*i^(n-j-1);
        end
    end
end

dy=reshape(dy,rsy);
ddy=reshape(ddy,rsy);
end
```

A.2 DMD Triple Decomposition Phase Correction

The DMD solution can be written as

$$\boldsymbol{X}(t) = \boldsymbol{\Phi} e^{\boldsymbol{\Omega} t} \boldsymbol{b}. \tag{1}$$

For the proceeding analysis, this will be written in indicial notation with index k corresponding to the kth DMD mode, and index j corresponding to the jth measurement or sensor (row of $\boldsymbol{X}$). The DMD solution is then

$$x_j(t) = \sum_{k=1}^{r} \phi_{j,k} e^{\omega_k t} b_k \tag{2}$$

where $\phi_{j,k}$ and ω_k are complex scalars and b_k is a real valued scalar. For the purposes of expansion, let

$$\phi_{j,k} = \alpha_{j,k} + i\beta_{j,k} \tag{3}$$

and

$$\omega_k = \gamma_k + i\delta_k \tag{4}$$

where $\alpha_{j,k}$, $\beta_{j,k}$, γ_k, and δ_k are real valued scalars. The DMD solution can then be written as

$$x_j(t) = \sum_{k=1}^{r} b_k e^{\gamma_k t} \sqrt{\alpha_{j,k}^2 + \beta_{j,k}^2} \left[\alpha_{j,k} \cos(\delta_k t) - \beta_{j,k} \sin(\delta_k t) + i \left\{\beta_{j,k} \cos(\delta_k t) + \alpha_{j,k} \sin(\delta_k t)\right\}\right] \tag{5}$$

or

$$x_j(t) = \sum_{k=1}^{r} b_k e^{\gamma_k t} \sqrt{\alpha_{j,k}^2 + \beta_{j,k}^2} \left[\cos\left(\delta_k t + \tan^{-1} \frac{\alpha_{j,k}}{\beta_{j,k}}\right) + i \cos\left(\delta_k t - \tan^{-1} \frac{\beta_{j,k}}{\alpha_{j,k}}\right)\right] \tag{6}$$

where $\tan^{-1}$ indicates the 4-quadrant arctangent. Real-valued solutions, such as in fluid flows, will simplify to

$$x_j(t) = \sum_{k=1}^{r} b_k e^{\gamma_k t} \sqrt{\alpha_{j,k}^2 + \beta_{j,k}^2} \cos\left(\delta_k t + \tan^{-1}\frac{\alpha_{j,k}}{\beta_{j,k}}\right). \tag{7}$$

The objective of the DMD solution is clear in this form: To express the data in terms of a series of modes, where each modes has a consistent growth or decay rate γ_k, oscillation rate δ_k, and overall amplitude b_k across all measurements. Within each mode, each sensor in X has an individual phase-shift and amplitude, given by the components of $\phi_{j,k}$, $\alpha_{j,k}$ and $\beta_{j,k}$. In vector form this can be written as

$$\boldsymbol{X}(t) = \sum_{k=1}^{r} b_k e^{\mathrm{Re}(\omega_k)t} \left|\boldsymbol{\phi}_k\right| \cos\left\{\mathrm{Im}(\omega_k)t + \angle\boldsymbol{\phi}_k\right\} \tag{8}$$

Now suppose we are interested in mainly oscillatory modes, or that we have restricted the DMD algorithm to return only modes no growth or decay, such that

$$\gamma_k = \mathrm{Re}(\omega_k) \approx 0, \tag{9}$$

giving

$$\boldsymbol{X}(t) = \sum_{k=1}^{r} b_k \left|\boldsymbol{\phi}_k\right| \cos\left\{\mathrm{Im}(\omega_k)t + \angle\boldsymbol{\phi}_k\right\}. \tag{10}$$

For comparison, consider two data matrices derived from an oscillatory system, $\boldsymbol{X}_a$ and $\boldsymbol{X}_b$. $\boldsymbol{X}_a$ is a traditional DMD data matrix, where a number of sensor locations, spanning the rows of $\boldsymbol{X}_a$ are recorded for a sequence of time snapshots, spanning the columns of $\boldsymbol{X}_a$. $\boldsymbol{X}_b$ consist of two measurement time-series, taken at non-overlapping times. The two time-series contain a subset of overlapping sensors, but the majority of sensors differ between subsets. However, in total the measurement locations are the same as in $\boldsymbol{X}_a$. This is a typical measurement scheme for particle-image velocimetry, where a large, high-resolution field-of-view is obtained by collecting overlapping spatial windows at differing times. Despite the differing measurement times, the two datasets are concatenated vertically to form $\boldsymbol{X}_b$, repeating sensor locations where overlap occurs, such that

$$\boldsymbol{X}_b = \begin{bmatrix} \boldsymbol{X}_{b,1} \\ \boldsymbol{X}_{b,2} \end{bmatrix}. \tag{11}$$

Because X_a and X_b contain the same sensor locations, and the oscillatory nature of our system is statistically stationary, DMD will return the same set of $\mathrm{Im}(\omega_k)$ for both matrices[1]. In the overlap regions of $\boldsymbol{X}_b$, the modal measurement amplitudes $b_k\,|\boldsymbol{\phi}_k|$ are also the same. This leaves only the phase of oscillation, $\angle\phi_{j,k}$, that differs between repeated sensor locations in $\boldsymbol{X}_b$. Since the phase values in each sensor subset are self consistent, a single phase correction can be applied to one of the subsets to bring it into alignment with the other, or

$$\boldsymbol{X}(t) = \begin{bmatrix} \sum_{k=1}^{r} b_k\,|\boldsymbol{\phi}_{k,1}| \cos\left\{\mathrm{Im}(\omega_k)t + \angle\boldsymbol{\phi}_{k,1}\right\} \\ \sum_{k=1}^{r} b_k\,|\boldsymbol{\phi}_{k,2}| \cos\left\{\mathrm{Im}(\omega_k)t + \angle\boldsymbol{\phi}_{k,2} + \psi_k\right\} \end{bmatrix} \tag{12}$$

where the subscripts 1 and 2 denote the sensor subsets, and ψ_k is the mode-specific phase correction term, which can be solved for by minimizing the mode reconstruction error in the sensor overlap region.

A.3 Prototype: Rotors coupled via non-circular gears

One possible method of producing sinusoidal angular velocity motion without the penalty of large electrical energy fluxes is to mechanically couple two rotors that oscillate out-of-phase, swapping kinetic energy between the rotors. One implementation is to use non-circular gears connecting the two rotors to the generator shaft, such that when the generator spins at a constant rate, the rotor oscillates. Such gears are demonstrated in Fig. **??**. In Fig. **??**, two sets of the gears connect two rotors with concentric driveshafts to implement the out-of-phase velocity oscillation.

---

[1] In X_b, a slight preference may be given to frequencies that dominate in the sensor overlap regions, since these are expressed twice. In a future implementation, these could be weighted to avoid this.

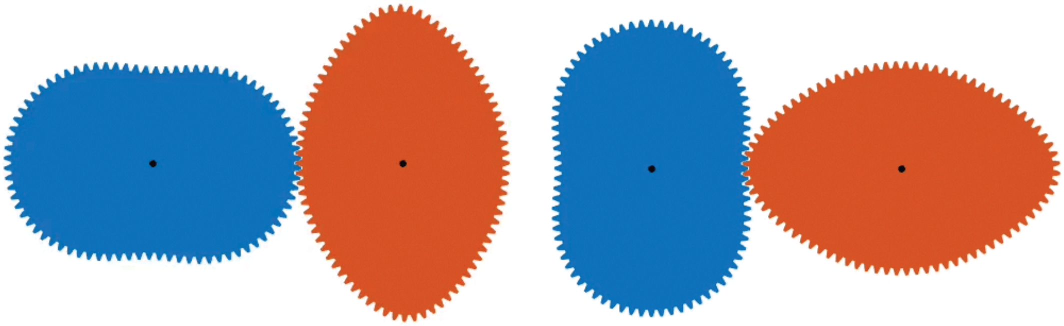

Figure 1: Non-circular gears for sinusoidal angular velocity.

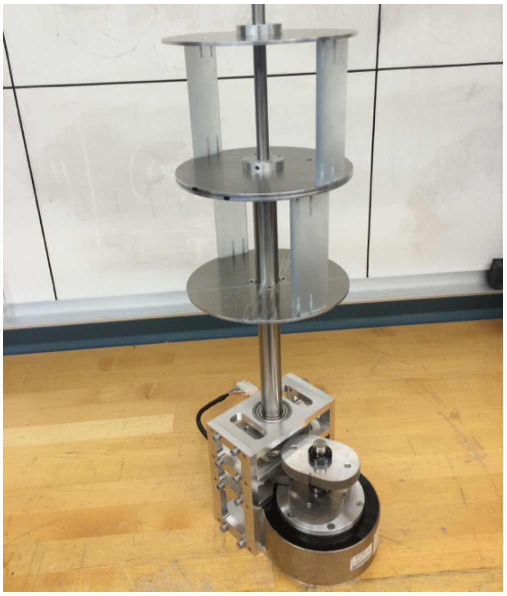

Figure 2: A prototype assembly of two concentric rotors driven by 90° out-of-phase non-circular gears connecting to a single generator.